Nanophotonics circuits formed by DNA self-assembly

Master thesis in Nanobiotechnology

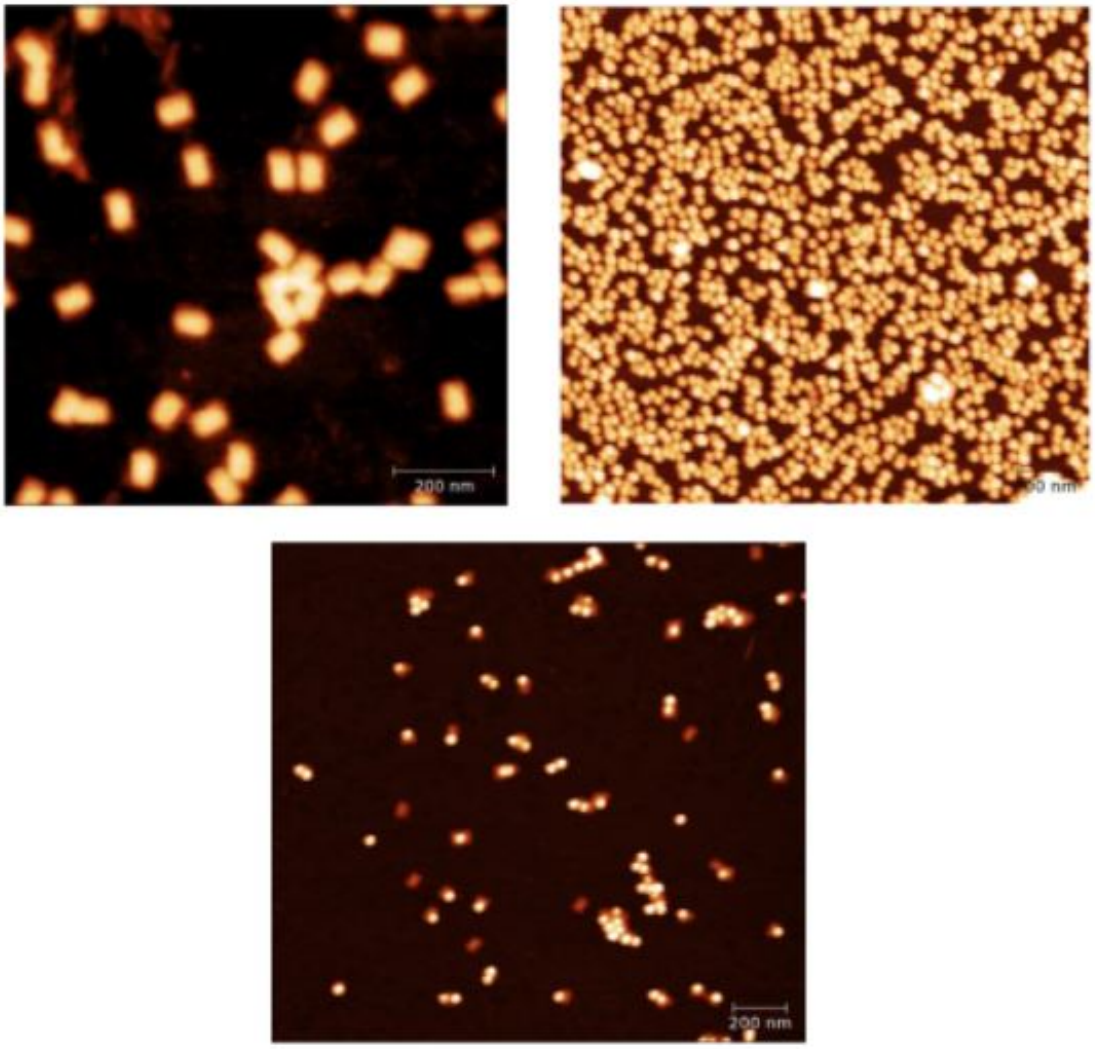

- Steffan Møller Sønderskov -

Institute of Physics and Nanotechnology
Aalborg University, Denmark
September 2016

AALBORG UNIVERSITY
STUDENT REPORT

Department of Physics and Nanotechnology
The Faculty of Engineering and Science
Aalborg University
Skjernvej 4A
DK-9220 Aalborg Ø, Denmark
Telephone 9940 9215
Fax 9940 9235
http://nano.aau.dk

Titel: Nanophotonics circuits formed by DNA self-assembly
Project period: September 3rd, 2015 - September 15th 2016

Author:
Steffan Møller Sønderskov

Project Supervisor:
Leonid Gurevich

Copies: 3
Pagecount: 113
Number of appendices: 5 (A, B, C, D and E)

Completed: September 15, 2016

Abstract:

This thesis investigated the use of DNA origami as the structural element in a nanophotonics circuit consisting of gold nanoparticles placed with high precision. Theoretical predictions on the fluorescence enhancement of the ATTO-647N dye in the gap of gold nanoparticle dimers were made. It was found that the dye was enhanced 385 times when in a gap of 15 nm surrounded by 100 nm particles. Predictions were also made for other gap and particle sizes. The evidence of the correct self-assembly of an 18 hb DNA origami structure was difficult to determine due to the small size, although AFM and agarose electrophoresis both pointed to the formation of an origami structure. Self-assembly of a 42 hb origami structure was found to proceed correctly according to gel electrophoresis while AFM imaging showed well-defined and correctly folded structures. Conjugation of 15 nm gold nanoparticles onto the 42 hb structure was found to achieve a high success-rate of approximately 91 % in addition to precise placement.

AALBORG UNIVERSITET
STUDENTERRAPPORT

Institut for Fysik og Nanoteknologi
Det Teknisk-Naturvidenskabelige Fakultet
Aalborg Universitet
Skjernvej 4A
DK-9220 Aalborg Ø, Danmark
Telefon 9940 9215
Fax 9940 9235
`http://nano.aau.dk`

Titel: Nanofotonisk kredsløb skabt ved DNA selv-samling
Projekt periode: 3. september, 2015 - 15. september 2016

Forfatter:
Steffan Møller Sønderskov

Projekt vejleder:
Leonid Gurevich

Antal kopier: 3
Antal sider: 113
Antal af bilag: 5 (A, B, C, D og E)

Afleverings Dato: September 15, 2016

Abstract:

I dette speciale blev det undersøgt hvorvidt DNA origami kunne anvendes som struktur-element i et nanofotonisk kredsløb bestående af guld nanopartikler. Teoretiske forudsigelse vedr. fluorescens stigningen af ATTO-647N i en guld nanopartikel dimer hul blev udarbejdet. Stigningen blev fundet til at være i omegnen af 385 for en hul-størrelser på 15 nm omgivet af 100 nm partikler. Forudsigelser blev også udarbejdet for andre hul-størrelser samt partikel størrelser. Bevis for en korrekt selv-samlet 18 hb DNA struktur var udfordrende pga. dens størrelse. Dog pegede både agarose gelelektroforese samt AFM undersøgelser på, at en origami struktur var blevet dannet. Den korrekte selv-samling af 42 hb origami struktur kunne ses ud fra agarose gelelektroforese samtidig viste AFM analyse også veldefineret og korrekte foldede strukturer. Konjugeringen af 15 nm guld nanopartikler til en 42 hb DNA origami struktur blev fundet til at opnå en succesrate på 91 % foruden en præcis placering.

Preface

This master thesis is authored by a nanobiotechnology student at the department of Physics and Nanotechnology at Aalborg University. The thesis project began the 3^{rd} of September 2015 and lasted until the 15^{th} of September 2016. The reader will benefit from having a prior understanding of DNA nanotechnology, electromagnetism and optics at the university level.

Reading guide: References to various sources throughout this report will be denoted in brackets as [∗], where a given number refers to a specific source in the bibliography. Each article source will have the author names, title, journal and year of publication as well as journal volume and article pages. Similar information will be given for book sources. References written before a period indicates information from that specific source is used in that particular sentence, while references written after a period means information from that source is used throughout the entire section.

Figures and tables are numbered by the chapter in which they are present. "Figure 1.2" refers to the second figure in the first chapter. The third figure would therefore be named "figure 1.3". The same system is used to number tables. All figures and tables will have a brief description of the content. If no sources are present, the figure has been constructed solely by the author. If the source is followed by "inspired by", the figure has been remade using the information gathered from an existing figure from that source. Lastly, if a standard source is given, the figure of the book or article has been used.

The front-page contains AFM images of the 42 hb, 15 nm Au-NPs and the successful conjugation of 15 nm Au-NPs onto the 42 hb.

Abbreviations:

AFM:	Atomic Force Microscopy
APTMS:	3-Aminopropyl)trimethoxysilane
Au-NP:	Gold nano-particle
BSPP:	Bis(p-sulfonatophenyl)phenylphosphine
DNA:	Deoxyribonucleic Acid
DLVO:	Derjaguin Landau Verwey Overbeek
dNTP:	Deoxyribonucleotide triphosphates
EDL:	Electric double-layer
FEF:	Fluorescence enhancement factor
hb:	helix-bundle
HR-SCC:	High-Resolution Solid Carbon Cone
kb:	kilo-base
MNP:	Metal nano-particle
NMWL:	Nominal Molecular Weight Limit
TB:	Tris-base Boric acid
TECP:	(tris(2-carboxyethyl)phosphine)
UV-VIS:	Ultraviolet-Visible
QE:	Quantum efficiency

Contents

1 | Introduction

Metal nano-particles (MNPs) have been shown to possess unique optical properties due to the ability to support surface plasmons, which result in the occurrence of interesting scattering and absorption phenomena [1, 2]. Gold nano-particles (Au-NPs) are promising candidates as central components in nano-optical circuits partly due to the above mentioned properties but also the relatively easy synthesis process of a wide range of particle sizes and shapes. [3] One of the main issues is controlling the precise geometric placement of individual components ensuring optimal control of the electro-magnetic profile. Using existing optical lithographic techniques present several challenges and limitations that have turned some focus into the development of buttom-up self-assembly approaches. [4]

The solution to this problem may be solved by using DNA as the structural building block. DNA is capable of programmed self-assembly due to its unique molecular recognition properties. This has resulted in the creation of a wide range of complex motifs and structures that are not limited to either one or two dimensions. [5, 6] Additionally, DNA can be chemically modified allowing the incorporation of optically active elements such as Au-NPs and fluorophores enabling the formation of optical circuits and devices with nanometer precision [57].

In this project, the synthesis of small nano-photonic circuits using DNA origami and Au-NP/DNA conjugation techniques will be examined. Two separate structures will be designed to include Au-NPs at pre-defined positions and the coupling efficiency in addition to the folding success of each origami structure will be examined using TM-AFM. The structures are designed using available CaDNAno DNA origami software and the structural properties will be predicted using Cando finite-element analysis resources before final synthesis. Furthermore, general bio-physical properties of the above mentioned origami structures will be studied. The optical properties of an Au-NP dimer model system will be predicted using finite-element programs COMSOL and Lumerical. This will be done for several particle sizes and gap distances and the properties of an inserted dipole acting as a fluorephore will be examined. Lastly, the knowledge obtained will be used to quantitatively predict fluorescence enhancements.

1.1 General properties of DNA

DNA (deoxyribonucleic acid) is recognized as the fundamental building block of life that contains genetic information and instructions on the maintenance of all known living organisms. DNA was first isolated by Friedrich Miescher in 1869, while its role as the carrier of genetic information was subsequently suggested by Oswald Avery and co-workers in 1944. These findings were followed by years of research into the chemistry, structure and physical properties of DNA. This resulted in perhaps the most noteworthy finding in 1953 at which point Watson and Crick presented an accurate description of the double-helical structure of DNA. [7]

Chemical structure

The chemical structure of DNA consists of a bio-polymer known as a nucleic acid that is formed by linked monomer units named nucleotides through phosphodiester linkage. Nucleotides are composed of a phosphate, a deoxyribose and one of four nitrogenous bases as seen in figure. 1.1. Adenine and guanine are purines which consists of a pyrimidine ring fused to an imidazole ring while cytosine and thymine are pyrimidines consisting of a six-membered ring. [8]

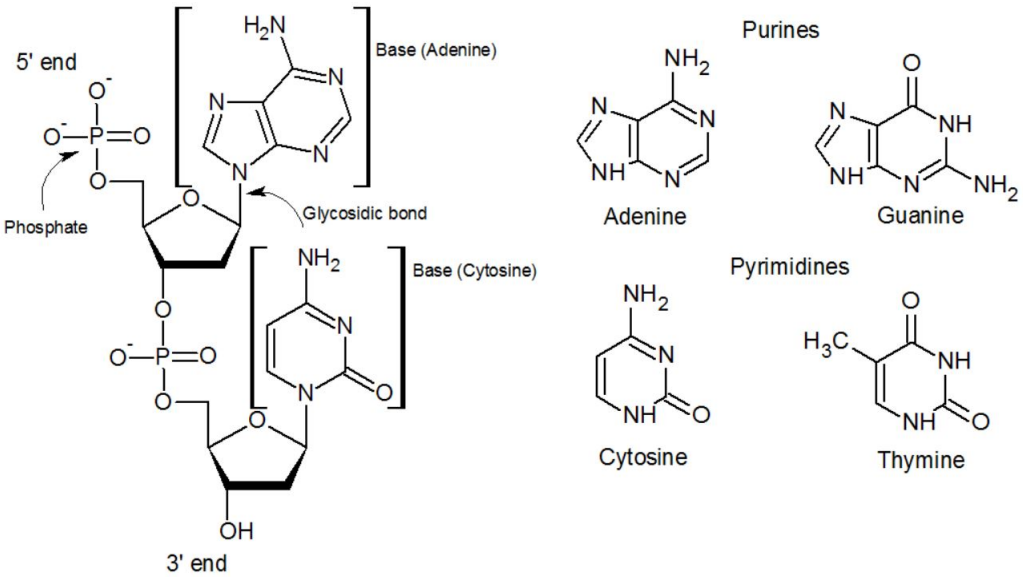

Figure 1.1: *The chemical structure of DNA and the four nitrogenous bases. Inspired by [8]*

Base-pairing

The nitrogenous bases of DNA have the property of pairing by hydrogen bonds in pairs of adenine(A)-thymine(T) and guanine(G)-cytosine(C). AT-pairs form two hydrogen-bonds, whereas GC-pairs form three resulting in stronger pairing. Base-pairing is illustrated in detail in figure. 1.2.

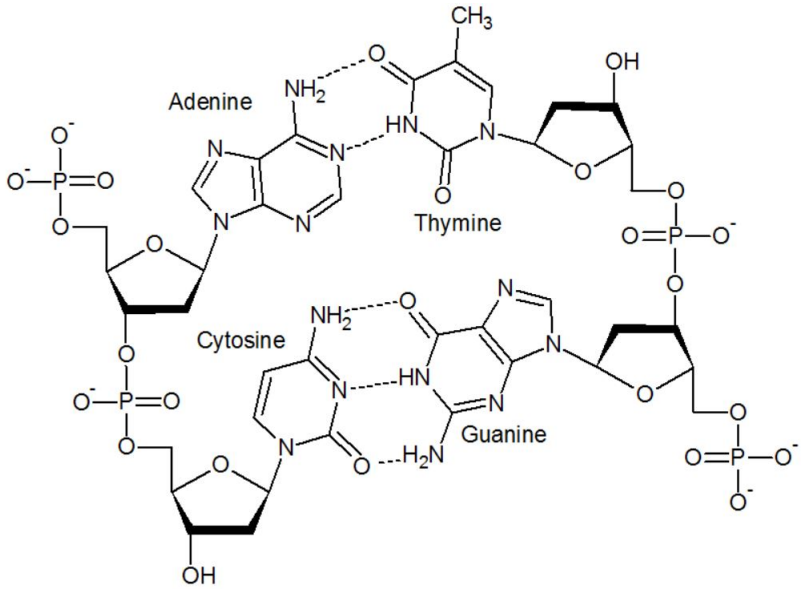

FIGURE 1.2: *Base-pairing of single-stranded DNA that illustrates the bonding of both AT and GC pairs. Inspired by [8]*

These conclusions were in agreement with the findings of E. Chargaff, who discovered that the ratio of adenine to thymine as well as cytosine to guanine in DNA was unity. The complementary base-pairing allows for highly specific inter- or intra-strand interactions resulting in double-stranded DNA. [9]

The physics of DNA base-pairing in solution can be explained by the Gibbs free energy, enthalpy and entropy contributions. Initially when two single-stranded complementary DNA are in a aqueous solution, water molecules form hydrogen bonds with the bases satisfying the hydrogen bonding properties. When complementary double-stranded DNA is formed, hydrogen bonds between bases and water are broken in favour of bonding between complementary bases. The formation of double-stranded DNA results in the displacement of water molecules which increases the entropy of the system, stabilizing the double helix. Additionally, electrostatic interactions (pi-pi) between stacked bases offer a contribution to the stability as well. Overall, the enthalpic contribution are favourable for both the solvent and DNA because of the formation of a larger H-network as well as base-stacking interactions. The entropic contribution is partly negative due to the highly ordered structure of double helix formation but is outweighed by the positive contribution due to water exclusion.

The ionic strength of the solution has an impact on the shielding of the phophoryl groups of the DNA backbone which are negatively charged. At no to very low salt concentration, the electrostatic repulsive forces inhibit the hybridization of single stranded DNA as well as stacking of bases. Thus, higher salt concentration shields these charges thereby stabilizing the double-helical formation. Divalent cations such as Mg^{2+} are effective and often used to promote the formation of double-stranded DNA [10]. High salt concentrations can on the other hand promote aggregation [11, 12].

Hence, the combined contributions due to base-stacking and base-pairing in addition to the physiological conditions determine the spontaneous formation of the characteristic double-helix structure of double-stranded DNA. [13]

Geometrical structure

The geometrical structure of B-DNA was formulated by Watson and Crick from x-ray diffraction patterns of hydrated DNA fibers. Their model of DNA includes two polynucleotide chains that wind into a helical structure with a right-handed screw sense. Moreover, the chains are anti-parallel which give them opposite polarity. The DNA sugar-phosphate backbone is highly solvent exposed contrary to the nitrogenous adjacent bases which are separated by a distance of 0.34 nm and located inside the helix which has a diameter of approximately 2 nm. Moving up the helix-axis, each base rotates 36 degrees corresponding to roughly 10 bases per helical turn. The major and minor grooves outlined in figure. 1.3 are structural characteristics of double-stranded DNA that can be attributed to the angle between glycosidic bonds of complementary bases. The glycosidic bond angles are respectively 120 and 240 degrees wide. As base-stacking proceeds, the narrow angle will give rise to a minor groove while the wide angle will result in a major groove. If the glycosidic bond angle was instead 180 degrees in all cases, each groove would be dimensionally indistinguishable. [8]

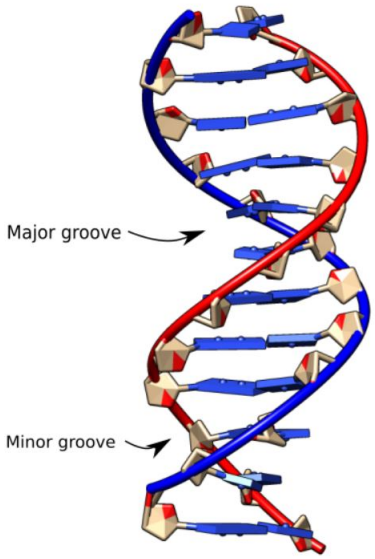

Figure 1.3: *The 3D structure of B-DNA. [14] Visualized with UCSF Chimera software*

The size difference in the major and minor groove results in an affinity preference for DNA-binding proteins and therefore has a significant role in processes such as DNA replication. [8, 15, 16]

In addition to the geometrical structure of B-DNA, DNA can exist in primarily the A-DNA and Z-DNA conformational states. X-ray diffraction studies of DNA at low humidity reveals the conformation of A-DNA. A-DNA has a lower rise per helix base pair of 0.23 nm and a helix packing diameter of 2.55 nm, which makes it shorter and broader compared to B-DNA. Additionally, it has a tilt of its bases of +19 degrees normal to the helix axis. Z-DNA consists of a left-handed helix and usually contains units of alternating purine and pyrimidine with the glycosidic bond in the syn conformation at purine residues and anti conformation at pyrimidine residues. The alternation of syn and anti conformations leads to

a zig-zag pattern of the backbone. The left-handed conformation for purine and pyrimidine alternating units is only observed in the presence of a high concentration of positively charged ions which effectively shield the negatively charged phosphate groups. Z-DNA has a slim and elongated structure with a rise per base of 0.38 nm and helix-packing diameter of 1.84 nm. [13, 17]

Stability of double-stranded DNA

Double-stranded DNA is one of the most structurally rigid known polymers with a persistence length of approximately 50 nm [18]. As double-stranded DNA is held together by non-covalent interactions, the mechanical properties of the double-helix structure are greatly susceptible to changes in the physical conditions of the surroundings. Alterations in temperature, ionic strength and pH of the DNA solution can induce the process of denaturation. Denaturation of DNA is a phase transition where the rigid and ordered structure of double-stranded DNA is converted to highly flexible and separated single-stranded DNA. [19]

Long double-stranded DNA is generally temperature stable below 70-90 °C. Heating a DNA solution beyond this temperature-limit disrupts the hydrogen bonds as well as the stacking forces resulting in thermal denaturation. Slowly cooling the solution generally results in annealing which is the correct pairing of the complementary single strands resulting in double-helix DNA. This process can be monitored by ultra-violet light-absorption of the bases at a wavelength of 260 nm. When a DNA double-strand is formed, base-stacking decreases the ability of the bases to absorb ultra-violet light. Contrarily, absorption is increased during denaturation, an effect termed hyperchromism. This can be studied by plotting the optical density of DNA vs. temperature. The mid-point of the transition from the double helical structure to the denatured state is the melting temperature (T_m) or temperature of mid-transition as seen in figure. 1.4

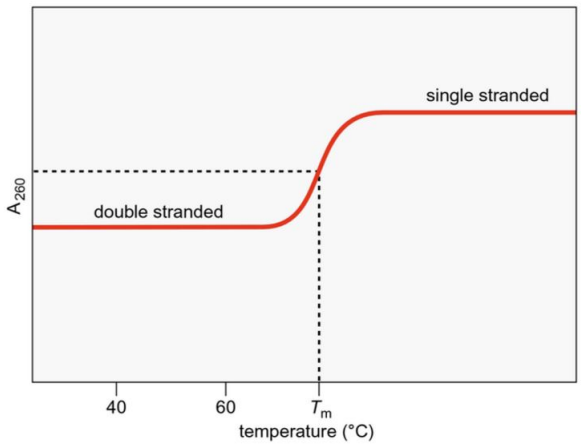

FIGURE 1.4: *Change in absorption of DNA as a function of temperature due to the effect of hyperchromism. Inspired by [13]*

The transition between single and double-stranded DNA can also be monitored by the use of DNA binding dyes such as SYBR green that has a strong coupling to double-stranded

DNA. Hereafter, the fluorescence is measured yielding near identical information as in figure. 1.4. The signals obtained from melting curve measurements from each method are differentiated with respect to the temperature to obtain temperature points where melting predominantly occurs.

The melting temperature of DNA is also influenced by the ratio of G:C and A:T content and the length. A higher percentage of G:C results in higher melting temperatures due to the additional stability of three hydrogen bonds contrary to two for A:T. Moreover, stacking interactions between G:C base-pair and their adjacent base-pair neighbour is more favourable.

Extreme pH often has a destabilizing effect on DNA leading to denaturation. At pH<3, protonation of cytosine's N(3) and adenine's N(1) occur which eliminates these as hydrogen-bond acceptors. At pH>10, deprotonation of guanine's N(1) and thymine's N(3) occur which eliminates these as hydrogen-bond donors. This is illustrated in figure. 1.5. Additionally, extreme pH may also either protonate or deprotonate all bases which will lead to mutual repulsion. [20]

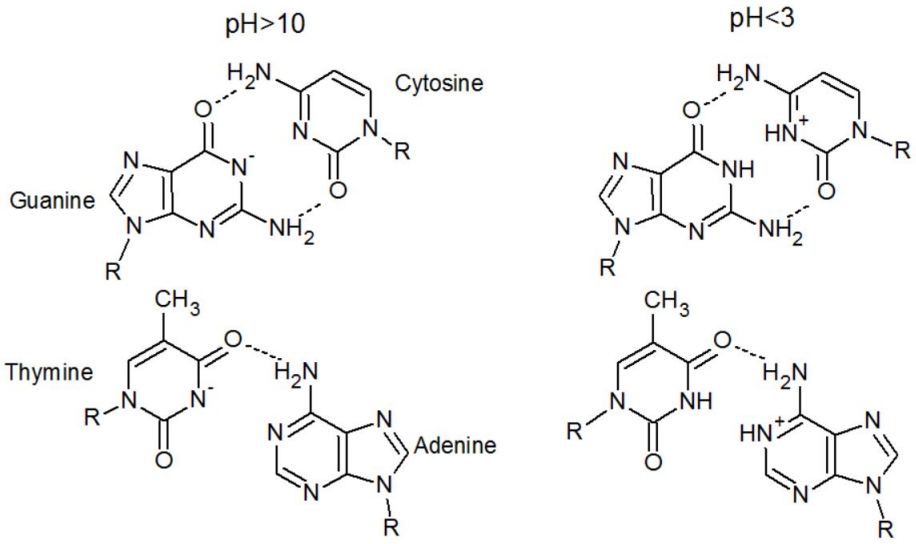

Figure 1.5: *The protonation state of DNA bases at different pH. Inspired by [20]*

Extreme pH may also irreversible cause damage to DNA in the form of hydrolysis or other bond-breaking mechanism as can high temperatures for prolonged periods of time. [21, 22].

Kinetics of DNA renaturation

The sharp increase in absorption at the melting temperature in figure. 1.4 is an indication that DNA denaturation and renaturation of complementary DNA strands is a cooperative process. It is theorized that the renaturation event itself involves two main steps in a second-order kinetic reaction. Initially, two DNA single-strands are in close proximity with a range of possible orientations that are not ideal for association. Due to solvent attractions as well as DNA jostling promoted by the electrostatic repulsive forces of phosphate groups, reorientation is achieved. The main step consists of partial molecular recognition between the two complementary strands forming a nucleation complex (rate-limiting step). The formation of the nucleation complex is theorized to be unstable depending on the temperature of the system, leading to either dissociation or further association. The second step consists of a rapid zippering from the nucleation site that results in the pairing of the remaining complementary bases. [19, 23]

Properties of single-stranded circular DNA

Circular single and double stranded DNA are well-known to have physical and topological properties that differ significantly from ordinary linear DNA. The topological changes are associated with the fact that circular DNA forms a closed loop. An example of a secondary structure that is often associated with double-stranded DNA is supercoiling, which occurs due to the twisting of circular double-stranded DNA in the same direction as its helical twist. Negative supercoiling is achieved by twisting in the opposite direction which results in unwinding. Supercoiling is an important mechanism done by the cell to prevent DNA degradation as well as denaturation. [24]

Circular single-stranded DNA is often prone to form intramolecular connections through base-pairing resulting in so called stem-loops. These are made when two separate regions are partially or fully complementary resulting in localized double-stranded DNA with an unpaired loop at the end. For stem-loops occurring in circular DNA, the order is greater which results in a stabilizing force that makes melting less likely. As several stem-loops are likely in single-stranded circular DNA, there is a significant chance that the overall secondary structure changes drastically resulting in different physical properties. [25]

1.2 Structural DNA nanotechnology

The role of DNA as the molecule containing genetic information is the reason why it is often discussed and researched in a biological context. However, Nadrian Seeman envisioned the use of DNA as a building material allowing precise programmable construction of structures and devices on the nano-scale. This idea was the foundation of the field of DNA Nanotechnology which covers the design and fabrication of artificial nucleic acid structures for various scientific and technological uses. [5, 26] DNA is an ideal building material on the nano-scale due to its unique mechanical and recognitional properties which are indispensable when creating stable structures for buttom-up self-assembly applications.

Furthermore, the sequence of chemically synthesized DNA is highly controllable ensuring a high level of programmability which is critical in order to obtain highly customized and correctly assembled structures with high yields. The chemical synthesis of DNA has been refined from years of experience which has led to the commercialization of DNA synthesis with affordable prices. The main issue is synthesis of DNA beyond 60 oligonucleotides. In this case, the yield starts to drop significantly because of error rates associated with the coupling of nucleotides leading to higher pricing. Additionally, commercial DNA synthesis also offers the opportunity to modify oligonuclotides with biotin, thiols, amines and fluorescent labels and more. This offers flexible options of combining the structural and active elements in few steps. [27]

Artificially engineered DNA structures

Numerous DNA nano-structures have been engineered since the first artificial structure in DNA nanotechnology was developed in 1991. Several designs are inspired by natural occurring structures such as the holliday junction which can be created using a multi-strand approach. This structure consists of four arms of double stranded DNA emerging from a central junction point as seen in figure. 1.6. [28]

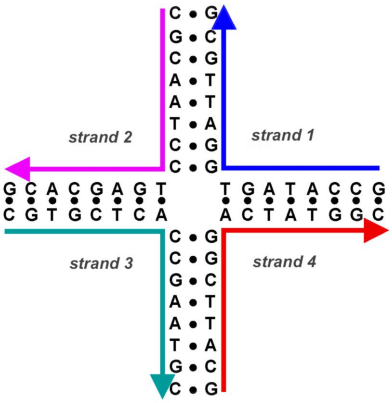

Figure 1.6: *Illustration of a Holliday Junction. [28]*

In biology, the structure is an important intermediate in the process of homologous recombination [29]. Furthermore, due to the symmetry of the nucleotide sequence, branch migration is possible enabling strands to move through the junction point leading to a

dynamic structure, whereas breaking the nucleotide symmetry ensures a fixed junction. Introducing sticky ends on the branch arms allows the option of coupling individual holliday junctions thereby principally enabling the formation of indefinite lines or 2D lattice structures. The junction structure can be slightly modified so that various components such as gold or silver nano-particles can be attached forming an array.

Additionally, several types of DNA motifs and tiles have been fabricated and used as building blocks using the multi-stand approach. Motifs are often engineered by the principle of reciprocal exchange, which results in new connectivities and often more rigid mechanical properties compared to conventional linear duplex DNA. The principle is illustrated in figure. 1.7 along with examples. [5]

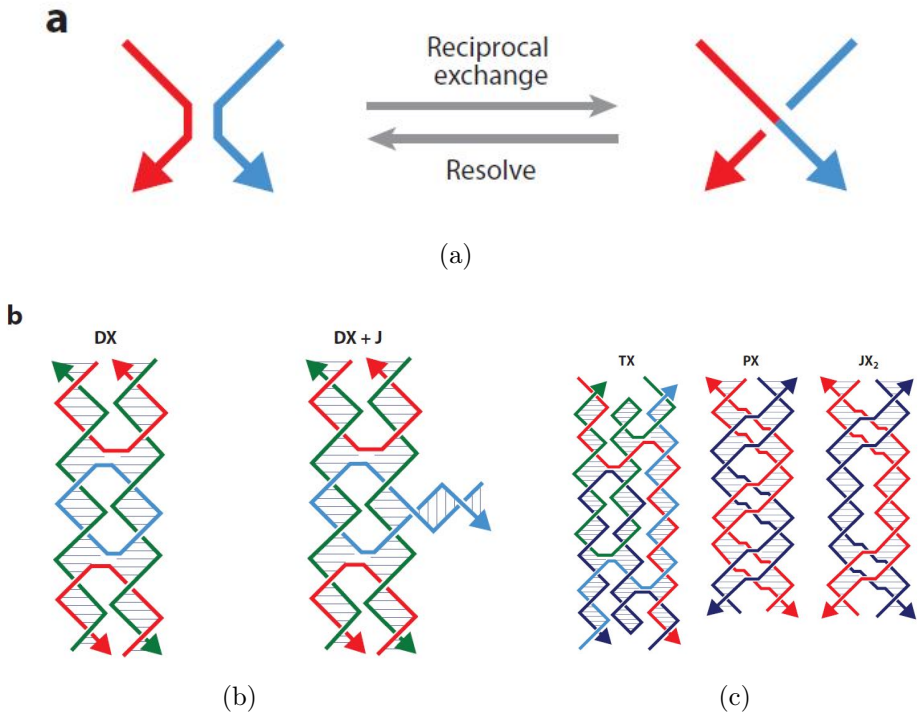

FIGURE 1.7: *Illustrations of motifs engineered by the principle of reciprocal exchange [5]*

The strategy of using DNA motifs and tiles to constructs structures have several disadvantages. Due to the relatively simple geometric shapes used, the complexity is often limited to lattice structures. Additionally, the formation of structures using short oligonucleotides requires a high level of stoichiometric control often followed by inter-step purification of the structures. These steps can be difficult and often error-prone resulting in time-consuming synthesis followed by low yields. [30]

1.2.1 DNA origami

In 2006, Paul Rothemund brought much attention to the scaffold-based DNA origami method. The approach consists of several single stranded oligonucleotides (staple strands) which arrange a single-stranded DNA (scaffold-strand) into a predefined geometrical shape by staple strand crossovers. The scaffold-strand is often the genome of a bacteriophage such as the m13mp18. This particular genome is preferable due to the known sequence, single-stranded nature, low cost as well as the substantial length of 7.25 kb, which offers the possibility of large and complex structures. Staple strands are chemically synthesized and usually consists of $\approx$ 25-50 nucleotides. The synthesis process of DNA origami structures proceeds by initially briefly heating the scaffold and staple-strand solution to 75-95 °C to disrupt any unwanted secondary structures. This is followed by slow cooling which allows separate regions to be connected by staple-strand cross-overs. [31] The annealing procedure can range from hours to days and can consist of a wide range of temperature rates and ramps that are often customised for a particular structure to ensure correct folding. Programs are often chosen depending on the complexity of the DNA origami structure, such as the overall shape, size and number of staple strands and their cross-over pattern. [6, 10] This method is illustrated in figure. 1.8.

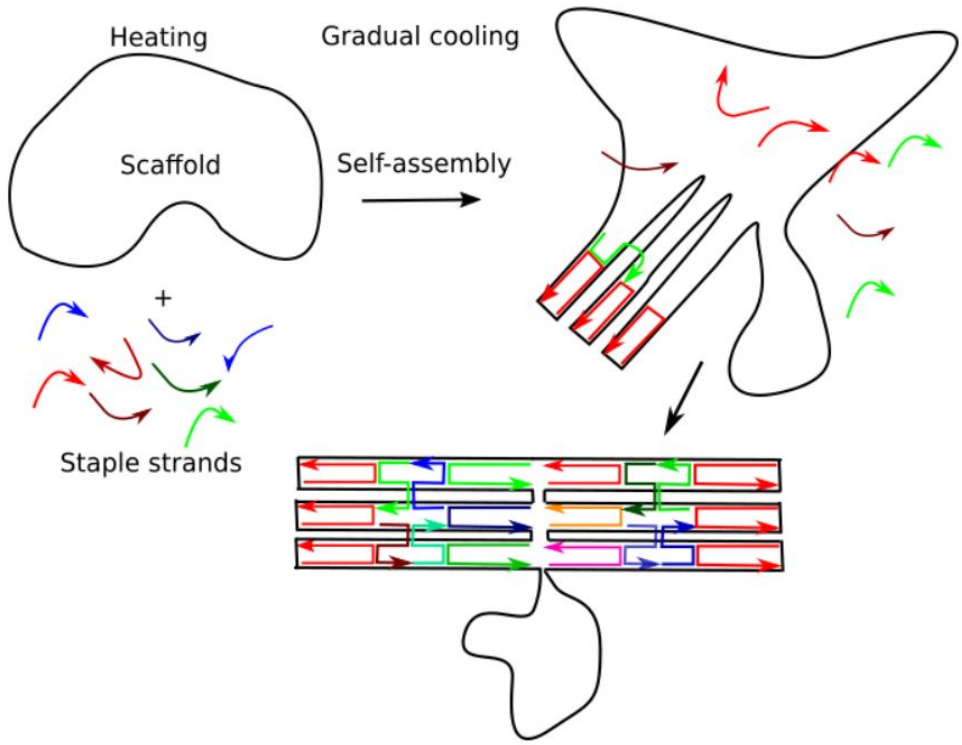

Figure 1.8: *Illustration of the scaffold-based DNA origami approach. Inspired by [30]*

Due to hybridization between staples with a common scaffold, relative staple-strand concentration is not critical contrary to several multi-strand assembly approaches in DNA nanotechnology. This avoids the fundamental issue of equal stoichiometry DNA self-assembly. Moreover, correctly folded DNA origami structures are partially determined by an initial correct arrangement of the scaffold strand. As more staples bind, the arrangement of the scaffold strand is funnelled closer to the final structure leading to more favourable correct

binding of the remaining staples making folding a highly cooperative process. [32, 33, 34] Due to the natural properties of DNA, the method of DNA origami allows the possibility of creating structures that can be fabricated with sub-nanometer precision. This results in the programmability of features with high precision and thereby a new method of creating structures. As DNA origami operates from the principle of parallel buttom-up self-assembly, this allows the possibility of large-scale parallel production. Moreover, staple-strands can be functionalized with a wide range of different elements resulting in highly customized DNA structures.

Formation of DNA origami structures at constant temperature

One of the central issues in DNA origami production has been a combination of low yield and in worse case week-long customized reaction-procedures for certain complex 3D structures. This has naturally challenged the potential practical applications of such structures. Lately, it was found that intricate 3D structures that usually required complex and long annealing procedures could be correctly folded after a couple of hours at a constant temperature denoted as the critical temperature. This is possible since many origami structures have a well-defined and unique cooperative folding profile. It has been found for several origami structures that complete base-pair formation proceeds at a narrow temperature interval of approximately 4 °C. The critical temperature is decided by the shape of the structure and staple strand sequences which requires prior study into the specific melting temperature profile of each structure. Logically, a sharply well-defined melting temperature is also dependent on the staple-strand crossover pattern following a defined strategy. [35, 36]

1.2.2 DNA origami design using caDNAno

Following the introduction of DNA origami, programs such as caDNAno have been made available which offer an interface where structures can be designed by the user by the ordering of the scaffold strand. Hereafter, the program introduces staple cross-overs which connect scaffold regions. As of now, the scaffold can be ordered in either a honeycomb or square lattice structure. [6, 37] Figure. 1.9 illustrates general design principles of DNA origami structures by examining a simple 6 helix-bundle structure.

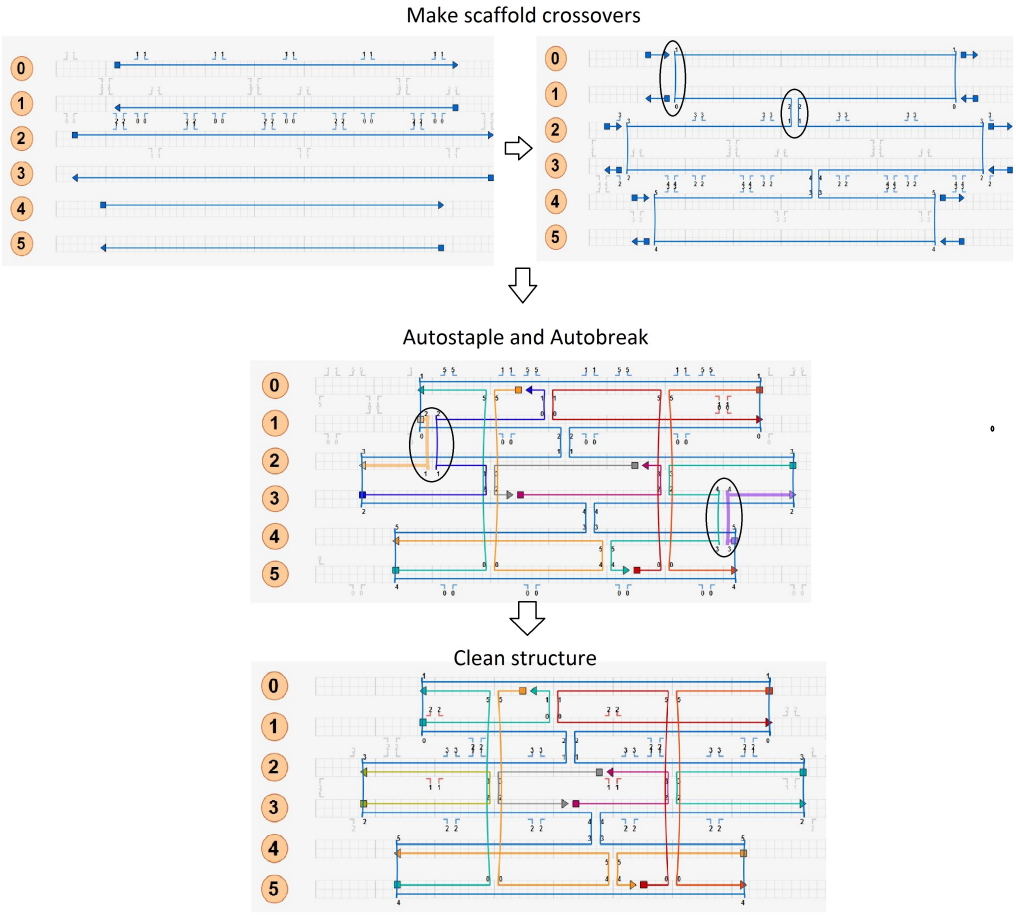

Figure 1.9: *Simple caDNAno design of a 6 helix-bundle DNA origami cylinder. The light-blue lines represent the scaffold strand which can be customized to create various shapes. Scaffold cross-overs can be created at selected positions resulting in helix-connection. Afterwards, staple cross-overs are introduced by the autostaple feature while auto-breaking breaks staples that have exceeded the recommended length. At times, the user must correct faulty staples that are usually too short and do not provide sufficient cross-over stability. [37]*

Contrary to much pre-existing structural DNA nanotechnology, DNA origami in conjunction with programs such as caDNAno, offer the possibility to create intricate 3D structures that do not require advanced pre-existing DNA motifs or architectures.

Following initial design in CaDNAno, files can be analysed using CanDo (Computer-aided engineering for DNA origami) where the mechanical flexibility is analysed using finite-element based modelling. The DNA double-helix is modelled as a homogeneous elastic

rod with mechanical properties that have been measured experimentally. This offers the possibility of predicting the mechanical properties of designed structures prior to the actual synthesis process. [38]

1.3 Surface plasmon resonance

Surface plasmon resonance is a physical phenomenon that is generated when light induces resonant oscillations of conduction band electrons in nano-particles or thin films of noble-metals and alike. [39] Metals have plasma-like properties due to the non-localized conduction electrons and can therefore be estimated as a free electron gas in the presence of a positive nuclei lattice [40].

1.3.1 Localized surface plasmon resonance

In the case where a noble-metal nano-particle is exposed to incident light, it is subjected to an oscillating electric field which in turn, at certain frequency ranges, induces a collective coherent oscillation of the conduction band electrons. This results in the separation of negative charge relative to the positive nuclei lattice thereby forming an oscillating electric-dipole as seen in figure. 1.10. [1]

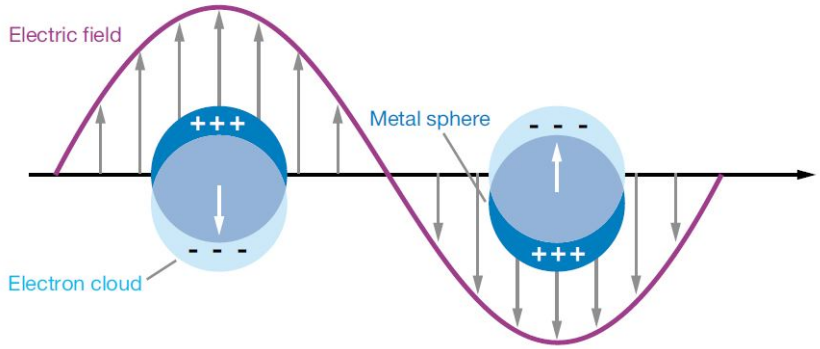

Figure 1.10: *Light-induced dipole oscillation in a metal nano-sphere. [41]*

Due to the presence of electric charges that oscillate, electromagnetic fields are created in the vicinity of the nano-particle surface. This phenomenon can also be explained by light inducing longitudinal electron-density waves which in turn creates electromagnetic waves. A single surface plasmon is defined as the quantum of the electron plasma oscillations and its associated electromagnetic field near a metal surface. Localized surface plasmons are trapped light-waves confined to the surface of nano-particles much smaller than the wavelength of incident light. [39, 42]

The conditions at which localized surface plasmon resonance occurs in spherical nano-particles can be derived by finding the electric field and corresponding electric potential in and around a small sphere. In the quasistatic approximation where the diameter of the sphere is $D \leq \frac{\lambda}{10}$, the electric field strength of the incoming light is treated as homogeneous across the particle at a point in time. [43, 44] An electric field is related to the electric potential and the charge density by the following expressions:

$$E = -\nabla V \tag{1.1}$$

$$\nabla \cdot E = \frac{\rho}{\varepsilon_0} \tag{1.2}$$

Combining eq. 1.1 and eq. 1.2 gives the electric potential dependence on the charge density and the permittivity of the surrounding medium.

$$\nabla \cdot \nabla V = \nabla^2 V = -\frac{\rho}{\varepsilon_0} \tag{1.3}$$

As there are no free charges present in either the sphere or the surrounding medium, eq. 1.3 is simplified resulting in the LaPlace equation which is:

$$\nabla^2 V = 0 \tag{1.4}$$

The solutions to the LaPlace equation inside and outside of a sphere with radius R, are given in spherical harmonics and are respectively:

$$\begin{aligned} \varphi_1(r,\theta) &= A_1 r cos\theta + A_2 r^{-2} cos\theta, r < R \\ \varphi_2(r,\theta) &= B_1 r cos\theta + B_2 r^{-2} cos\theta, r > R \end{aligned} \tag{1.5}$$

The constants are solved from boundary conditions. A_2 is zero to prevent an infinite electric potential from forming as $r \to 0$. Moving far away from the sphere, the electric field is expected to have a uniformity which results in $B_1 = -E_0$. The remaining constants A_1 and B_2 are found from the following boundary conditions at the sphere-medium interface:

$$\varphi_1\Big|_{r=R} = \varphi_2\Big|_{r=R} \quad and \quad \varepsilon_p \frac{\partial \varphi_1}{\partial r}\Big|_{r=R} = \varepsilon_m \frac{\partial \varphi_2}{\partial r}\Big|_{r=R} \tag{1.6}$$

Where ε_p and ε_m are the permittivity of the particle and surrounding medium respectively. This results in the following:

$$A_1 R = -E_0 R + B_2 R^{-2} \quad and \quad \varepsilon_p A_1 = \varepsilon_m(-E_0 - 2B_2 R^{-1}) \tag{1.7}$$

$$A_1 = -\frac{3E_0\varepsilon_m}{\varepsilon_p + 2\varepsilon_m} \quad and \quad B_2 = \frac{E_0 R^3(\varepsilon_p - \varepsilon_m)}{\varepsilon_p + 2\varepsilon_m} \tag{1.8}$$

Inserting the obtained constants yields the solution to the electric potential inside and outside a particle.

$$\begin{aligned} \varphi_1(r,\theta) &= -\frac{3E_0\varepsilon_m}{\varepsilon_p + 2\varepsilon_m} r cos(\theta) \\ \varphi_2(r,\theta) &= -E_0 r cos(\theta) + \frac{E_0 R^3(\varepsilon_p - \varepsilon_m)}{\epsilon_p + 2\varepsilon_m} r^{-2} cos(\theta) \end{aligned} \tag{1.9}$$

Using the relation in eq. 1.1 together with the expressions for the electrostatic potential in eq. 1.9 at $\theta = 0$, yields the electric field in and outside the particle along the center.

$$\begin{aligned} E_1\Big|_{\theta=0} &= \frac{\partial \varphi_1}{\partial r}\Big|_{\theta=0} = \frac{3E_0\varepsilon_m}{\varepsilon_p + 2\varepsilon_m} \\ E_2(r)\Big|_{\theta=0} &= \frac{\partial \varphi_2}{\partial r}\Big|_{\theta=0} = E_0 + \frac{2E_0 R^3(\varepsilon_p + \varepsilon_m)}{\varepsilon_p + 2\varepsilon_m} r^{-1} \end{aligned} \tag{1.10}$$

The scattered potential obtained is identical to that of a dipole with a dipole moment of [45]:

$$P = 4\pi\varepsilon_m R^3 \frac{\varepsilon_p - \varepsilon_m}{2\varepsilon_m + \varepsilon_p} E_0 \tag{1.11}$$

Where ε_p can be expressed as:

$$\varepsilon_p = \varepsilon_{p1}(\omega) + i\varepsilon_{p2}(\omega) \tag{1.12}$$

Resonant enhancements occur when the Frohlich condition is met, that is when $|2\varepsilon_m + \varepsilon_p|$ is minimum. In the case where $i\varepsilon_{p2}(\omega)$ is small or weakly dependent on ω, the following holds true:

$$Re\left[\varepsilon_p\right] \approx -2\varepsilon_m \tag{1.13}$$

Evidently, the surface plasmon resonance conditions are given by the interplay of the wavelength dependent permittivity ε_p of the particle and the permittivity ε_m of the surrounding medium. This interplay can be physically explained by the mutual polarizing effect by the particle and the medium. The charge density inside the sphere has to adjust to both the field of the incident light as well as the fields caused by polarization effects resulting in wavelength dependent resonance. The plasmon resonance position is found to be red-shifted if the di-electric constant of the medium is increased. This can be used to monitor local changes in the medium surrounding the nano-particle. Additionally, $\varepsilon_2(\omega)$ determines plasmon peak width and height. [43, 46] Moreover, increasing the size of the nano-particle red-shifts the wavelength of plasmon resonance. This can physically be explained by the increasing distance between charges on opposite sides of the particle, which results in the weakening of the restoring force and thereby their interactions also known as damping. [45]

Enhanced light absorption and scattering of gold nano-particles

An electromagnetic wave interacting with matter experience loss of energy from either absorption or scattering processes. Light absorption occurs when the energy of the photon is converted into internal energy of the material. Light scattering results from photon induced electron oscillations when incident light strikes an obstacle. Electron oscillations are a source of electromagnetic radiation, thereby resulting in the re-emission of light with a propagation direction different from that of the incident light. Light scattering is predominantly described by either Rayleigh or Raman scattering. Rayleigh scattering is an elastic process where the scattered light has the same frequency as the incident light whereas Raman scattering is inelastic with a frequency-shift in scattered light. [1] The sum of the energy removed by either absorption or scattering processes is termed as the extinction of light.

Scattering and absorption cross-sections are introduced which are the effective areas where scattering or absorption processes can occur. These are thereby also a measure of the probability of the occurrence of either of these processes and are defined as:

$$\sigma_{abs} = \frac{W_{abs}}{\mathcal{P}_{inc}} \qquad \sigma_{sca} = \frac{W_{sca}}{\mathcal{P}_{inc}} \tag{1.14}$$

Where σ_{abs} and σ_{sca} are the absorption and scattering cross-sections, $[m^2]$, W_{abs} and W_{sca} is the power absorbed and scattered by the particle, $\left[\frac{W}{m^2}\right]$. $\mathcal{P}_{inc}$ is the incident irradiance, $\left[\frac{W}{m^2}\right]$. In the quasistatic limit, the absorption and scattering cross-section of a plasmonic

nano-particle can be expressed as: [47]

$$\sigma_{abs} = 4\pi k a^3 Im\left[\frac{\varepsilon_p - \varepsilon_m}{\varepsilon_p + 2\varepsilon_m}\right] \quad \sigma_{sca} = \frac{8}{3}\pi k^4 a^6 \left|\frac{\varepsilon_p - \varepsilon_m}{\varepsilon_p + 2\varepsilon_m}\right|^2 \tag{1.15}$$

Comparing the absorption and scattering expression in eq. 1.15, it is implied that as the particle size decreases, absorption will dominate over scattering.

The highly surface-localized electromagnetic field due to surface plasmons enhances both the absorption and scattering properties of Au-NPs greatly. The calculated ratio of the per micron scattering- and absorption coefficient found in literature is highly dependent on the size, shape and metal-dielectric composition which results in highly tunable properties. In the case of gold nanospheres, an increase in size results in an increase in the ratio and thereby better scattering properties which is in agreement with eq. 1.15. [48]

Localized surface plasmon resonance coupling

It has previously been stated that single Au-NPs showing localized surface plasmon resonance have enhanced electromagnetic fields at the surface. When two or more Au-NPs are brought into close proximity of each other, near-field coupling occurs with the result of hotspots located in the gap-region with electric-field enhancements. Coupled plasmon modes can be attributed to coulomb attraction between opposite polarization charges on both sides of the gap between the Au-NP dimers. As such, charges are concentrated at the surface areas adjacent to the shortest gap distance resulting in local field enhancements. This electric field enhancement in the gap occurs only if the electric field of incident light oscillates parallel to the gap. [49] The electric field profile of such a system is illustrated in figure. 1.11.

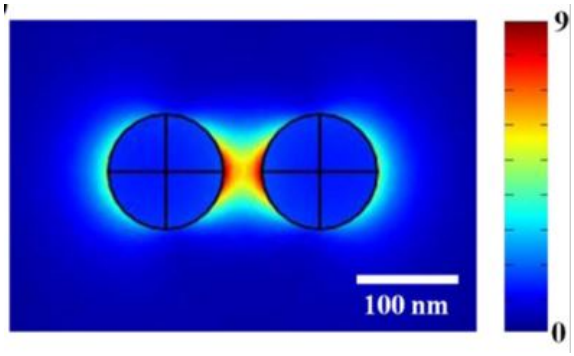

FIGURE 1.11: *Electric field profile of an Au-NP dimer with 100 nm particle diameter and a separation distance of 40 nm obtained by finite element methods. The system is irradiated with light at 633 nm with an electric field strength of 1 V/m [50]*

1.3.2 Surface plasmon polaritons

The properties of surface plasmon phenomena confined to small geometries have previously been accounted for. The other case to be considered is the set-up where incident p-polarised light enters a system consisting of a prism with a higher refractive index (n_2), a metal film usually consisting of either gold or silver and lastly a lower refractive index material (n_2) such as air or water. This is illustrated in figure. 1.12

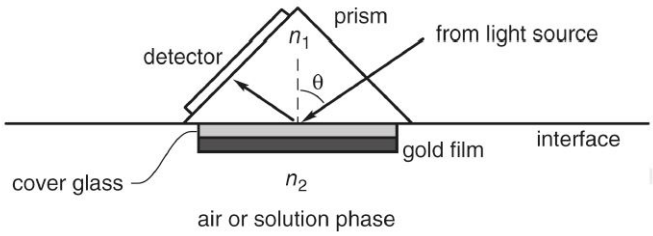

Figure 1.12: *Light entering a prism-dielectric-gold set-up [51]*

As light travels directly from a higher to lower index material, total internal reflection will occur if the incident angle θ, is greater than the critical angle θ_c, where the following relationship holds true: $sin(\theta_c) = \frac{n_2}{n_1}$. At conditions of total internal reflection, standing evanescent waves are formed that penetrate into medium 2 meanwhile transmitting zero energy across the interface. If a gold film with a thickness of $\approx$ 50 nm is placed at the interface, the evanescent wave will be enhanced and penetrate both the metal and the metal-medium 2 interface. The surface-parallel component of the wave-vector of the evanescent wave can be formulated as: [51]

$$k_{evan,||} = \frac{2\pi}{\lambda} n_1 sin(\theta) \tag{1.16}$$

The penetration of the evanescent wave can result in the excitation of conduction band electrons in the metal forming a surface plasmon polariton (SPP) whereby a decrease in the amount of reflected light can be monitored. [51] SPPs are contrary to localized surface plasmons, electromagnetic excitations propagating on the interface of a metal and di-electric that can travel in the x- and y-direction with an evanescent electromagnetic field normal to the direction of propagation as seen in figure. 1.13 [42]. The physical properties of SPPs can be derived by solving the wave-equation for a metal and di-electric layer [53]. Hereafter, the solutions are matched between the layers by using appropriate boundary conditions. The dispersion relation is described in eq. 1.17. A detailed derivation is shown in appendix A.

$$\beta = k_{spp} = k_0 \sqrt{\frac{\varepsilon_1 \varepsilon_2}{\varepsilon_1 + \varepsilon_2}} \tag{1.17}$$

This can be re-written in terms of the wavelength of light and the refractive index of the medium as:

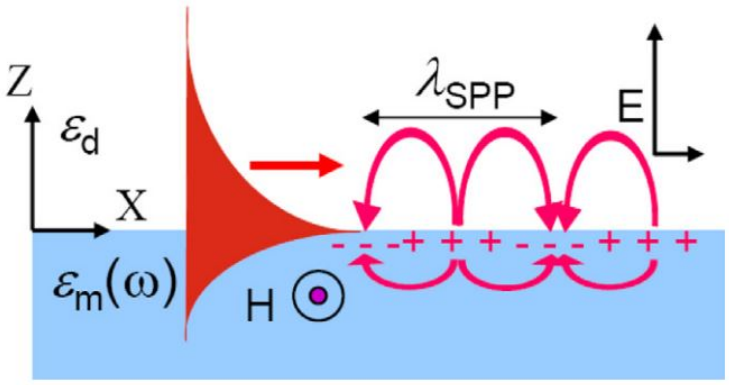

FIGURE 1.13: *Surface plasmon polaritons propagating along a metal and dielectric interface. [52]*

$$k_{spp} = \frac{2\pi}{\lambda}\sqrt{\frac{n_1^2 n_2^2}{n_1^2 + n_2^2}} \tag{1.18}$$

Equating eq. 1.16 and eq. 1.18 and rearranging gives the angle of incoming light at which SPPs are excited and thereby the conditions for surface plasmon resonance.

$$\theta_{spr} = sin^{-1}\left(\frac{1}{n_1}\sqrt{\frac{n_1^2 n_2^2}{n_1^2 + n_2^2}}\right) \tag{1.19}$$

SPPs dispersion profile

The dispersion of free space photons and SPPs are compared in figure 1.14. It is seen that SPPs have a larger momentum than free space photons at the same frequency. Thus, the incident plane-wave light in free space provides inadequate momentum for the excitation of SPPs and thereby no coupling can occur. Momentum gain is achieved if light is passed through a prism with a high refractive index accounting for the design choices in the Kretschmann configuration. [52, 54]

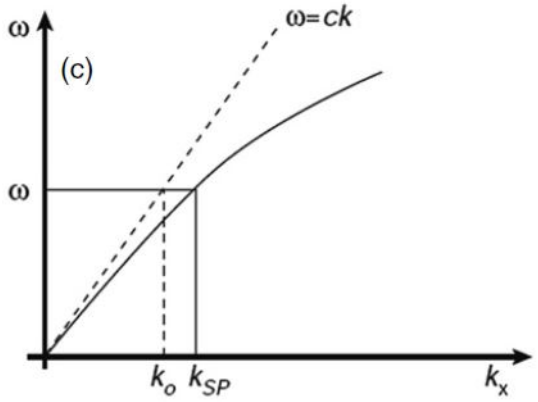

Figure 1.14: *Comparison of the dispersion relation of free space photons and a surface plasmon. [52, 54]*

1.4 Principles of fluorescence

Luminescence is the physical process where light is emitted from any material due to radiative relaxation from an electronically excited state. Luminescence phenomena include fluorescence and phosphorescence which are distinguishable by the properties of their excited state which can either be in an electronic singlet state in the case of fluorescence or a triplet state in the case of phosphorescence. The excitation of the electronic state can occur by the absorption of light with the subsequent emission of photons followed by the relaxation of the electronic state. [54, 55] The electronic processes of fluorescence can be explained by a simplified Jablonski diagram seen in figure. 1.15.

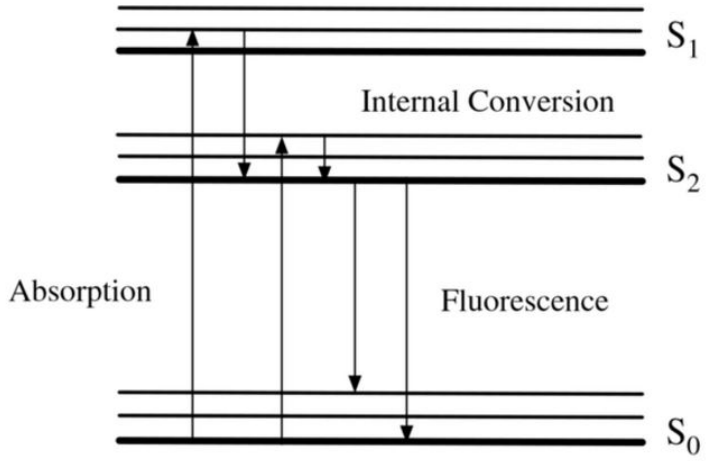

FIGURE 1.15: *Jablonski diagram illustrating the concept of fluorescence. A fluorophore subjected to incident light might absorb energy in the form of light which causes excitation into a higher vibrational energy level. This is followed by the rapid relaxation into the lowest vibrational state of S_1, a process termed internal conversion. Lastly, a final relaxation occurs from the S_1 electronically excited state to the electronic ground state possibly emitting a photon. [54]*

Even though light is absorbed, the subsequent emission of photons may not occur at all. The probability that a given excited fluorephore will emit energy in the form of a photon during the transition from the excited state to the ground state is defined by the quantum yield. If light emission does not occur, relaxation of excited fluorophores through the transfer of non-radiative energy to the surroundings will happen.

1.4.1 Fluorescence enhancement and quenching

Fluorescence emission can be enhanced and decreased due to various processes. The decrease of fluorescence is termed quenching and can be attributed to for instance fluorophore-molecule collisions or donation of a fluorophore's excited electrons to Au-NPs. [55] Energy transfer processes are also possible through the near-field coupling to guided waves such as surface plasmons. The efficiency is dependent on the distance and the dipole orientation of the fluorophores. All result in the non-radiative decay of the excited state.

Fluorescence enhancement can be attributed to local electric field enhancements that results in increased excitation rates and fluorescence probability. [56] In the case of an Au-NP dimer, the strong associated electric field in the gap due to plasmon coupling can provide greatly enhanced fields that theoretically can produce fluorescence enhancement of over 100 times [57].

Fluorescence enhancement and quenching is also observed for fluorophores located close to plane metal surfaces. In the kretschmann configuration, the evanescent electric field associated with surface plasmon polaritons can enhance the excitation rate similarly to previous cases. This can also provide an alternative method of monitoring the conditions of surface plasmon resonance. Alternatively, fluorophores located at distances approaching the surface experience intense quenching due to energy transfer and energy dissipation in the metal surface. Quenching can also occur by fluorophore energy flow providing momentum to surface plasmon polaritons. [58]

The fluorescence enhancement factor of a fluorescent dye located near one or several Au-NPs can be quantitatively calculated by its quantum yield and the local electric field. In the case of a single fluorophore, the enhancement is expressed as: [59, 60]

$$\frac{\gamma_{em}}{\gamma_{em}^{\circ}} = \frac{\gamma_{exc}}{\gamma_{exc}^{\circ}} \frac{q}{q_0} \quad where \quad \frac{\gamma_{exc}}{\gamma_{exc}^{\circ}} = \frac{|E|^2}{|E^{\circ}|^2} \tag{1.20}$$

Where $\frac{\gamma_{em}}{\gamma_{em}^{\circ}}$ is the ratio of the radiative emission rate of a fluorophore in an inhomogeneous to a homogeneous environment. $\frac{\gamma_{exc}}{\gamma_{exc}^{\circ}}$ are the excitation rates and are linked to the strength of the local electric field (E). Specifically, the quantum yield of the fluorophore in the absence and presence of single Au-NPs or Au-NP dimers, respectively q_0 and q, can be expressed in terms of the decay rates of the excited fluorophore through radiative and non-radiative decay channels:

$$q_0 = \frac{\gamma_r^{\circ}}{\gamma_r^{\circ} + \gamma_{nr}^{\circ}} \quad and \quad q = \frac{\gamma_r}{\gamma_r + \gamma_{nr} + \gamma_{abs}} \tag{1.21}$$

Where γ_{nr}°, γ_r° and γ_{nr}, γ_r are the non-radiative and radiative decay rates in the absence and presence of the Au-NPs respectively. The presence of Au-NPs introduce the γ_{abs} decay-channel which is non-radiative and thereby acts as a source of quenching. The ratio of the quantum yield of the fluorophore in the presence of the nano-particle and the intrinsic quantum yield of the fluorophores gives the following:

$$\frac{q}{q_0} = \frac{\gamma_r}{\gamma_r q_0 + \gamma_{nr} q_0 + \gamma_{abs} q_0} \tag{1.22}$$

Assuming that the Au-NP does not influence the value of γ_{nr}, $\gamma_{nr}^{\circ} = \gamma_{nr}$ holds true. By dividing every term in eq. 1.22 with γ_r°, normalized decay rates are obtained which leads to the following:

$$\frac{q}{q_0} = \frac{\gamma_{r-o}}{\gamma_{r-o} q_0 + \gamma_{abs-o} q_0 + (1 - q_0)} \tag{1.23}$$

1.5 Nano-particle formation and growth

The formation of nano-particles is described by classical nucleation which is the process whereby a small crystalline-like nuclei is formed by the arrangement of a small number of atoms, ions or molecules via self-assembly. The small nuclei formed act as seeds for further growth. Homogeneous nucleation will be studied in this section which in contrary to heterogeneous nucleation does not occur on the surface of a system. [61]

For homogeneous nucleation to occur, the solute has to exceed its equilibrium solubility. The high Gibbs free energy of the supersaturated solution can be reduced by forming a solid phase meanwhile maintaining an equilibrium concentration. The change of Gibbs free energy per unit volume of the newly formed solid phase can be written as:

$$\Delta G_v = \frac{-kT}{\Omega} ln\left(\frac{C}{C_0}\right) \tag{1.24}$$

Where C and C_0 are the concentration of the solute and the equilibrium concentration respectively. Ω is the atomic volume while k and T are the Boltzmann constant and the temperature. As seen from eq. 1.24, without supersaturation it is energetically unfavourable to form a solid phase. Accompanying ΔG_v, is the surface energy of formed particles which counter balances the previous term. This results in the total change of Gibbs energy for a spherical particle with radius, r being:

$$\Delta G = \Delta\mu_v + \Delta\mu_s = \frac{4}{3}\pi r^3 \Delta G_v + 4\pi r^2 \gamma \tag{1.25}$$

Where γ is the surface energy per unit area. Figure. 1.16 shows a schematic illustrating how the energy contributions behave as a function of particle radius, r.

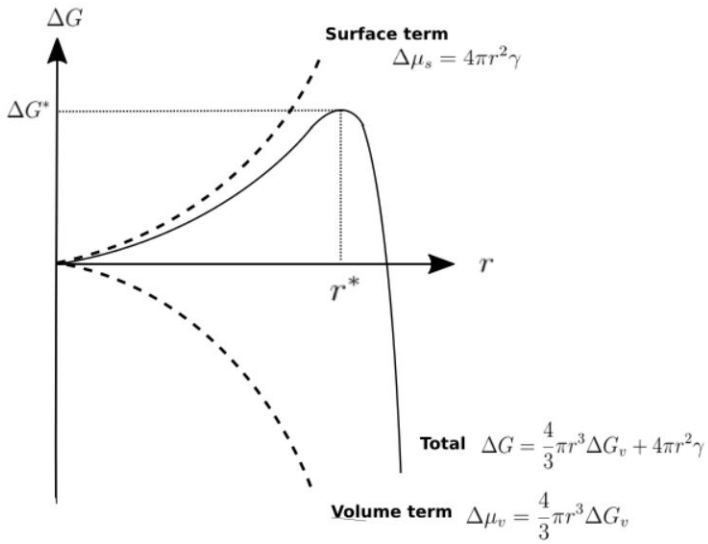

FIGURE 1.16: *Schematic illustrating the free energy contributions as a function of particle radius, r. Inspired by [61]*

Stable nuclei will only form for nuclei larger than $r^* = r$, as these nuclei have overcome the energy barrier and continue to grow and reduce their free energy. Nuclei with a radius

smaller than $r^* = r$ will reduce their free energy by redissolving. Subsequent growth of NPs is summarized by the kinetics of monomer diffusion to the nuclei surface followed by surface reaction kinetics. Several theories exist on the mechanisms of nucleation formation and growth of nano-particles. [62]

1.5.1 LaMer mechanism

The LaMer theory consists of a three-step mechanism. At first there is a concentration increase of free monomers in solution due to the decomposition of precursor chemicals, such as heating chloroauric acid. Following this, monomers aggregate by burst nucleation when the concentration of monomers reaches supersaturation levels. As monomers continuously aggregate on existing nuclei, monomer concentration naturally decreases. As the monomer concentration decreases below $C_{min}nu$, nucleation formation stops and subsequent growth relies on diffusion and surface reactions. Continuously adding precursor material which becomes decomposed will continue particle growth. A schematic of this mechanism is seen in figure. 1.17. [62]

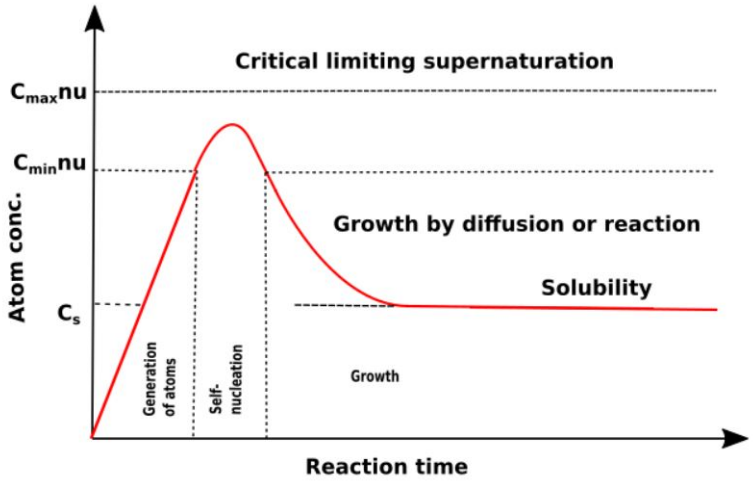

Figure 1.17: *Diagram illustrating the mechanism of particle formation and growth. Inspired by [62]*

1.5.2 Ripening effects

The size distribution of NPs in solution results in that the physical properties of each NP may differ significantly. As smaller particles have a higher solubility as well as surface free energy compared to larger ones, smaller particles are more prone to redissolve. This in turn results in the formation of even larger particles. This phenomenon is known as Ostwald ripening.

Instead of ripening effects proceeding between individual particles, intra-particle ripening is possible as well. Under some conditions, single monomer units in solution can have a slightly lower or equal energy compared to the surface energy of one of the crystal facets of the NPs. This low difference in free energy results in no net diffusion of monomers in the

bulk onto the particle surface. Some of the crystal facets can have larger energy which will result in one facet dissolving and a lower energy facet growing. [63, 64]

1.5.3 Formation and growth of gold nano-particles

In the case of Au-NPs, two primary formation pathways are theorized that are dependent on either acidic conditions of pH 3.7-6.5 or higher pH of 6.5-7.7. In each case, the particles are synthesised using standard citrate recipes, where the reduction agent trisodium citrate is injected into a boiling solution of tetrachloroauric acid. Each formation pathway is shown is figure. 1.18

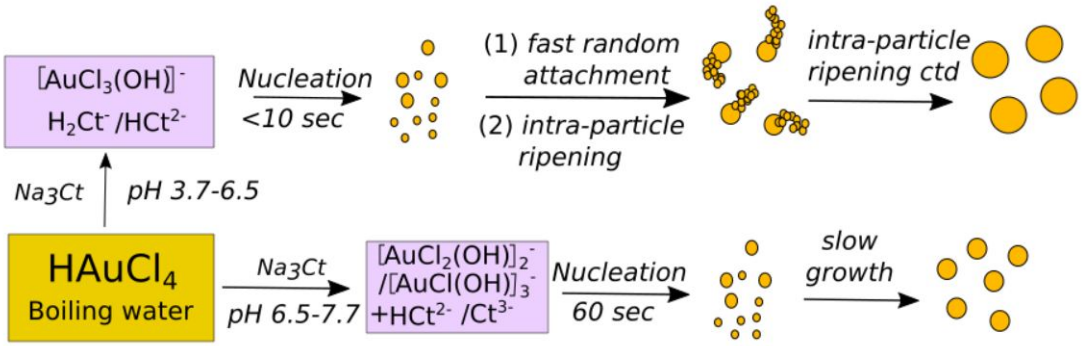

FIGURE 1.18: *Formation pathways of Au-NPs using standard citrate reduction at different pH. Inspired by [62]*

The synthesis reaction connecting the formation of gold nuclei clusters from the precursor material is theorized to follow one of two pathways. The first pathway consists of gold ions that undergo complete reduction into zerovalent atoms followed by aggregation into nuclei and further growth. The other pathway is where a cluster complex of unreduced gold material is formed followed by full reduction. Each pathway is described in eq. 1.26 and eq. 1.27 respectively. [65]

$$\begin{aligned} M^{x+} + xe &\rightarrow M^0 \\ M^0 + M_n^0 &\rightarrow M_{n+1}^0 \end{aligned} \tag{1.26}$$

$$\begin{aligned} M^{x+} + e &\rightarrow M^{(x-1)+} \\ M^{(x-1)+} + M^{(x-1)+} &\rightarrow M_2^{(2x-2)+} \\ M_2^{(2x-2)+} + xe &\rightarrow M_x \end{aligned} \tag{1.27}$$

1.5.4 Nano-particle aggregation and stabilization

A suspension of nano-particles is not thermodynamically stable and therefore tend to aggregate into clusters over time. Initially, Brownian diffusion causes nano-particle collision and thereby allow short-range thermodynamic processes to occur. The attachment efficiency is calculated according to whether the short-range forces present result in net-attractive or net-repulsive contributions. Particle aggregation is often described by the DLVO (Derjaguin-Landau-Verwey-Overbeak) theory. Classical DLVO considers the thermodynamic surface interactions between two spherical particles and predicts whether or not sticking will occur by summing the attractive van der Waals force and the repulsive electric double layer force. [66]

The van der Waals interactions are comprised of a set of forces that originate from three types of dipole interactons: [67]

- Keesom interactions refer to dipole-dipole interactions of permanent dipoles such as those found in polarised molecules.
- Debye interactions are observed due to the fact that a permanent dipole creates an electric field which can induce a dipole in a neighbouring molecule thereby creating an attractive force.
- London dispersion forces describe how non-polar but polarizable molecules can attract each other through instantaneous dipoles.

Electrostatic double-layer forces on the other hand arise due to the initial adsorption of ions on the particle surfaces followed by loosely bound opposite charges due to coulomb attraction and thermal motion. As separate particle surfaces with similar potential profiles approach each other, the individual EDLs will at some point overlap which will result in surface repulsion. [66] The potential profile of ions adsorbed onto a Au-NP is seen in figure. 1.19.

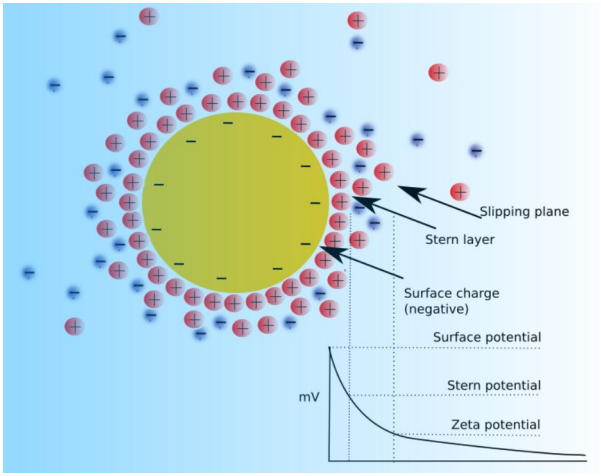

Figure 1.19: *Schematic showing the interplay between a negatively charged Au-NP and ions in solutions in addition to a simple potential profile. Inspired by [68]*

Figure. 1.20 depicts how van der Waals and EDL forces behave at different separation distances as well as the sum of these forces.

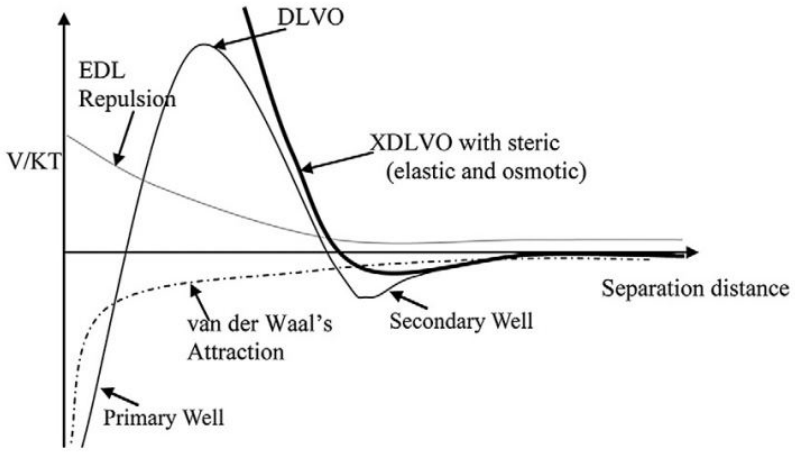

FIGURE 1.20: *Schematic illustrating the free energy contributions at distances away from a particle surface. [61]*

Methods of stabilization Stabilization of Au-NPs is usually done by ions that effectively adsorb on the surface such as citrate or BSPP (Bis(p-sulfonatophenyl)phenylphosphine) in the presence of low ionic strength, high ionic strength can result in charge neutralization and thereby particle aggregation. Another possibility includes the use of polymers one of which is the use of DNA bridged to the particle surface by interactions between gold and an added thiol-group or by interactions between gold and single dNTPs. [69]

2 | DNA origami designs

Two separate structures will be investigated in this report. Both designs are conceived to be the structural element in the optical investigation of primarily two set-ups.

In the first system illustrated in figure. 2.1, the origami structures will act as bridges in an Au-NP dimer set-up with a pre-defined separation distance. This is engineered to be used for fluorescence enhancement of a dye. Au-NP conjugation will be attempted through two methods. In the first method, selected staple strands will be thiolated thereby connecting the Au-NPs and the origami structure. In the second method, Au-NPs will be coupled to thiolated strands composed of poly-dT sequences. This will later couple to origami through poly-dA overhang sequences on selected staple strands. Au-NPs are expected to be separated by a distance of 15-20 nm according to modelling. A clear difference in the fluorescence properties of the dye is expected to occur when the system is irradiated by linearly polarised light. The position of the dye was chosen to be in the center of the gap.

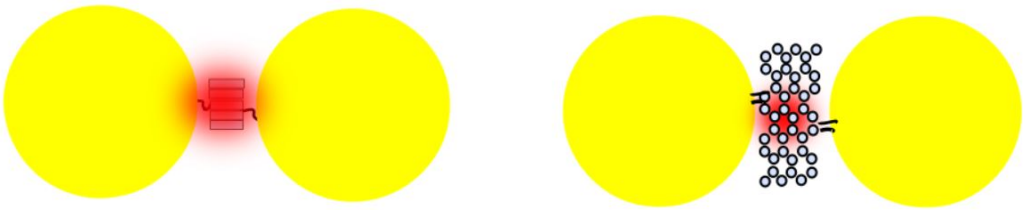

(a) (b)

FIGURE 2.1: *Au-NP dimer created using two separate DNA origami structures. The set-up will act as a nano-antenna.*

In the second set-up illustrated in figure. 2.2, the origami structures are meant to be deposited on a metal-film/glass-prism surface stabilized by interactions between the gold surface and thiolated staple strands. Afterwards, Au-NPs are meant to be deposited on top of the origami structures. The set-up will allow fluorescence enhancement studies in a total internal reflection fluorescence set-up.

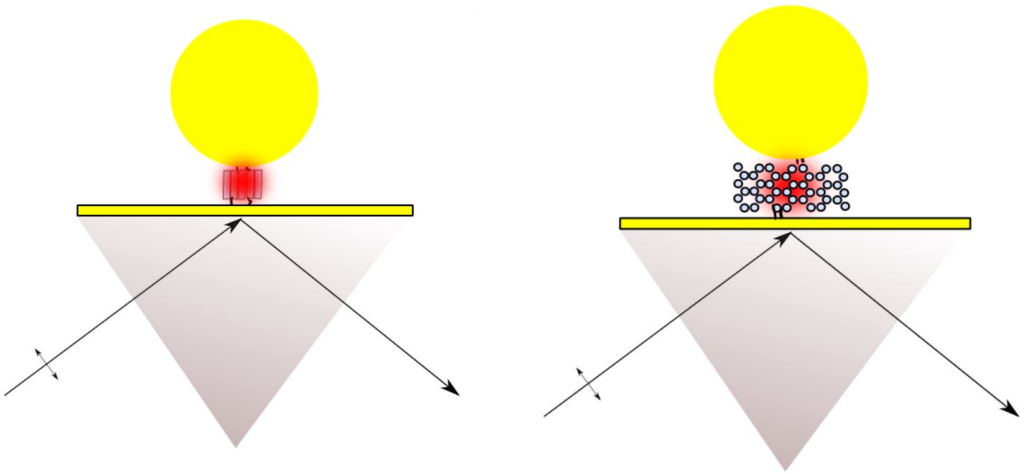

(a) (b)

Figure 2.2: *DNA origami structures acting as separators between a gold film and a single Au-NP with a fluorophore located in between.*

2.1 18 helix-bundle DNA origami design

The first engineered DNA origami structure consists of a 18 helix-bundle (hb) designed using caDNAno software. The scaffold is held together by 22 staple-strands forming a structure with approximate dimensions of 18x17x15 nm. Figure. 2.3 shows a 3D model of the design in the form of adjacent barrels representing the individual helices as well as a slice-view of the scaffold obtained in caDNAno.

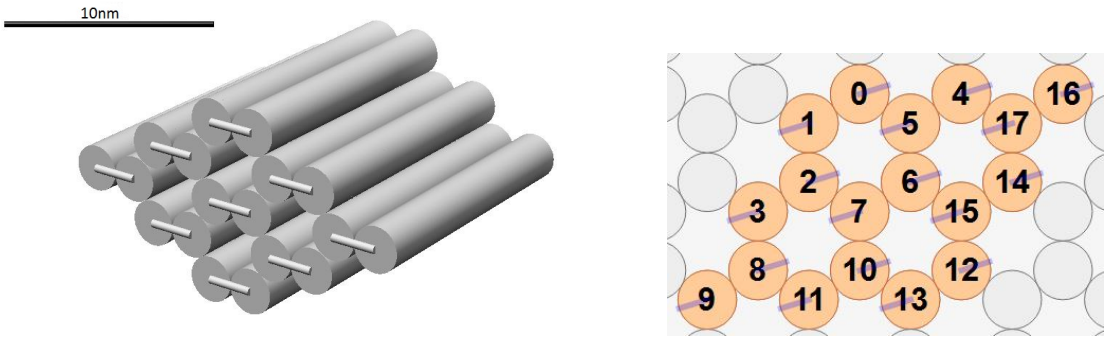

(a) (b)

FIGURE 2.3: *3D model of the 18 hb DNA origami structure visualized with UCSF Chimera software in addition to a slice-view of the scaffold obtained in CaDNAno*

The complete caDNAno design with the scaffold and staple arrangements are found in appendix B.1. The staples are arranged as to accommodate binding at the ends of helix 6 and 7 to gold surfaces and Au-NPs using thiolated modifications. The break-point of the scaffold is located on helix 9 pointing away from the structure to minimize any kinetic traps or mis-folding during the annealing step. Additionally, any neighbouring scaffold and staple-strand cross-overs are separated by 10 bases or less have been purposefully avoided as kinetic traps may arise. The scaffold-strand helices are connected in pairs along one direction to ensure that each helix bundle is equal in length as well as each end of the origami structure is planar. This is done to ensure that nano-particle binding should proceed more successfully and that the structure should be more rigid when binding to the metal-film lowering the possibility of tipping. As only approximately 10 % of the scaffold is used for this particular structure, it is possible to synthesize a separate neighbouring origami structure using flanking scaffold DNA. A possible design is seen in appendix. B.3 where the two structures are meant to be connected via a short DNA bridge.

2.2 42 helix-bundle DNA origami design

The next structure is a 42 helix-bundle cuboid structure that was originally published by Martin et. al. [70]. The structure has been slightly re-designed in cooperation with Tilibit Nanosystems for the use in fluorescence enhancement experiments. The 3D model is viewed in figure. 2.4.

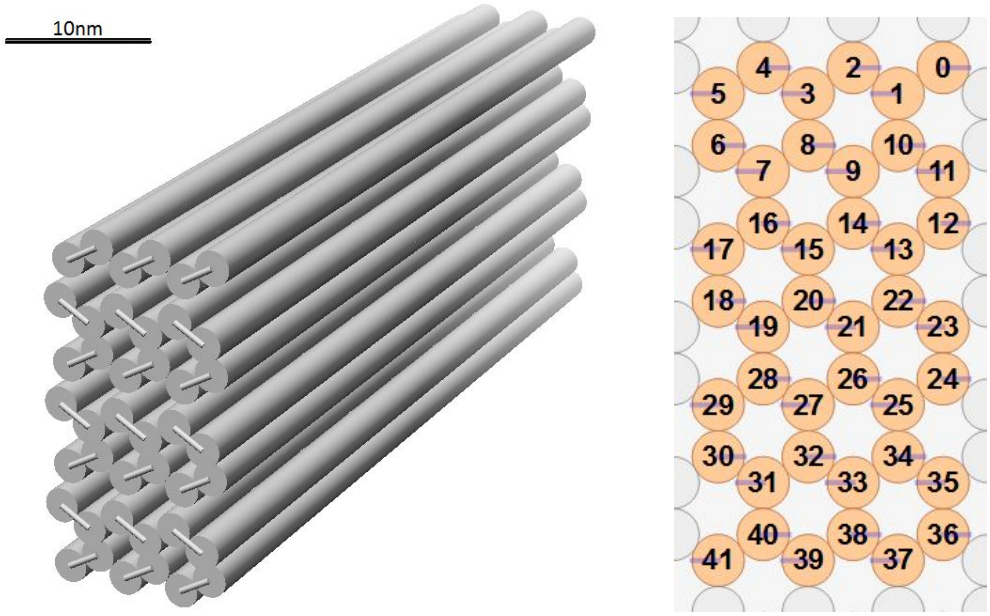

(a) (b)

Figure 2.4: *3D model of the 42 hb DNA origami structure visualized with UCSF Chimera software in addition to a slice-view of the scaffold obtained in CaDNAno*

The dimensions are approximately 14 nm x 27 nm x 59 nm and the bundle ends of the structure are originally passivated with staple strands containing 5 poly-dTs. The entire design schematic and staple arrangement is seen in appendix. B.2.

3 | Computational simulations

3.1 CanDo simulation

The mechanical properties of the 18 helix-bundle design is computationally predicted using the resource CanDo (Computer-aided engineering for DNA origami) in order to gain insight into the degree of mechanical stability before actual DNA origami synthesis. The simulation was done for the 42 helix-bundle as well in order to compare possible structural differences and give reasons for these. Simulations were performed with default geometric values of B-DNA with a axial rise per base-pair of 0.34 nm, a helix diameter of 2.25 nm, a cross-over spacing of 10.5 bp and an inter-helical angle of 60 degrees. The mechanical properties are: Axial stiffness of 1100 pN, bending stiffness of 230 pN nm^2, torsional stiffness of 460, junction twist angle stiffness of 135.3 $pNnmrad^{-1}$ and a nick stiffness factor of 0.01. The model resolution is fine and the honey-comb lattice is used. The structures are coloured according to the root-mean-square-thermal fluctuations in nm, which thereby provides info on the structural properties.

3.2 Electric field and scattering/absorption cross-section simulations

The electric field profile along with the scattering/absorption cross-sections of Au-NPs attached to the DNA origami structure are investigated using the Radio Frequency module in COMSOL Multiphysics v5.1. The nano-particles are modelled as perfect spheres with diameters spanning between 2-80 nm separated by a distance of 5, 10, 15 and 20 nm. The simulations were performed in medium with properties identical to water, assuming this reflects the di-electric environment of the DNA origami structure and the surroundings. The relative permittivity of gold is obtained in the range of 400-800 nm in steps of 10 nm by extracting values from Johnson and Christy [71]. This is followed by interpolation in COMSOL. The incoming light is a plane-wave propagating perpendicular to the Au-NP dimer gap with an electric field of strength 1 $\frac{V}{m}$ oscillating parallel to the gap. The absorption and scattering cross-sections of a single Au-NP in both a monomer and dimer configuration are calculated between 400 and 800 nm in COMSOL according to the expressions formulated in eq. 1.14 by performing numerical integration. Commands used in COMSOL to find the scattering and absorption cross-sections can be found in manuals. [72, 73]

3.3 Fluorescence enhancement simulations

The quantum efficiency of a fluorophore in the presence of an Au-NP monomer or dimer is predicted using the FDTD Solutions photonic simulation and design software by Lumerical Solutions, Inc. The radiative and non-radiative decay data of a dipole obtained from the simulation is used to gain physical insight into the properties of an ideal dipole with intrinsic quantum efficiency of $q_0 = 1$. Furthermore, the data will be used to calculate $\frac{q}{q_0}$ of a dipole with quantum efficiency of 0.65 identical to the ATTO-647N. This will be done according to eq. 1.23.

The fluorophore is treated as a single point dipole located near Au-NPs with water as the surrounding medium. The dipole is set to emit radiation at wavelengths of 400-800 nm. Focus was put into 665 nm as this is the wavelength where the emission peak of the ATTO-647N dye occurs [74].

The fluorescence enhancement factor is calculated according to eq. 1.20 and 1.23. The electric-field strength that the dipole experiences is calculated in COMSOL. The dipole and the dipole-particle system are enclosed by boxes with power monitors registering the power emitting from the dipole and the dipole-particle system. The quantities are used to monitor the power absorbed by one or more Au-NPs. Decay-rates are calculated from the following relationship [75]:

$$\frac{\gamma_0}{\gamma} = \frac{P_0}{P} \tag{3.1}$$

Where $\frac{\gamma_0}{\gamma}$ and $\frac{P_0}{P}$ are decay rates and power radiation by the dipole in an environment where one or more Au-NPs are present. Separate simulations were performed while the dipole was in a parallel and perpendicular orientation with respect to the Au-NP surface. This was done in order to consider the physical effects and consequences of light emission from the fluorophores in different directions relative to the surface of the nano-particles.

The decay values obtained due to different orientations can be averaged according to [59]:

$$\frac{2\gamma_{parallel} + \gamma_{perpendicular}}{3} \tag{3.2}$$

A mesh size of 0.5 nm is used for the dipole and sphere region while a mesh accuracy of 4 is used for the region outside. The material properties are obtained from Johnson and Christy [71].

The simulation environment created will also be used to investigate and compare findings published by Acuna et. al. [57] of a fluorescence enhancement set-up using DNA origami as the structual element.

4 | Materials and methods

4.1 Chemicals

Table 4.1: *Chemicals used in DNA origami synthesis and analysis*

Chemical	Description/Classification	Manufacturer
p7249 scaffold		tilibit nanosystems
10x folding buffer XM		tilibit nanosystems
$MgCl_2$ solution		tilibit nanosystems
6x gel loading due		tilibit nanosystems
Agarose		Sigma-Aldrich (lot#100M9432V)
Boric acid	GHS08	Sigma-Aldrich (lot#106H1109)
DNase free water		Sigma-Alrich (lot#RNBD9146)
EtBr	GHS06, GHS08	Sigma-Aldrich (lot#00093172)
$MgCl_2$		Riedel-de Haen (lot#62650)
6X DNA loading dye		Thermo Scientific (lot#00097465)
GeneRuler 1kb DNA ladder		Thermo Scientific (lot#00093172)
Tris-base		Sigma-Aldrich (lot#110M54391V)

Table 4.2: *Chemicals used in nano-particle synthesis/imaging and DNA conjugation*

Chemical	Description/Classification	Manufacturer
APTMS	GHS05	Sigma-Aldrich (lot#BCBBL6126V)
Toluene	GHS02, GHS07, GHS08	Sigma-Aldrich (lot#STBF7647V)
BSPP	GHS07	Strem Chemicals (lot#A1726129)
Chloroauric acid	GHS05, GHS07	Strem Chemicals (lot#20992400)
Sodium borohydride	GHS02, GHS05, GHS06	Sigma-Aldrich (Batch#11404HH
Sodium chloride		In-house
TECP	0.5 M, pH 7 solution, GHS07	Sigma-Aldrich (lot#MKBW8503V)
Trisodium citrate		Sigma-Aldrich (lot#28H0209)

4.2 Lab procedures

4.2.1 DNA origami preparation

18 hb staple strands

The DNA origami staple strands for the 18 helix bundle structure were ordered and received in lyophilized form from SBS Genetech Co. Ltd (Beijing, China). Prior to opening the tubes containing DNA, each tube was briefly centrifuged to prevent any dislodged DNA material from escaping. Afterwards, each DNA oligo was suspended in DNase-free water at concentrations of 100 μM and divided into aliquots and stored at -20°C. The concentration of each oligo was measured using a P200 Picodrop Microliter Spectrophotometer (Picodrop Ltd., United Kingdom) using 1 mm thick proprietary tips. To find the concentration in pmol/μL, the onboard oligo program was chosen along with the proportions of bases of each respective oligo.

Staple-strand master-mix for 18 and 42 hb

A staple-strand master-mix for the 18 hb was prepared by pipetting 10 μl of each unmodified staple-strand stock solution on a piece of para-film and fusing the content into a bigger drop. The content was afterwards pipetted into an eppendorf tube yielding 220 μl of staple-strand master mix with a concentration of 4.55 μM per staple strand. The master-mix solution was aliquoted and kept at -20°C.

Core staple strands for the 42 helix bundle structure were ordered and received from Tilibit nanosystems in a prepared 746 nM solution. Poly-dT passivation strands were received in a separate 1539 nM solution. Staple strands with overhang were synthesized by Eurofins and received by Tilibit as were strands that accounted for slight modification of the design. These strands were prepared in a separate solution with a final concentration of 11.11 μM. All solutions were divided in aliquots and stored at -20°. Thiolated DNA strand for Au-NP conjugation was ordered from Eurofins and received in lyophilized form

Folding mixes

A 10-20 μl folding mix solution of the 18 hb and 42 hb is listed in 4.3 and 4.4. The $MgCl_2$ content will depend on eventual $MgCl_2$ screening tests.

TABLE 4.3: *The components and amounts in the folding mixture of the 18 hb (10 μl)*

Component	Amount (μL)	Final concentration
Scaffold, 100 nM	1 μL	10 nm
Folding buffer, 10x	1 μL	1x
$MgCl_2$	0.5 μl	10 mM
Unmodified oligos	2.20 μL	1 μM per strand
H_20	5.3 μL	

TABLE 4.4: *The components and amounts in the folding mixture of the 42 hb (20 μl)*

Component	Amount (μl)	Final concentration
Scaffold, 100 nM	4 μl	20 nM
Folding buffer, 10x	2 μl	1x
$MgCl_2$	2 μL	20 mM
Core staple strands	5.36 μL	200 nM per strand
Poly-T passivation strands	2.6 μl	200 nM per strand
Overhang and modified strands	0.72 μl	400 nM per strand
H_20	3.32 μl	

4.2.2 Annealing procedures

10-20 μl folding solution was prepared in 200μl PCR tubes followed by annealing using an Eppendorf MasterCycler Gradient system. A lid-temperature of 105° was used during all programs to prevent condensations.

As the 18 hb is an entirely new structure, different annealing programs were used in addition to a $MgCl_2$ screening by having samples with concentrations of 0, 4, 8, 12, 16 and 20 mM. The annealing programs programs used for the 18 hb structure are listed in table. 4.5.

Annealing procedures for the 42 hb were done according to a recommended program provided by Tilibit, where samples were subjected to 65 °C for 10 min followed by cooling from 60-40 ° at 1 h per °C. In addition, a constant temperature method was examined where samples were incubated at temperatures between 41 and 59°C in steps of 3°C over a 2 h period.

Table 4.5: *Annealing programs used for 18 hb formation*

(a) *Annealing program A*

Cycle number	Temperature and time
1	90 °C, 15 min
2-71	89 °-20 °C, 1 min per °C
73	Stay at 4 °C

(b) *Annealing program B*

Cycle number	Temperature and time
1	90 °C, 15 min
2-71	89 °-20 °C, 3 min per °C
73	Stay at 4 °C

(c) *Annealing program C*

Cycle number	Temperature and time
1	90 °C, 15 min
2-71	89 °-20 °C, 10 min per °C
72	Stay at 4 °C

(d) *Annealing program D*

Cycle number	Temperature and time
1	80 °C, 15 min
2-16	80 °-66 °C, 5 min per °C
17-52	65-30 °C, 30 min per °C
53	Stay at 4 °C

(e) *Annealing program E*

Cycle number	Temperature and time
1	80 °C, 5 min
2-16	80 °-66 °C, 1 min per °C
17-52	65-30 °C, 10 min per °C
53	Stay at 4 °C

4.2.3 Agarose gel electrophoresis

Gel imaging

Purification and initial quality control of the DNA origami structures were performed by agarose gel electrophoresis. Agarose gels were prepared by mixing 0.5-1 g agarose and 50 ml 0.5X TB-buffer (45 mM Tris-base and boric acid) buffer, pH 8.3 where-after the solution was microwaved until the agarose was fully dissolved. The solution was cooled down to 50-60 °C before adding 8 μl of 0.5 mg/ml EtBr and 550 μl of 1M $MgCl_2$ solution (final concentration 11 mM).

The gel was immediately poured into a casting tray and a comb was inserted. When the gel had solidified, the casting tray was put into an electrophoresis bath containing 0.5X TB-buffer and 11 mM $MgCl_2$ followed by immersion of the bath into ice-water. The samples were hereafter loaded and the gel was run at 65 V and 46 mA for 1.5-4 hours. The TB+$MgCl_2$ running-buffer was changed after 2 h to replenish the salt content in order to avoid denaturation of the origami.

Origami purification and extraction

20 μl folding solutions underwent annealing and were afterwards loaded onto agarose gels in two gel wells each containing 10 μL. The samples were separated in the agarose gel according to settings in section. 4.2.3. After the separation of the primary DNA origami band from excess staple strands could be visualised, the main band was cut out using a scalpel. The gel slice was placed into a dialysis tubing cellulose membrane bag (Sigma-Aldrich) with a width of 10 mm. Prior to this, a 5 cm long piece of membrane was cut and rinsed both inside and outside with DNA-free water. Afterwards, the tubing material was submerged into 0.5X TB-buffer containing 11 mM $MgCl_2$ at +4 °C for 1 h. Afterwards, one end was sealed with a clamp followed by rinsing with buffer. Following the insertion of the gel material in the tubing bag, 100 μl of 0.5X TB-buffer containing 11 mM $MgCl_2$ was added. The other end of the tubing material was sealed and the bag was placed in an electrophoresis bath perpendicular to the flow of electricity. The material was run at 65 V for approximately 45 min followed by 65 V for 2 min at opposite polarity.

The concentration of DNA origami was measured by absorption on a P200 Picodrop Microliter Spectrophotometer (Picodrop Ltd., United Kingdom) using 1 mm thick proprietary tips. For the 18 and 42 hb origami structures, a molar mass of $4.48 \cdot 10^6 \frac{g}{mol}$ and $4.66 \cdot 10^6 \frac{g}{mol}$ were used respectively in addition to a mass attenuation coefficient of $0.020 \frac{\mu g}{ml}$ [76] for double-stranded DNA.

4.2.4 Au-NP synthesis and modification

Synthesis of 5 and 15 nm particles

The synthesis of Au-NPs in this study was done according to citrate and modified citrate reduction methods. The basic recipe was adopted from Turkevich. et. al. [77].

5 nm citrate-coated Au-NPs were synthesized at room temperature primarily by using $NaBH_4$ as the reduction agent. 177 mL of deionized water was added into a 250 mL flask followed by the addition of 80 μL of 0.53 M chloroauric acid under vigorous stirring. 1.8 mL of 50 mM trisodium citrate was hereafter added followed by a 10 min wait without stirring. Lastly, 0.45 mL of 0.5 M cold and freshly prepared solution of sodium borohydride was added under stirring. The particles were stored overnight at room-temperature.

15 nm citrate coated Au-NPs were prepared by standard citrate reduction methods. A 150 ml solution containing 0.5 mM of chloroauric acid was heated to approximately 95 °C on a hot-plate. 15 ml of a 38.8 mM tri-sodium citrate solution was added under stirring. The solution was left for 6 min and the colour was noted to change from light-yellow to purple and lastly burgundy red. Afterwards, the solution was left to cool at room-temperature overnight. Both batches were afterwards kept at +4°C for long-term storage.

Size determination

The size and growth of synthesized Au-NPs were investigated by absorption measurements using an UV-1800 UV-VIS spectrophotometer (Shimadzu, Japan) using Greiner Bio-One semi-micro cuvettes.

Absorption was measured at wavelengths between 400 and 800 nm with a step-size of 0.5 nm and a scan-speed of 1 nm/sec. Absorption measurements of both batches of synthesized Au-NPs were also done after 2 days, 1 week and 1 month to examine their stability. Additional information regarding the size and size-distribution was attempted using NanoSight LM10 Instrument.

In the case of 5 nm Au-NPs, immediately after adding $NaBH_4$, 7 absorption measurements were conducted with a 10 min interval to investigate if the growth could be monitored. Afterwards, measurements were done every hour for a total of 5 hours.

Ligand exchange and up-concentration

Ligand exchange of citrate for BSPP was done by adding 0.2 mg/mL of BSPP to a 15 mL Au-NP solution followed by slow shaking at 1 Hz at room-temperature in an incubator. Afterwards, the entire content was poured into Centriprep centrifugal filters with Ultracel YM-50 membranes and a NMWL of 50000. The content was centrifuged at 1000 g for 15 min followed by decanting of the water. This was repeated until a concentrate of 1 mL was achieved.

Au-NP DNA conjugation

40 μl of 200 μM thiolated 15 poly-dT oligo was mixed with TECP (final concentration 20 mM) for 1 h at room temperature. 30 μl of concentrated Au-NP solution was mixed with 30 μl of oligo solution in the presence of 89 mM Tris-base and Boric acid as well as 50 mM NaCl and stored in a shaking incubator at 1 Hz room at temperature for 60 h. 20 μl solution was run on a 2% agarose gel containing 0.5x TB buffer at 100 V and 20 min. A solution containing Au-NP at an identical concentration was run as a reference. The band of interest was cut and put into a dialysis tubing cellulose membrane bag pretreated with 0.5X TB-buffer according to prior instructions. Electrophoresis was run at 80 V for 15 min followed by 80V and 2 min at opposite polarity. The final concentration was roughly 10 nM according to absorption spectroscopy using molar attenuation coefficients of $1 \cdot 10^7$ and $3.67 \cdot 10^8$ for 5 and 15 nm Au-NP solutions respectively.

4.2.5 Au-NP DNA origami coupling

The coupling of Au-NPs onto the 42 hb was attempted via two approaches. Both involve DNA origami material isolated by membrane tubing (300 pM) mixed with isolated Au-NP DNA conjugate (10 nM) in equivolume amounts. The first approach consisted of 10 μl of the final solution being directly deposited on mica followed by 10 min incubation, rinsing with 40 μl water and N_2 blow-drying. The other approach followed an annealing protocol where the solution was cooled from 37 to 20 °C over a 17 h time-period followed by identical deposition and rinsing.

Attempted conjugation of Au-NPs onto the 18 hb proceeded by treating the DNA origami tubing solution (900 pM) with TECP (final concentration 20 mM) for 1 h at room temperature. Afterwards, a 300 pM origami solution was mixed with 10 nM Au-NP solution in equivolume amounts with identical deposition and rinsing.

4.2.6 AFM sample preparation and imaging

All AFM measurements were performed on a Bruker multimode AFM in tapping mode. DNA and Au-NP imaging was performed using either an Asylum Research (Oxford Instruments) silicon-based cantilever with res. freq. of 68 kHz and a force constant of 1.43-2.47 N/m. Or a Team Nanotec HR-SCC cantilever with res. freg. of 225 kHz and a force constant of 3 N/m.

Either 2x2 or 1x1 μm images were recorded with a scan-rate between 0.5 and 1 Hz. Generally, images were done at three different areas on the mica surface for all samples to gain an insight into the consistency.

DNA origami sample preparation for AFM imaging was done by pipetting 10 μL sample onto a freshly cleaved mica surface followed by 10 min incubation, rinsing with 40 μl water followed by N_2 blow-drying. Imaging of scaffold samples were done by pipetting 10 μL of

a 1 nM scaffold solution containing 5 mM $MgCl_2$ followed by identical incubation time and rinsing procedure.

For imaging of Au-NPs, a freshly cleaved mica surface was incubated under vacuum with a 250 μl APTMS + 500 μl toluene solution for 30 min. 10 μl of 100 nM Au-NP solution was pipetted on the surface followed by an incubation time of 30 min, rinsing with water and lastly N_2 blow-drying.

Image analysis was done using Gwyddion software. Height profiles were obtained using the profile extraction tool.

4.2.7 Melting temperatures of scaffold and DNA origami structure

10 μl scaffold and DNA origami samples were prepared according to table. 4.3 with $MgCl_2$ concentrations at 0, 4, 8, 12, 16 and 20 mM. DNA origami structure samples underwent thermal annealing according to program E. Each sample was mixed with iTaq Universal SYBR Green Supermix (Bio-Rad) in a 1:1 ratio. The samples were added to a PCR plate and covered with transparent film before brief centrifugation. The plate was afterwards loaded into a Bio-Rad Real-time system and underwent heating from 20-95° with a 0.5° increase every 5 sec.

4.2.8 Gold-coated glass platform

A gold-coated glass slide meant for total internal reflection fluorescence experiments was made by first cleaning a glass wafer with acetone and isopropanol (Sigma-Aldrich) followed by N_2 blow-drying. A 2 nm Cr and 50 nm Au layer was deposited on the glass by physical vapour deposition using a Cryofox Explorer 600 system. Afterwards, the glass was sputter-coated with photo-resist and baked at 110°C for approximately 70 s. The glass was cut into pieces with the dimensions of 3x4 cm using a Disco Dicer Saw. Afterwards, the photo-resist was removed by submerging the pieces in an acetone solution (Sigma-Aldrich) in an ultra-sound bath and finally rinsing with isopropanol and blow-drying with N_2.

5 | Results

5.1 CanDo simulation

The structural properties of the 18 and 42 hb DNA origami designs were computationally predicted by CanDo to gain insight into the structural properties.

5.1.1 18 helix-bundle structure

The 18 hb structure along with the root mean square fluctuations are seen from different angles in figure. 5.1. Additional images are found in appendix C.1.

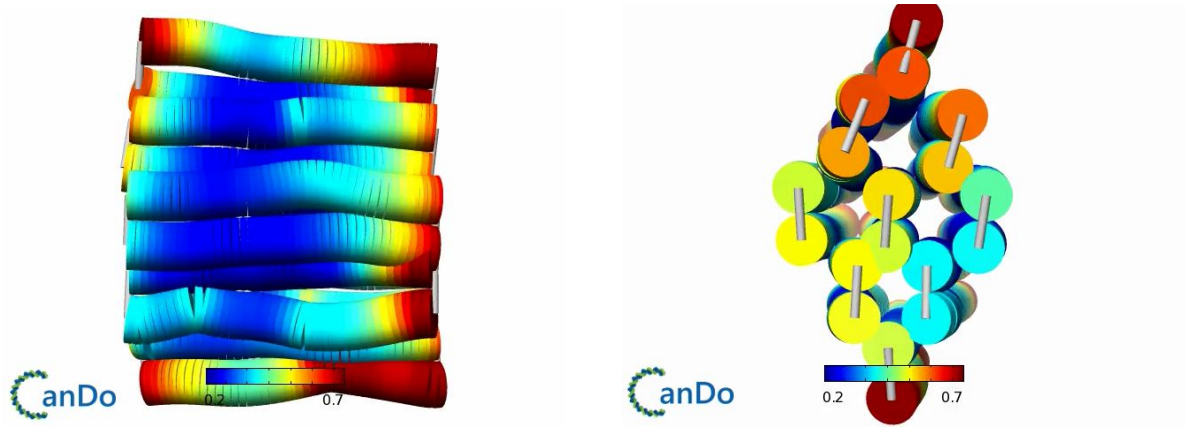

(a) (b)

FIGURE 5.1: *RMSF (nm) of the 18 hb DNA origami structure*

RMSF values of 0.2-0.3 nm are observed in the left center of the majority of helices. The left ends of these helices have slightly higher values of approximately 0.5 nm while the right ends have values of 0.6-0.7 nm. Helix 9 and 16 which are the top and buttom helices seen are characterised by having regions of RMSF values of approximately 0.4 nm in the center left region while the center right and right end regions have values of 0.7 nm.

5.1.2 42 helix-bundle structure

The root mean square fluctuations of the 42 hb are seen in figure. 5.2. Additional images are found in appendix. C.2.

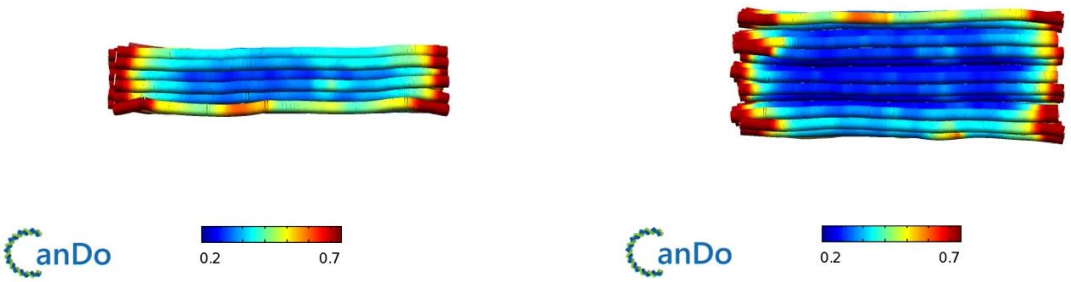

(a) (b)

Figure 5.2: *RMSF (nm) of the 18 hb DNA origami*

Analysing the helices seen in figure. 5.2(a), RMSF values of approximately 0.3 nm are predominantly observed at large regions in the center area with occasional stability spikes of 0.2 nm. The lowest stability areas are seen at the helix ends. Viewing the RMSF profile in figure. 5.2(b), the helices have a lower RMSF of approximately 0.2 nm at nearly all center-areas. Once again, helix ends display low stability.

5.2 Simulations of the optical properties of Au-NPs

5.2.1 Electric field profiles

The electric field response of Au-NPs along with the scattering and absorption cross-sections were computationally predicted using COMSOL.

Complete electric field profiles in and around 80 nm Au-NP monomer and dimers are shown in figure. 5.3 when irradiated by light at 647 nm with an oscillating electric field in the x-direction.

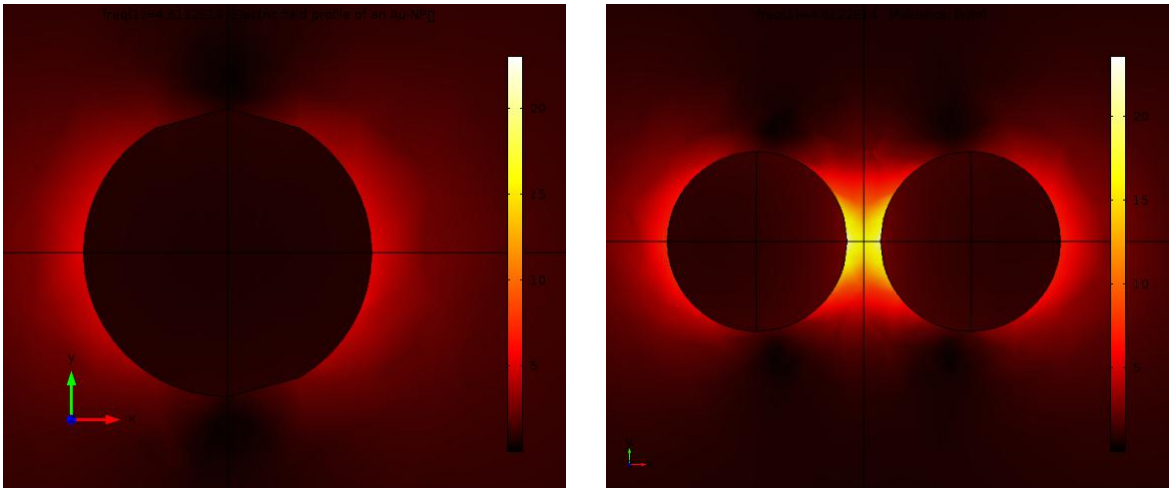

[]

(b)

FIGURE 5.3: *Electric field profiles of Au-NP monomer and dimer systems when irradiated by 647 nm light. The scale-bar in each case is 0-23.*

Most importantly, a clear angle dependence of the electric field is observed in both cases. The electric field strength is at a minimum at the particle surface for x=0, while the maximum is located at y=0 for an Au-NP monomer. The same is true for an Au-NP dimer except for the occurrence of a slight shift of the electric field minimum towards the gap. For the dimer set-up, the field at the particle surface for x=0 is higher in the dimer gap compared to the ends. In addition, the high electric field in the gap is significantly larger than what is produced by an Au-NP monomer of identical size. Furthermore, a clear case of symmetry is observed along x=0 for both set-ups.

The electric field strengths relative to that of incoming light are measured at varying positions relative to the particle surface of both an Au-NP monomer and dimer for different particle sizes along the center. These are shown in figure. 5.4 when light with a wavelength of 647 nm interacts with Au-NPs.

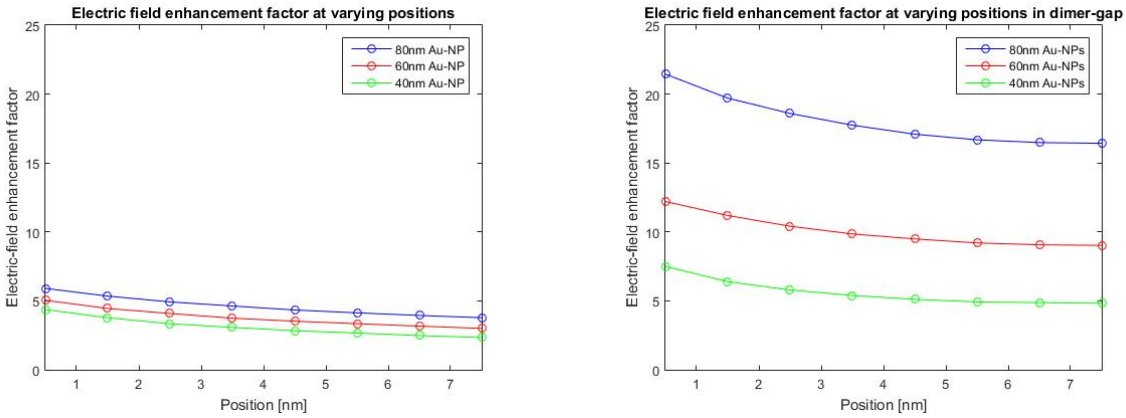

(a) (b)

Figure 5.4: *Relative electric field strength at positions relative to the particle surfaces.*

Most noteworthy is the significant electric field amplification that is seen in the vicinity of the nano-particle surface relative to that of the incoming light. Electric field amplifications near the surfaces are approximately in the range of 4.5-5.5 and 7.5-22 for Au-NP monomers and dimers respectively. Moving away from the surface results in the decrease of electric field intensity with enhancement factors of approximately 2-4 and 5-16.

5.2.2 Full spectrum electric field enhancements

Figure. 5.5 shows the electric field enhancements in the center of the gap for wavelengths between 400 and 800 nm for Au-NP dimers of different sizes as well as gap distances.

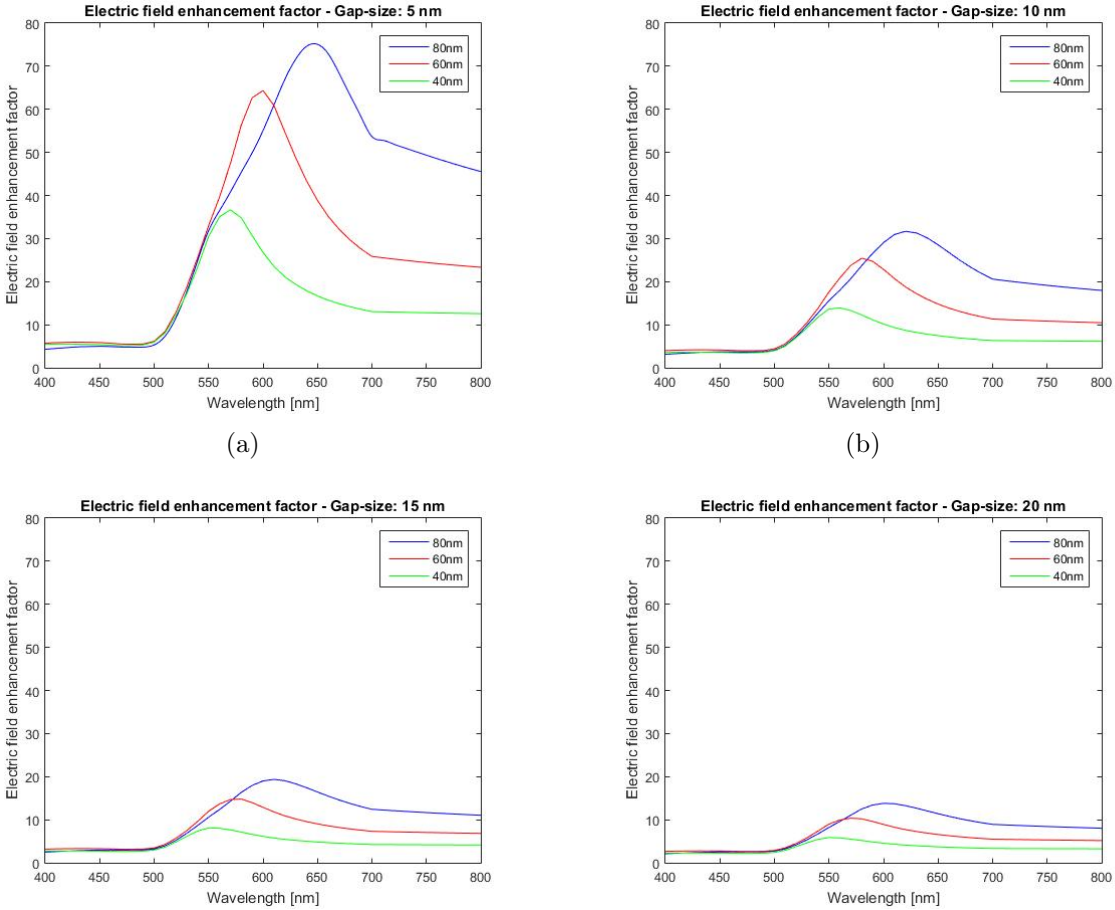

FIGURE 5.5: *Electric field enhancement in the center of the gap of Au-NP dimers*

All graphs generally have the same shape, the major difference being the location of the maxima and the accompanied electric field enhancement factor resulting in varying degrees of sharpness of the graphs. A consistent trait is that for each respective gap-size, increasing the nano-particle size results in a red-shift of the maxima in addition to an increase in the electric field enhancement factor. Widening the gap-size results in the peak values for each respective nano-particle size being blue-shifted.

5.2.3 Scattering and absorption cross-sections of Au-NPs

The ratio of the scattering to absorption cross-sections of Au-NP monomers and dimers for particle sizes of 40, 60 and 80 nm are seen in figure. 5.6. These values are found in order to initially determine at which wavelengths the excitation and emission spectra of a fluorophore should be located in order to maximise fluorescence.

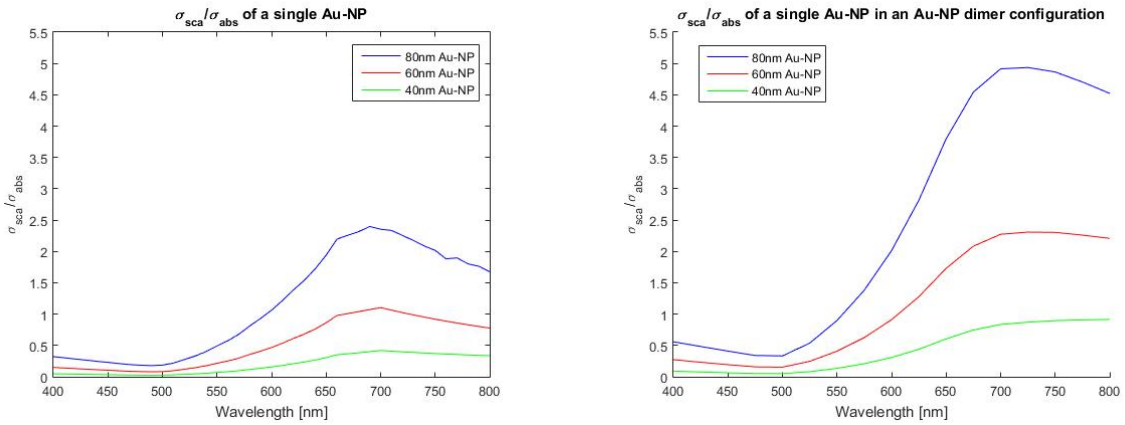

(a) (b)

Figure 5.6: $\frac{\sigma_{sca}}{\sigma_{abs}}$ *of a single Au-NP in continuous medium and in a dimer set-up. The dimers are separated by a distance of 15 nm.*

Observing at 400 nm for a single Au-NP, all corresponding values lie below 0.5. As the wavelength red-shifts towards 500 nm, a global minimum is seen for all particles sizes. Increasing the wavelength leads to an increase in the ratio which reaches unity at approximately 600 nm for 80 nm particles, 670 nm for 60 nm particles while for 40 nm particles unity is not reached at this interval of wavelengths. The ratio continues an increase reaching the maximum at approximately 700 nm for all particles investigated The increase and decrease of the ratio value is more rapid as the particles increase in size. Generally, as the particle size increases so does all values at all corresponding wavelengths.

In the case of a single Au-NP in a dimer set-up, many of the same tendencies are observed as with single Au-NPs. The minima and maxima are located at approximately the same wavelengths. An exception is that no clear maximum is observed for a 20 nm particle, instead a continuous increase from its minima at 500 nm is observed. Importantly, all minima and maxima are more pronounced compared to those found for identical particles sizes in an Au-NP monomer set-up.

5.3 Fluorescence enhancement simulations

The quantum efficiency of a dipole emitting light between 400-800 nm in dimer-gaps of different sizes is found in order to better understand the enhancement and dimer-separation relationship. Afterwards, in depth analysis is done on the decay rates of a dipole with properties identical to an ATTO-647N in a 15 nm Au-NP dimer-gap in addition to a monomer set-up with a dipole/Au-NP distance of 7.5 nm. Lastly, analysis is done on a dipole with an emission wavelength of 665 nm in 15 and 20 nm dimer-gaps to quantitatively predict the enhancement factor of the ATTO-647N dye in geometries similar to the ones of the origami structures in this study.

5.3.1 Quantum efficiency predictions

Full spectrum quantum efficiency of a dipole in an Au-NP gap of various sizes

Figure. 5.7 and 5.8 show the quantum efficiency of an ideal dipole emitting light between 400 and 800 nm while located in Au-NP gaps of different sizes. The figures contain information on a dipole located in a perpendicular and parallel orientation respectively.

In the case of a perpendicularly oriented dipole, it is seen for all spectra that the maxima resides at approximately 650-700 nm while the minima is located at 500-550 nm. The quantum yield is also seen to increase for larger particles. In addition, as the gap-size is increased so are the quantum efficiency values.

For a parallelly oriented dipole, the maxima are located at approximately the same wavelengths with the spectra for particle size 40 nm with a gap-size 15 and 20 nm being the exceptions. The clearest trend is seen in the form of a clear decrease in quantum efficiency values at all wavelengths as the gap-size is decreased. All QE values are also seen to be significantly smaller than the ones obtained for a perpendicularly oriented dipole for identical particle-sizes and gap-distances.

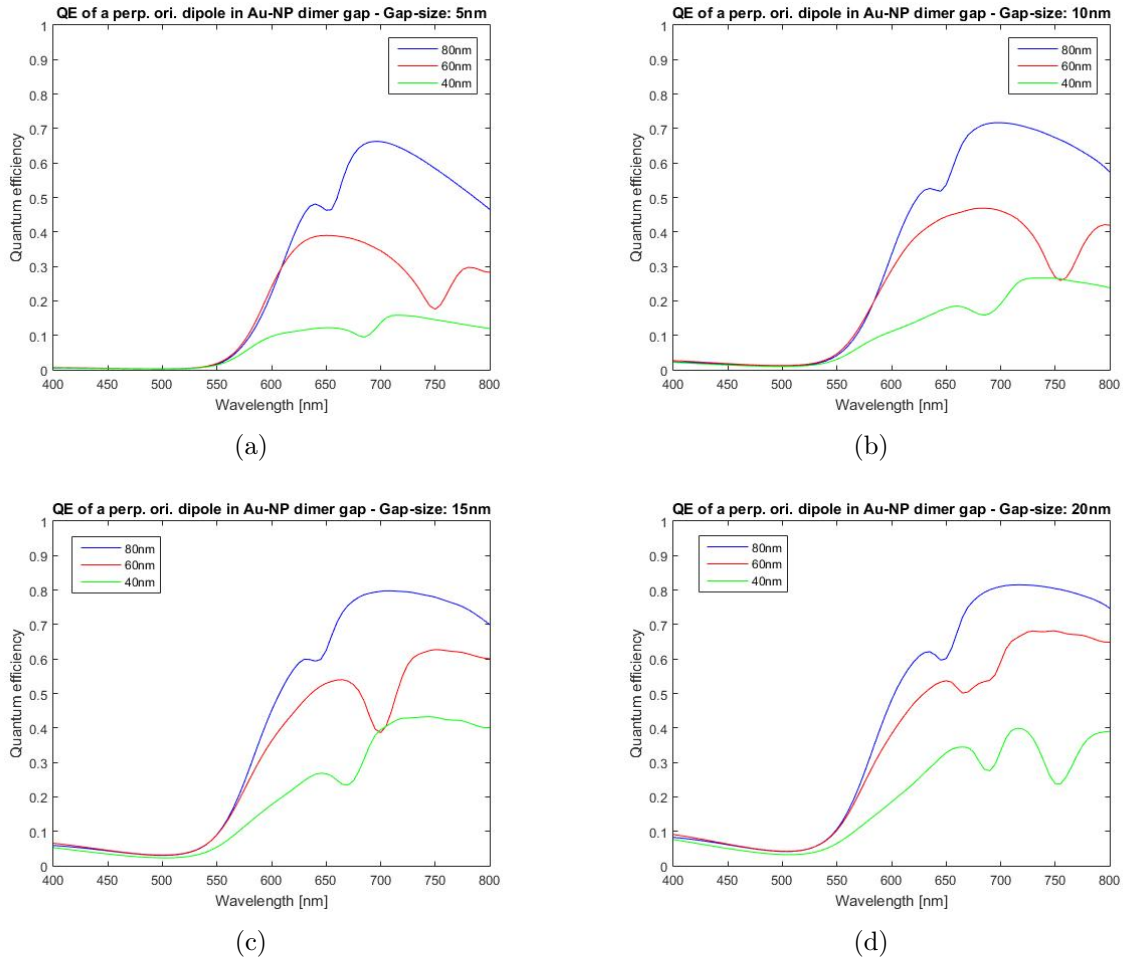

Figure 5.7: *Quantum efficiency of an ideal dipole emitting light at wavelengths between 400-800 nm in an Au-NP dimer-gap with sizes between 5 and 20 nm. The dipole has a perpendicular orientation with respect to the nano-particle surface.*

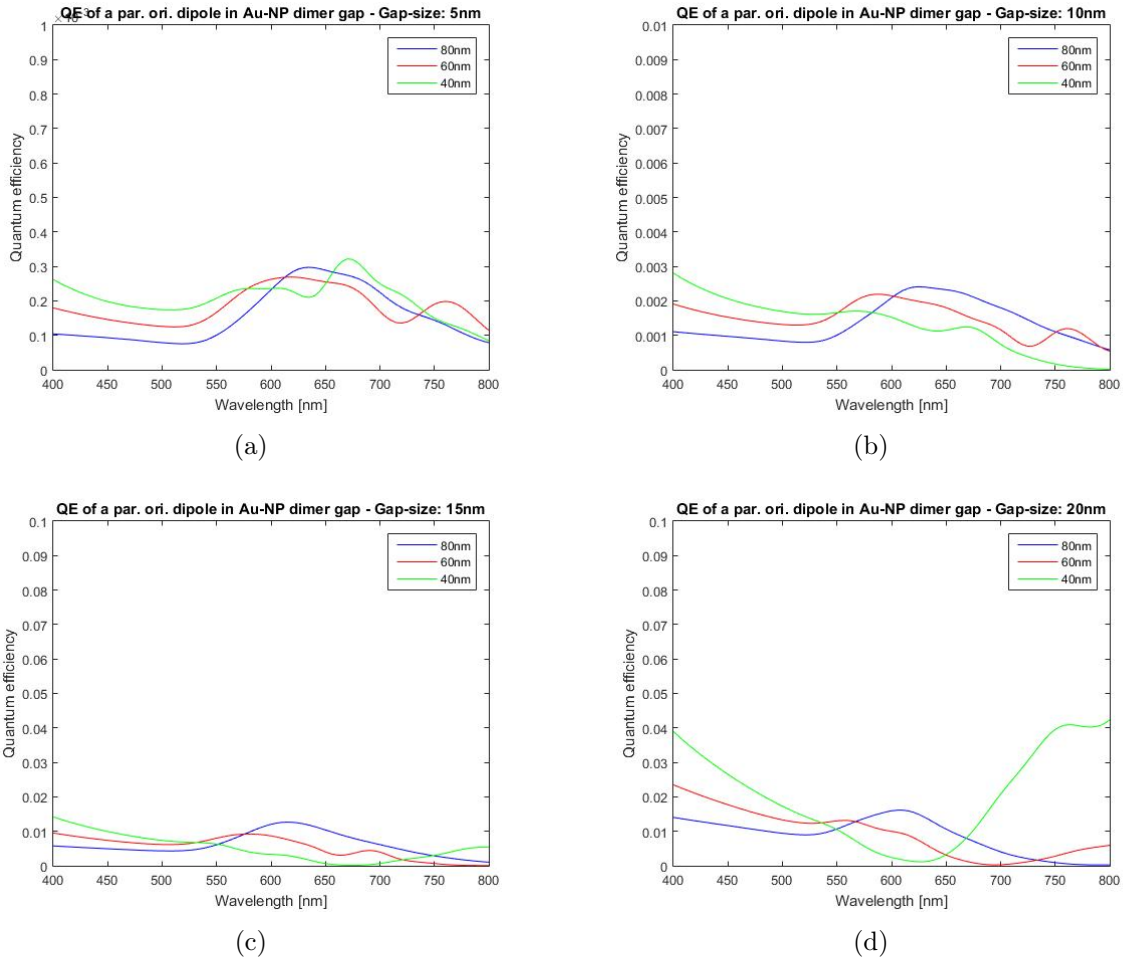

FIGURE 5.8: *Quantum efficiency of an ideal dipole emitting light at wavelengths between 400-800 nm in an Au-NP dimer-gap with sizes between 5 and 20 nm. The dipole has a parallel orientation with respect to the nano-particle surface.*

Radiative and non-radiative decay rates

The normalized radiative and non-radiative decay rates of a dipole emitting light at 665 nm identically to the Atto-647N dye in the presence of varying sizes of single Au-NPs and Au-NPs dimers are examined in figure. 5.9. The dipole was located 7.5 nm away from Au-NPs.

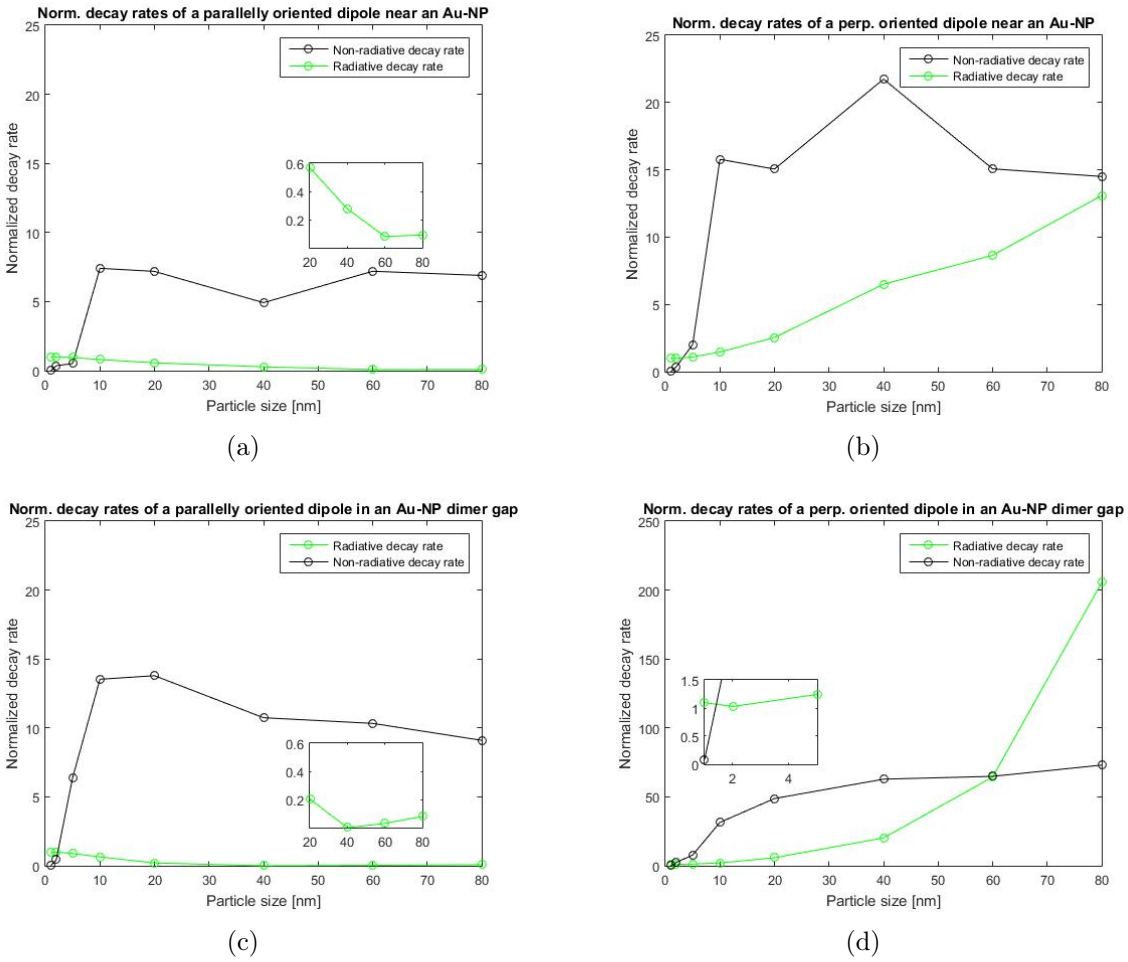

Figure 5.9: *Normalized radiative and non-radiative decay rates for a dipole in both a parallel and perpendicular orientation with respect to the nano-particle surface.*

Comparing the radiative and non radiative decay rates for both orientations and Au-NP set-ups reveal several interesting tendencies. The non-radiative decay rates have similar tendencies across all four sub-figures. The decay-rate is found to increase from 1-10 nm particles where-after the values become approximately constant.

In both set-ups the radiative decay rate for a perpendicularly oriented dipole is found to increase with larger particles whereas the opposite is seen for a parallelly oriented dipole. Comparing the radiative decay-rate in a monomer and dimer set-up reveals that the values are higher in a dimer set-up for a perpendicular oriented dipole. For a parallelly oriented dipole, values are seen to be smaller in an dimer set-up especially for larger sized particles.

An important property is that at small particle sizes, the radiative decay rate is approximately unity while the non-radiative decay rate is approximately zero.

Using the data presented in figure. 5.9 along with eq. 1.23, values for the corresponding quantum yields which are necessary in order to quantitatively calculate the fluorescence enhancement factor can be found. Figure. 5.10 presents the results for both set-ups and orientations along with an average that is weighed according to eq. 3.2.

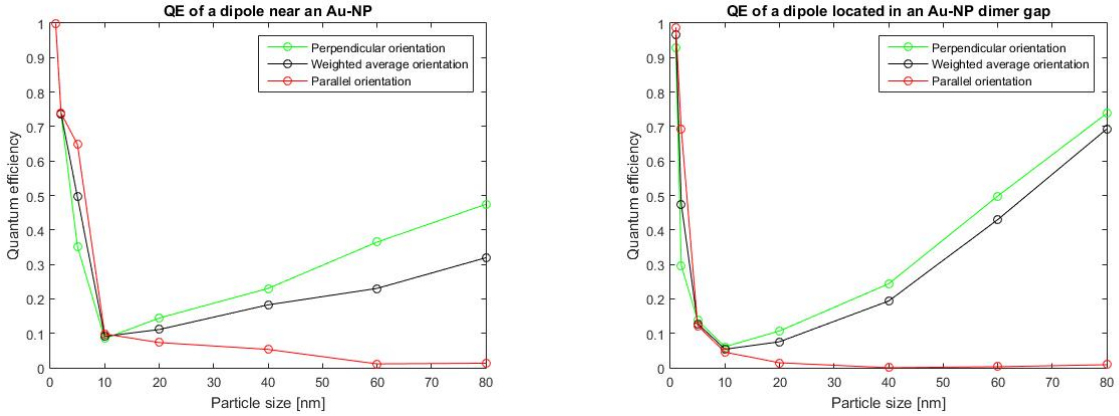

(a) (b)

FIGURE 5.10: *Quantum efficiency of an ideal dipole in perpendicular and parallel orientations in the presence of either an Au-NP monomer or dimer with sizes ranging between 1 and 80 nm*

In the case of a dipole near a single Au-NP, a particle size of 1 nm results in quantum efficiencies of approximately unity. As the particle size increases the quantum yield drops for both orientations until a size of approximately 10 nm is reached. Hereafter, the parallel orientation continues a decline which reaches roughly 0.01 at 80 nm particles while the perpendicular orientation begins to show a linear increase which ends at 0.49. Averaging both orientations shows an approximately linear decline in quantum efficiency between 2 and 10 nm size particles. Hereafter, a linear increase is seen

For a dipole residing in a dimer gap, the QE is located at approximately 0.9 for both orientations for a particle size of 1 nm. As the particle size increases the QE is found to decrease for both orientations. At 10 nm the declining trend for a perpendicular dipole is broken and a significant increase is seen in line with figure. 5.10(a). The decrease is continued for a parallel dipole with values significantly smaller than the ones found in the monomer set-up.

Additional QE and decay-rate data for Au-NP set-ups with varying particle sizes and gap-distances can be seen in figure. D.3 in appendix. D.

Power-output profiles of a dipole near Au-NPs

To graphically exemplify the apparent difference in quantum yield for different dipole orientations, the time-average power output behaviour of a dipole in both a parallel and perpendicular orientations were studied near an Au-NP monomer using COMSOL. The dipole emits light at 665 nm with a separation distance of 50 and 100 nm from a 60 nm large Au-NP.

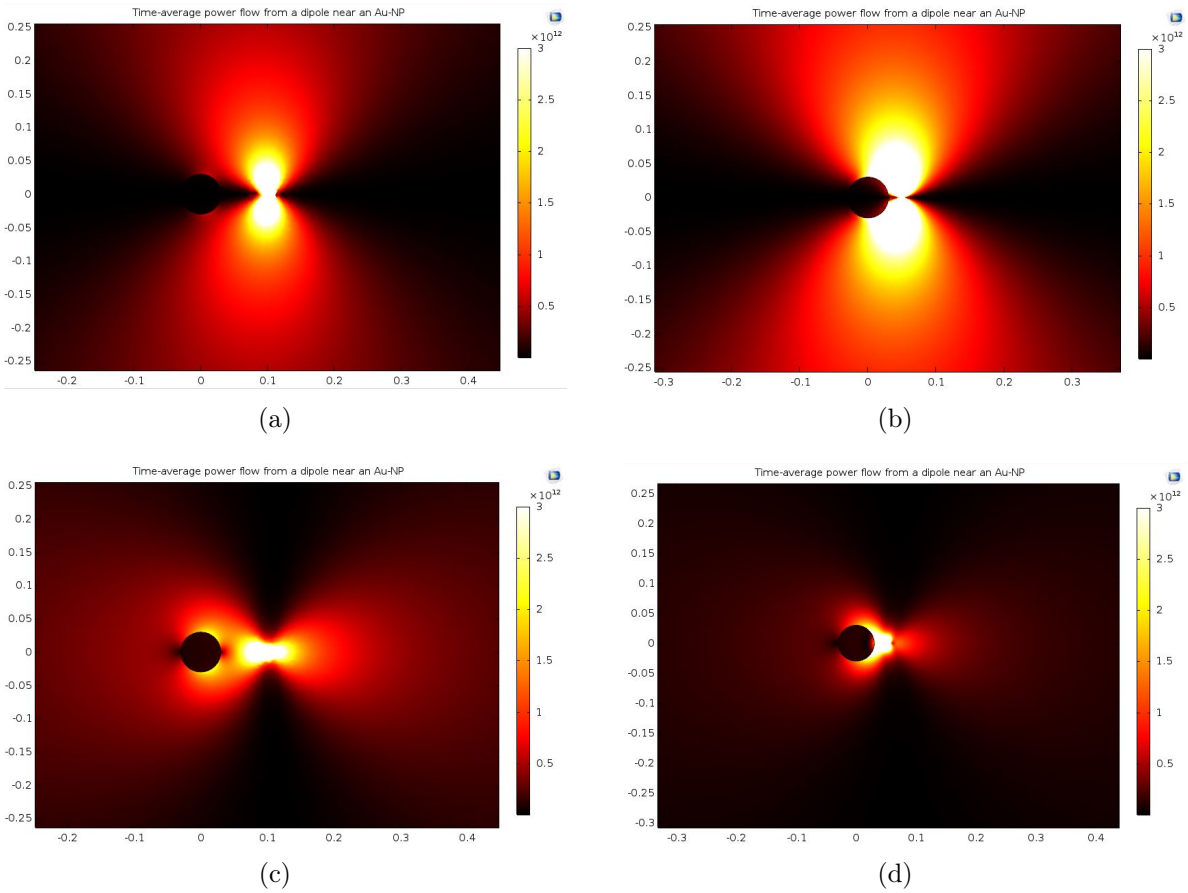

Figure 5.11: *Time-average power from a dipole emitting light at 665 nm positioned at 50 nm and 100 nm away from the center of a 60 nm Au-NP monomer*

The most interesting effects are observed when comparing the evolution of the power output when varying the dipole positions. Moving a perpendicularly oriented dipole closer to the surface results in a significant enlargement of the power output. The exact opposite is seen for a parallelly oriented dipole. Here a noticeably damping of the surrounding power profile is seen.

Monomer and dimer comparison

Combining the measurements used for predicting the quantum yield in figure. 5.10 along with eq. 1.23, the expected quantum yield of an ideal dipole as well as the ATTO-647N dye can be calculated. The average enhancement is seen in figure. 5.12 for particles with diameters spanning between 2 and 80 nm. The electric field strength data used for these calculations can be viewed in figure. D.1 in appendix. D.

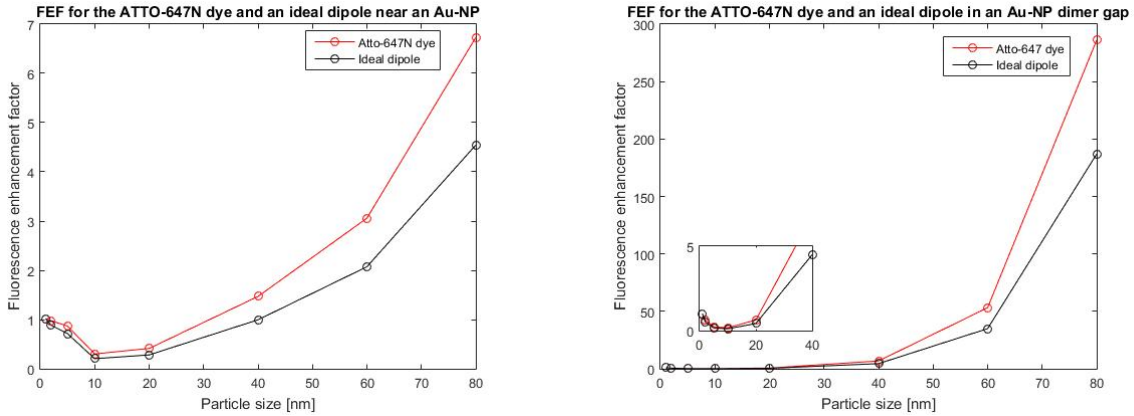

(a) (b)

FIGURE 5.12: *Fluorescence enhancement factor of a dipole located at a distance of 7.5 nm of a single Au-NP and in an Au-NP dimer-gap of 15 nm*

The enhancement can be seen to be highly dependent on the Au-NP particle size in addition to the basic set-up. In each case, the fluorescence is nearly independent of the presence of Au-NPs if the particle size is very small. As the particle-size increases, the fluorescence enhancement is seen to decrease below unity until a particle size of 20 nm is reached. At points hereafter, enhancements are increased significantly with increasing size.

Fluorescence enhancement of dipole in 15 and 20 nm dimer gap

Figure. 5.13 compares the predicted fluorescence enhancement of the ATTO-647N dye in a dimer-gap of 15 and 20 nm. These dimensions are close to the ones expected from dimer set-ups using the origami structures in this study. All necessary decay-rate data and electric field strengths are found in appendix. D.

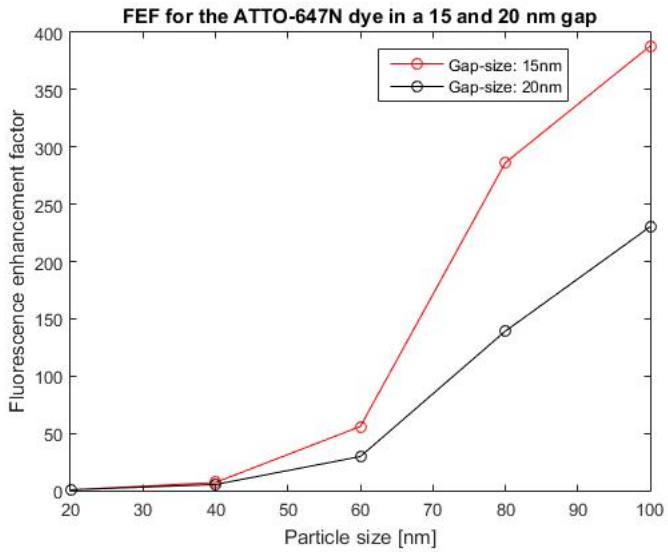

Figure 5.13: *Comparison of the fluorescence of the ATTO-647N dye in a 15 and 20 nm dimer-gap*

The most important property is that fluorescence is expected to be the highest for a 15 nm set-up almost by a factor of two. The enhancement factor is found to be highly dependent on the particle size resulting in an increase for larger particles.

Using the simulation environments adapted in this study, the case of 80 nm dimers separated by a distance of 23 nm as investigated by Acuna et. al. [57] can be calculated and the findings compared. The dimensions are almost exactly the same as the ones you can expect for an Au-NP dimer set-up for the 42 hb. Acuna et. al. found that a perpendicular oriented dye in the gap would experience a fluorescence enhancement of approximately 115 times when irradiated by light at 640 nm.

In this study, Lumerical gave a quantum yield of 0.82 and COMSOL gave an electric field factor of 12.2 times yielding a fluorescence enhancement factor of 122. This is roughly a 6 % increase compared to the findings of Acuna.

The QE and fluorescence enhancement factor of an ideal dipole was also examined at different positions in a 15 nm dimer-gap. Highest enhancement is found in the center of the gap. All results are seen in appendix. E

5.4 DNA origami analysis gels

Gel-electrophoresis was done on both 18 and 42 helix bundles to gain initial insight into the folding quality as well as finding optimal conditions for proper folding.

5.4.1 18 helix-bundle structure

To study the effect of using different annealing programs as well as $MgCl_2$ concentrations on the folding of the 18 hb DNA origami structure, a $MgCl_2$ screen was performed along with five different annealing programs. Figure. 5.14 shows gels of samples having undergone folding programs A, B and C.

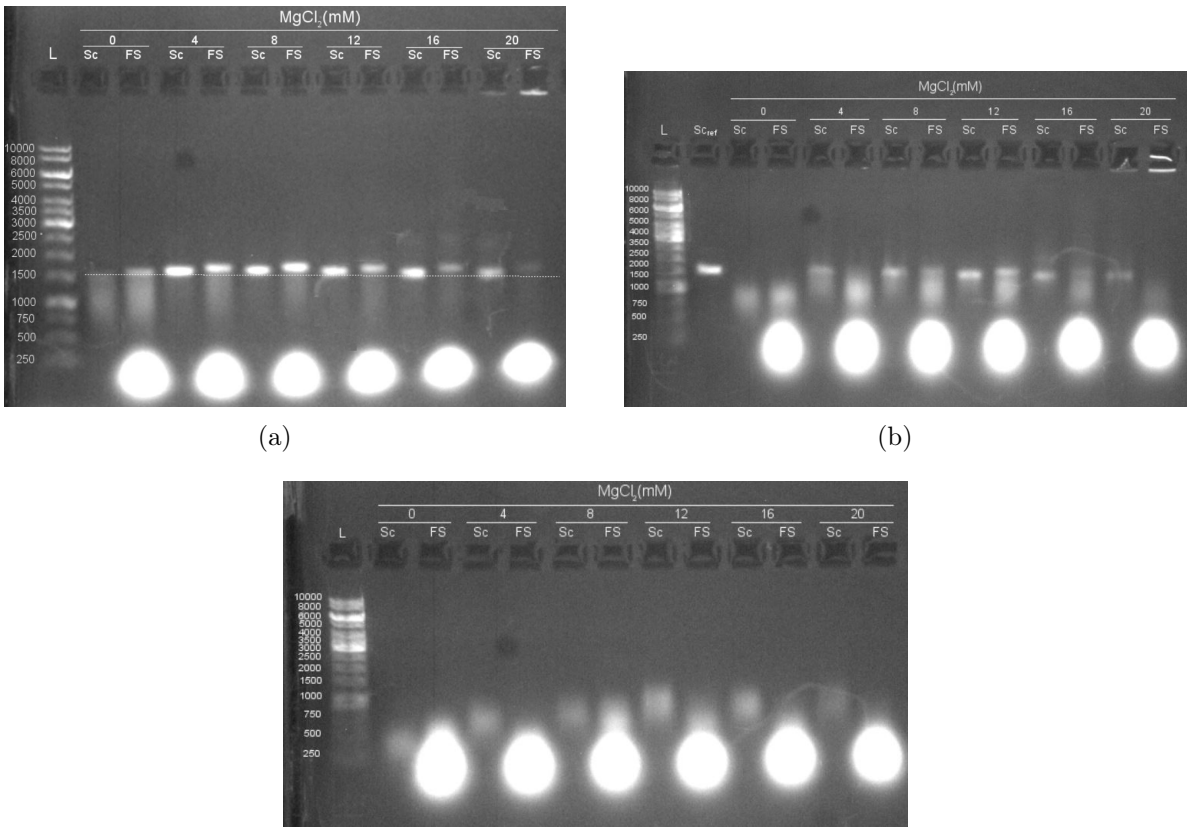

(a) (b)

(c)

FIGURE 5.14: *Gels containing samples undergone folding according to folding programs A, B and C at different $MgCl_2$ concentrations. Scaffold samples undergone the respective folding programs were added as references*

In figure. 5.14(a), it is noticeable that all mains bands appear at approximately 1600 bp. The scaffold solutions at 4, 8, 12 and 16 mM $MgCl_2$ appear to have the same intensity as well as migration rate. The bands for the scaffold solution at 0 and 20 mM appear to have lower intensity. For 0 mM no clear band is seen, instead a smear is observed located between 750 bp and 1500 bp.

Figures 5.14(b) and 5.14(c) show images of gels with samples that have undergone annealing according to programs B and C respectively. Both images were taken after 2h. In

the gel for program B, smearing appears to be significant for several scaffold samples and especially folding samples, although some-what well-defined bands are seen at approximately 1500 bp. For figure. 5.14(c) all samples have noticeable smearing with no clear well defined bands being present.

Gel analysis of samples that have undergone annealing program D is seen in figure. 5.15.

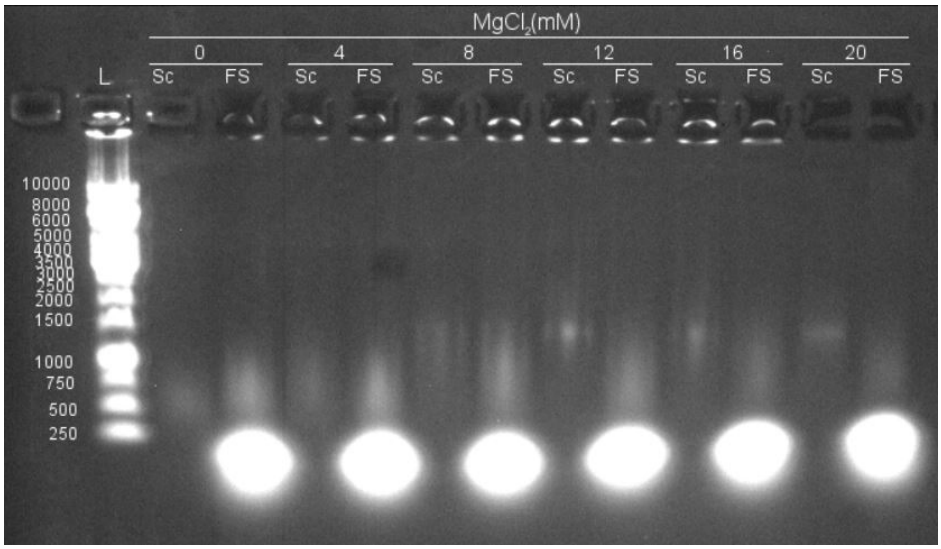

Figure 5.15: *Gel containing samples that have been treated according to annealing program D.*

Here it is seen that smearing is a recurrent phenomenon. Smearing is observed for all samples along with no well-defined bands. In this case, smearing is located between 250-500 bp for Sc(0) while for the other samples it is located between approximately 750-1000 bp.

Program E was the final program inspected with the gel sample seen in figure. 5.16

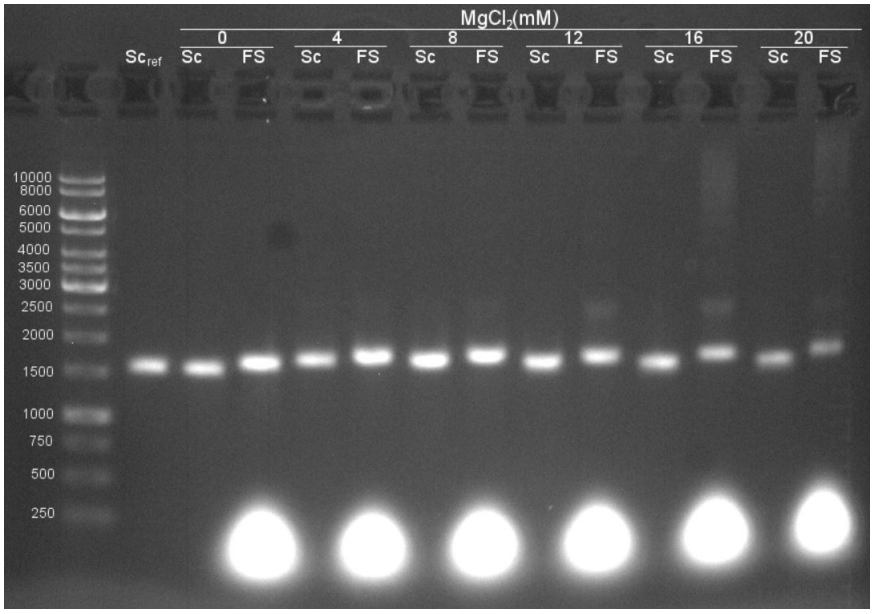

FIGURE 5.16: *Gel containing samples that have been treated according to annealing program E.*

All bands are well defined and have no noticeable smearing near the main bands located at approximately 1500 bp. Interestingly, for samples FS(12), FS(16) and FS(20) there are very faint bands present all located at 2500bp. Faint traces of smearing is located in lanes FS(16) and FS(20) stretching from near the gel wells to approximately 5000bp.

5.4.2 42 helix-bundle structure

The 42 hb structure has previously been analysed thoroughly in literature [11, 35]. The main attention was thereby focused on replicating already found results. Gels containing samples prepared by Tilibits recommendation in addition to a constant temperature approach were investigated.

Constant temperature analysis

Figure. 5.18 shows a gel containing samples that were run at constant temperature over 2 hours.

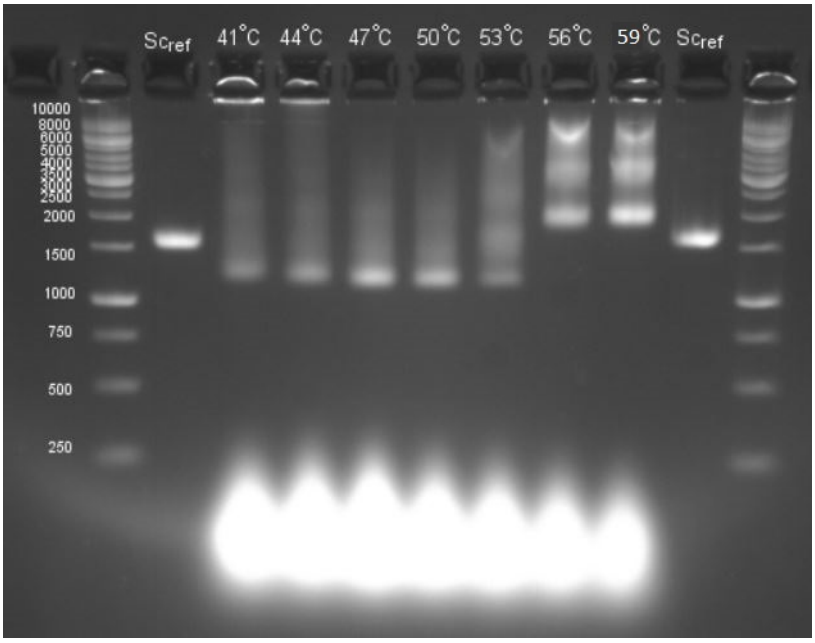

Figure 5.17: *Gel results of the 42 hb DNA origami folded at constant temperatures between 41 and 59 °C*

Samples run between 41 and 53 °C are found to be largely very comparable. Each lane contains a rather pronounced band between 1000 and 1500 bp especially for samples at 47 and 50 °C. It can also be seen that this main band migrates faster through the gel compared to the reference scaffold. Additionally, smearing is seen for each lane in the area of approximately 1500-10000 bp. The samples prepared at 56 and 59 °C are found to have drastically different gel migration characteristics. In these cases, the main bands migrate slower than both the scaffold reference in addition to the main bands of the first five samples. A combination of smearing and a smaller band at approximately 4000 bp is seen as well.

Constant temperature and folding program comparison

A gel comparison of a sample prepared at 50 °C for 2 h and a sample prepared according to Tilibits recommendation (section. 4.2.2) was done to compare the quality of folding in addition to the final yield.

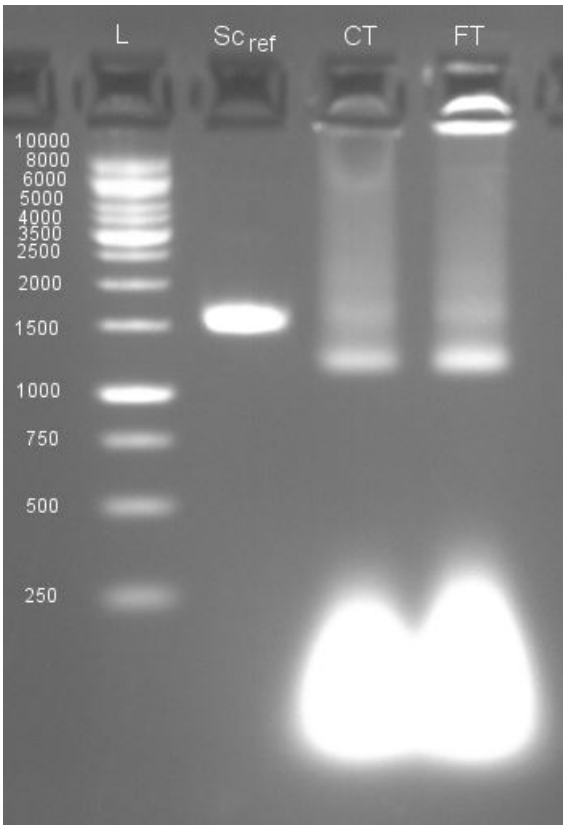

FIGURE 5.18: *Comparison of samples prepared at contant temperature (CT) and according to Tilibit recommendations (FT).*

Both wells have bands located at approximately 1200 bp with the main band in well TF appearing to be brighter. Material trailing appears in both lanes between 1500 and 4000 bp with subtle differences in trailing length and brightness.

5.5 Melting analysis of the p7249 scaffold and 18 helix-bundle structure

Melting temperatures of the scaffold and the 18 hb DNA origami structure were investigated to gain further insight into the biophysical properties of both structures. Figure. 5.19 shows the first derivative of the melting temperature of both the scaffold and 18 hb DNA origami structure for samples that were prepared with various concentrations of $MgCl_2$.

Common for all scaffold samples is the occurrence of significant melting between 20-50°C with a maximum residing at approximately 50°C in all cases. Additionally, it can be seen that for all samples, the majority of melting has occurred by 70-80°C. For DNA origami samples the melting primarily occurs at 20-60 °C with a maximum at 60°C. The exception is the occurrence of a negative derivative value at 60 °C for the origami sample annealed at 0 mM $MgCl_2$. Besides the apparent shift of the melting maxima, the entire melting profile of the origami sample is found to be shifted towards higher temperatures relative to pure scaffold. Lastly, a peak is observed at approximately 80°C for the majority of measurements. This peak is found to decrease as the $MgCl_2$ concentration is increased.

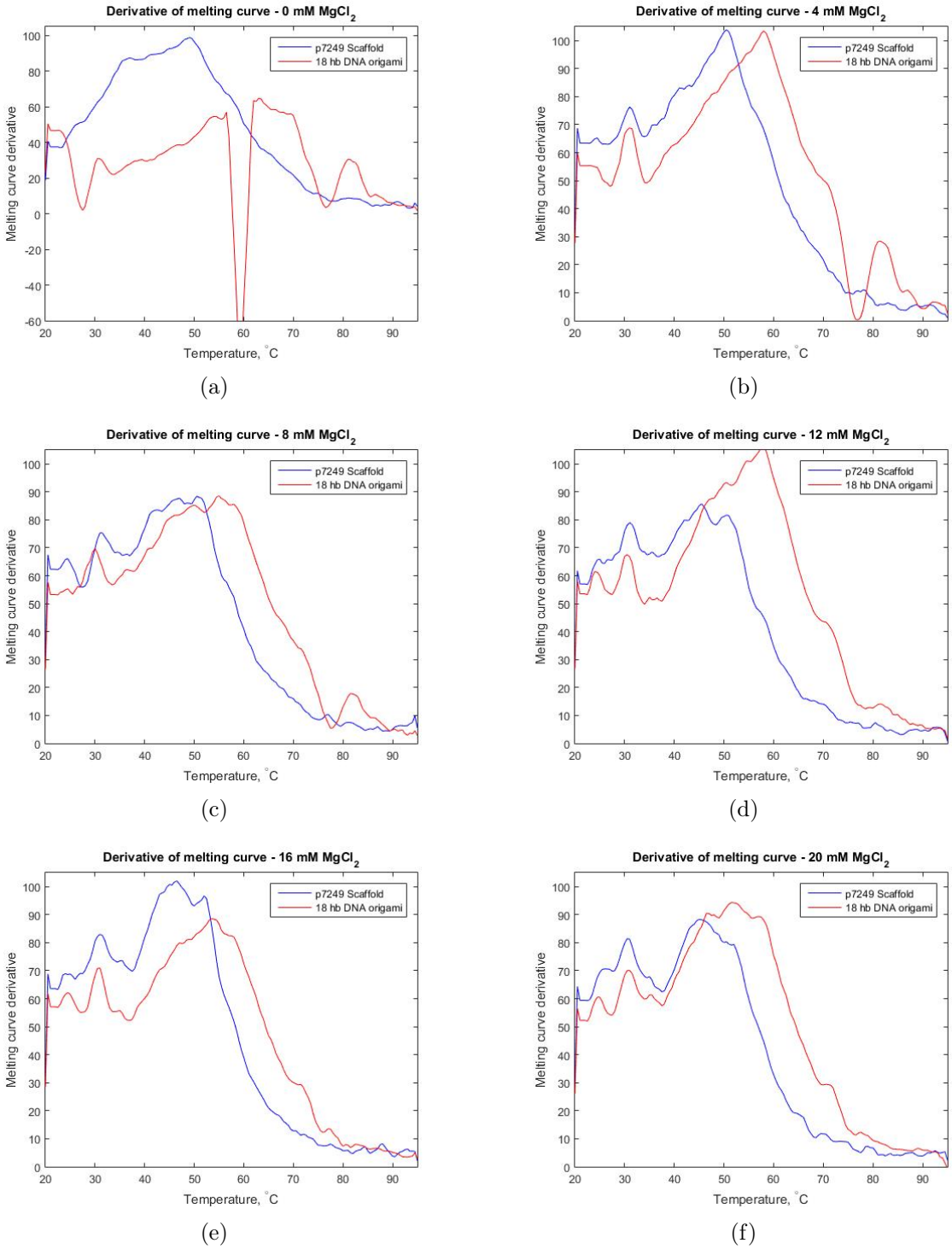

FIGURE 5.19: *Melting curve analysis of the p7249 scaffold and 18 hb DNA origami at different $MgCl_2$ concentrations.*

5.6 Absorption and gel analysis of Au-NPs

5.6.1 Absorption spectra of synthesized Au-NPs

Figure. 5.20 shows a comparison of the normalized absorbance for synthesized 5 and 15 nm Au-NPs.

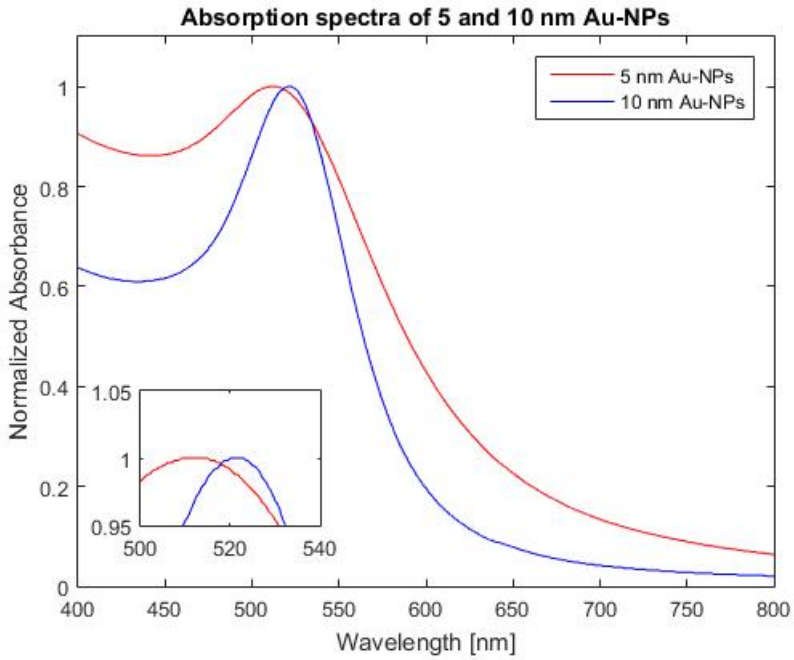

Figure 5.20: *Normalized absorption spectra of Au-NPs synthesized according to recipes for 5 and 15 nm sized Au-NPs.*

Most importantly, the maxima are 512 and 522.5 nm for 5 and 15 nm Au-NP solutions respectively. Secondly, there are differences in the overall trend of each spectrum. The spectrum of 15 nm Au-NPs is found to have a width that is significantly narrower in addition to a sharper peak when comparing to the spectrum for 5 nm particles.

Growth of Au-NPs

The growth of Au-NPs synthesized according to a recipe for 5 nm particles was monitored by absorption spectroscopy at time-intervals after the addition of sodium borohydride. Full spectrum graphs in addition to the wavelength of maximum absorption for each measurement is seen in figure. 5.21.

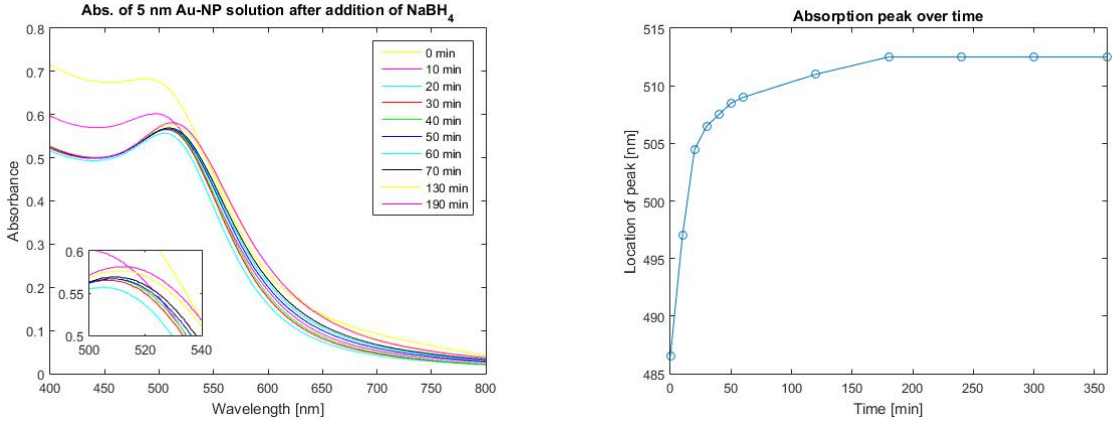

(a) (b)

FIGURE 5.21: *Study into the growth of Au-NPs using absorption spectroscopy*

After the addition of sodium borohydride, the solution immediately turned red. Absorption spectroscopy revealed a peak at 486 nm that continuously was red-shifted over time followed by a decrease in absorbance until 20 min had passed. The red-shift continued but the absorbance increased and became steady after 60 min.

5.6.2 Gel analysis of Au-NP/DNA conjugates

Gel analysis of pure Au-NPs and Au-NP/DNA conjugate solutions were run on an agarose gel to confirm if Au-NP/DNA conjugates had formed. Figure. 5.22 shows a comparison where 5 nm Au-NPs were used.

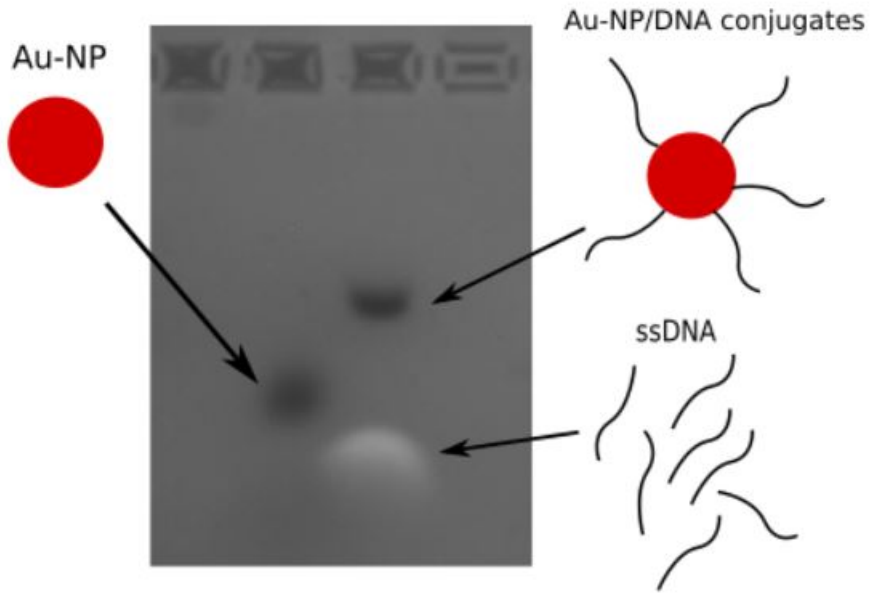

Figure 5.22: *Agarose gel analysis and separation of Au-NP/DNA conjugates.*

Both Au-NP and Au-NP/DNA conjugates are seen as black bands under UV illumination. In normal light, both bands had a deep red colour. The clearest difference between the bands are seen in the migration rate. The Au-NP/DNA conjugation samples had a significantly slower migration rate relative to a pure nano-particle sample. The white smear seen in the Au-NP/DNA conjugate lane is excess single-stranded DNA. Same tendencies were also observed for solutions based on 15 nm Au-NPs.

5.7 AFM studies

5.7.1 Scaffold and DNA origami analysis

p7249 scaffold and 18 helix-bundle imaging

AFM images of the p7249 scaffold strand and an 18 hb origami sample prepared according to program E are seen in figure. 5.23.

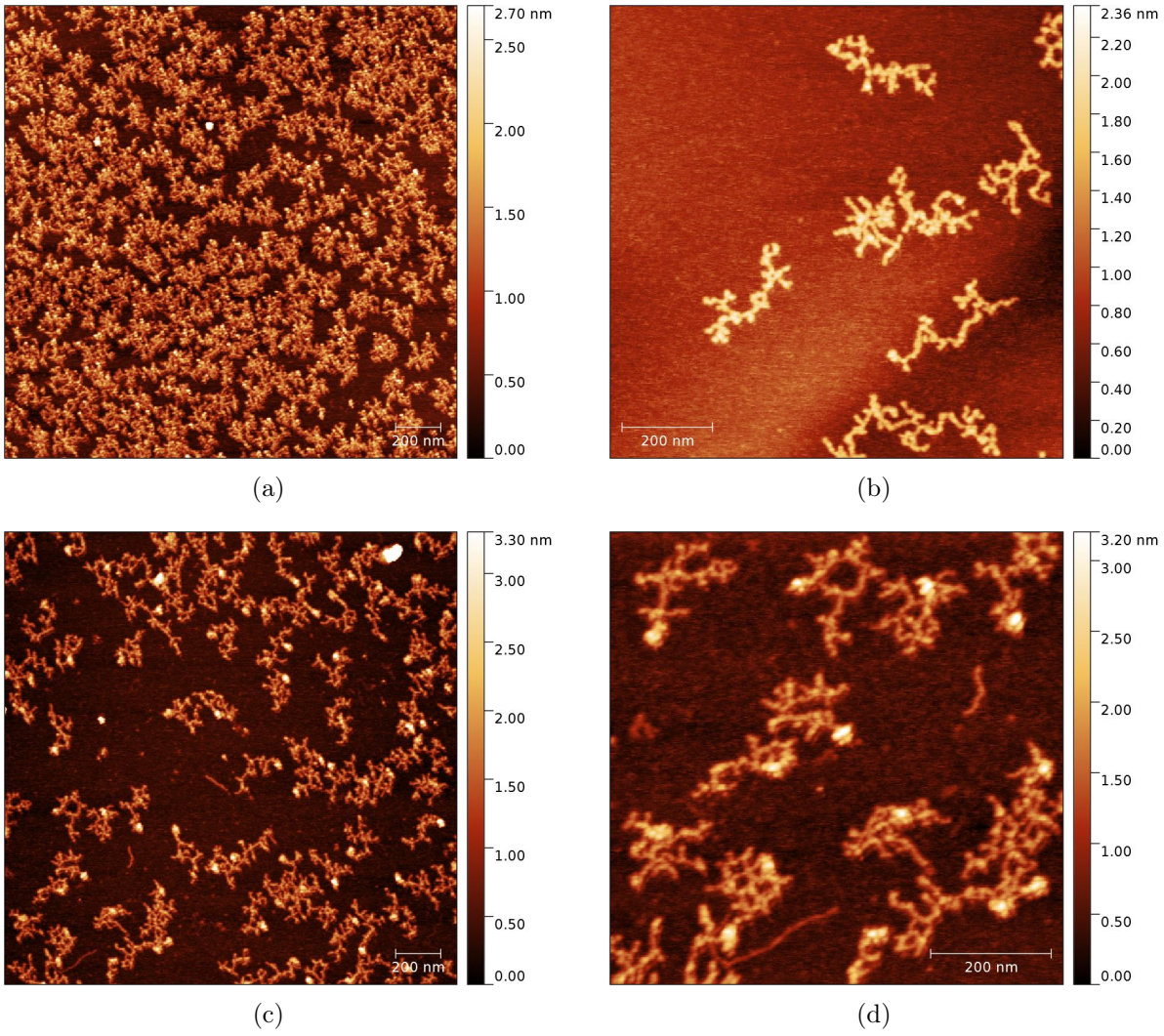

FIGURE 5.23: *AFM images of the p7249 and 18 hb origami sample. Figures. 5.23(a) and 5.23(b) are 2x2 and 1x1 μm scans of the scaffold while 5.23(c) and 5.23(d) are scans of the 18 hb sample.*

Figures. 5.23(a) and 5.23(b) show clear images of the p7249 scaffold having a semi-ordered compact structure with a height of ≈ 0.8 nm. Each scaffold occupies an area of ≈ 200x200 μm. In figures. 5.23(c) and 5.23(d), it is seen that the 18 hb origami sample has high resemblance with the p7249 scaffold. The exception being the occurrence of small patches of DNA measuring approximately 30x24x2.7 nm. Thereby the height is significantly larger than

ordinary scaffold DNA. Additionally, it appears that only one patch exists per individual scaffold strand.

p7560 scaffold and 42 helix-bundle imaging

AFM images of the p7560 scaffold can be seen in figures 5.24(a) and 5.24(b). Figures 5.24(c) and 5.24(d) are images of the 42 hb prepared at a temperature of 50°C for 2 h as well as according to Tilibit recommendations respectively.

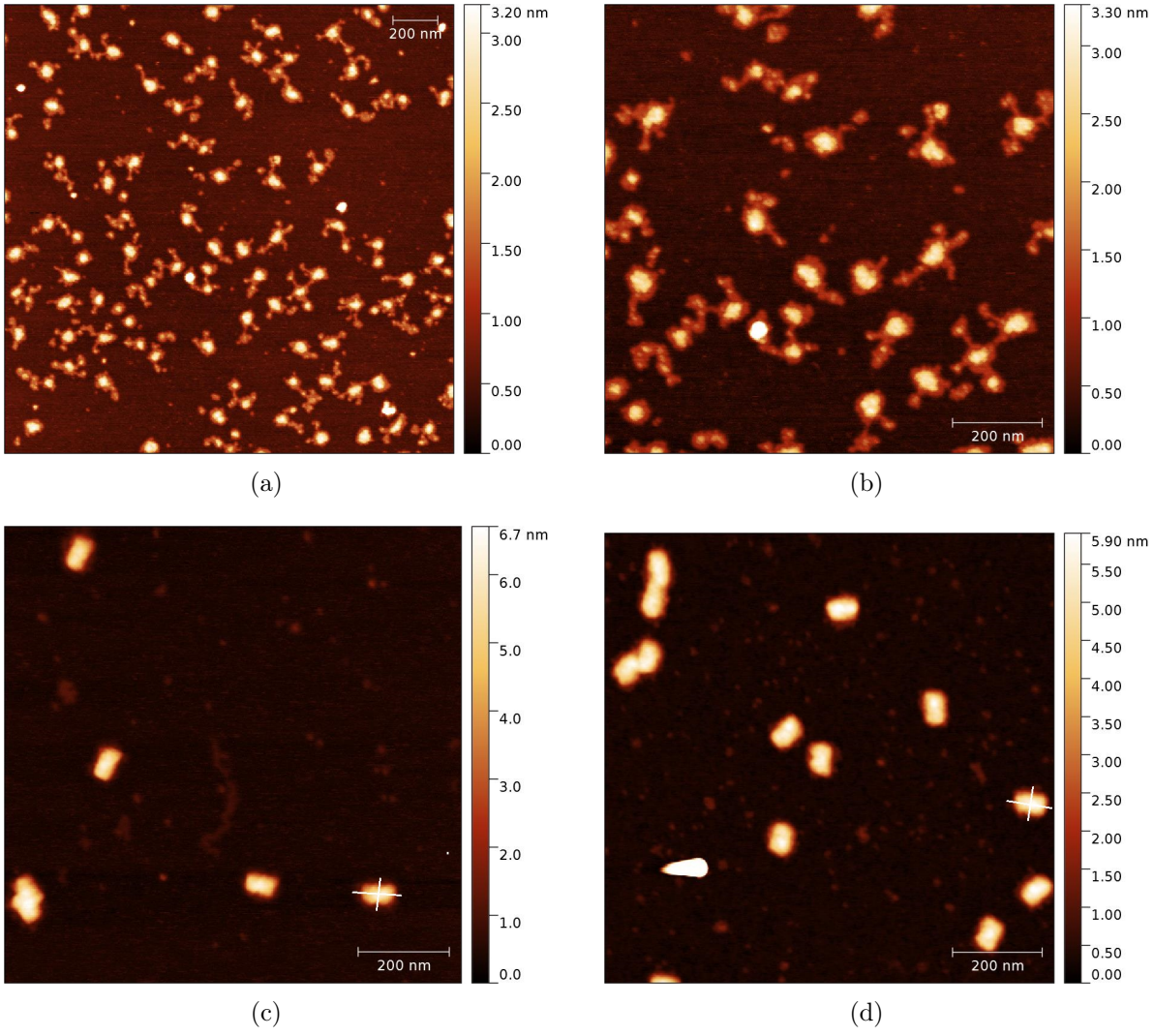

Figure 5.24: *AFM images of the p7560 and 42 hb origami sample. Figures. 5.24(a) and 5.24(b) are 2x2 and 1x1 µm scans of the scaffold while 5.24(c) and 5.24(d) are scans of the 42 hb sample.*

The p7560 scaffold is found to occupy an area comparable to that of the p7249 scaffold. The scaffold is mostly composed of DNA patches with a height of approximately 2.6 nm while the remaining DNA is roughly 1.1 nm. Analysing images obtained of the 42 hb DNA origami structure gives dimensions of approximately 70x40x5 nm of the core region. This is irrespective of individual structures and folding programs used. This high level of similarity

is seen in figure. 5.25 where the height profile along the width and length is compared for origami structures prepared according to each program.

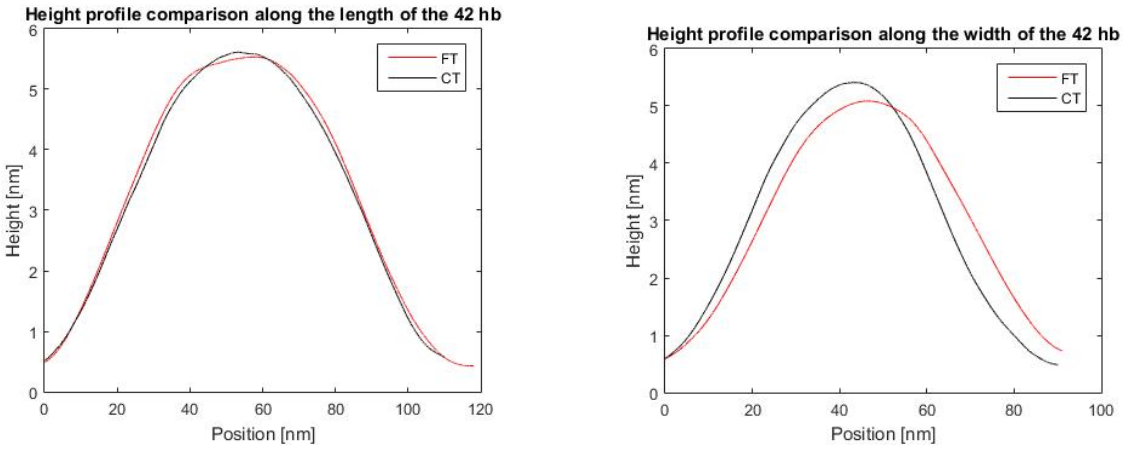

(a) (b)

FIGURE 5.25: *Height comparison along the length and width of the 42 hb structures prepared at either constant temperature (CT) or according to Tilibit recommendations (FT). The structures analysed are marked in figure. 5.24(c) and 5.24(d)*

5.7.2 Au-NP analysis

TM-AFM was conducted on samples containing synthesized Au-NPs to analyse the actual size and distribution. The information obtained will be used to discuss if actual Au-NP coupling to origami was done. Figures. 5.26(a) and 5.26(b) show images obtained from two separate sample spots for 5 nm Au-NP solution deposited on an APTMS modified mica surface. Figure. 5.26(c) shows an image of a 15 nm Au-NP solution deposited.

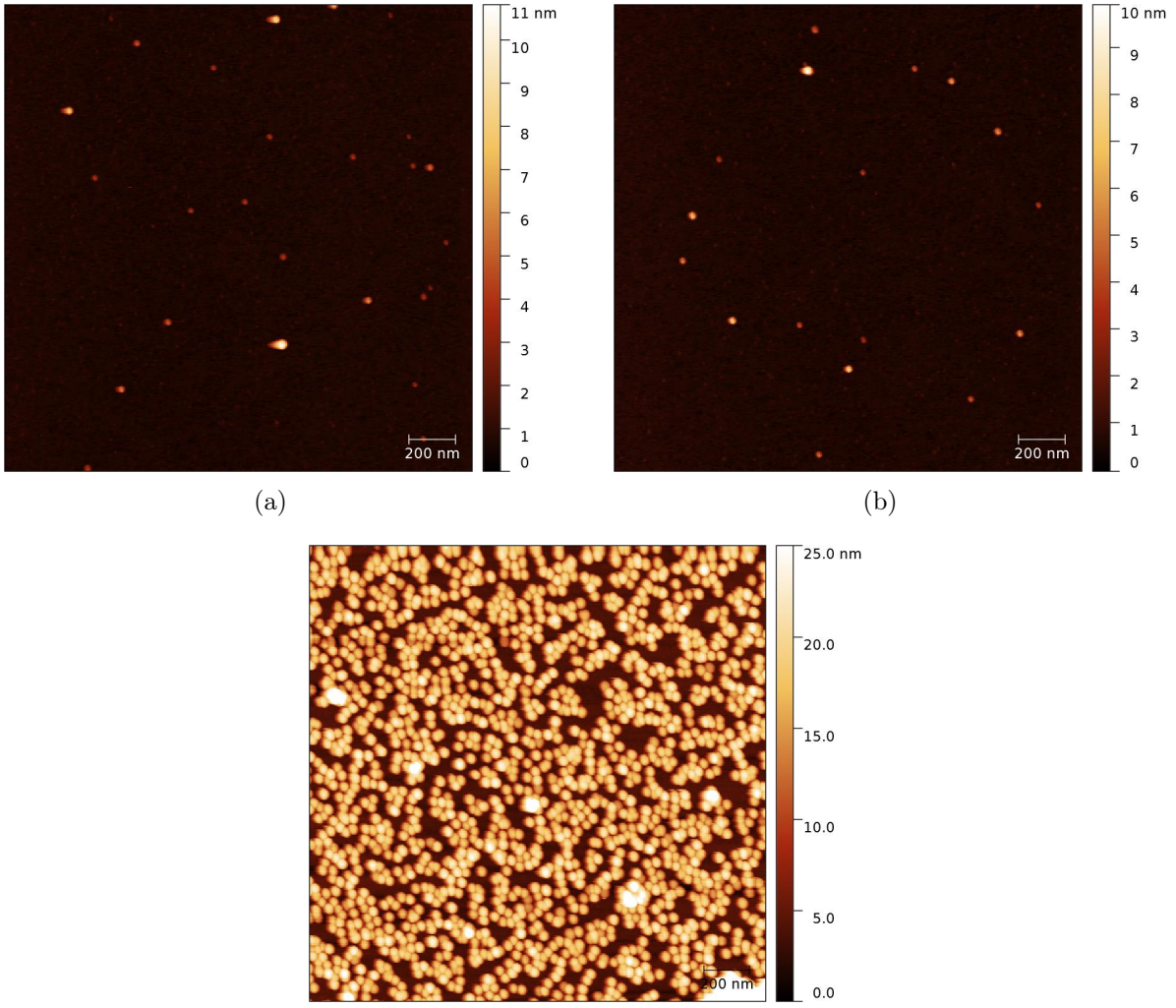

Figure 5.26: *AFM images obtained containing Au-NPs synthesized according to a recipe for 5 nm (figure. 5.26(a) and 5.26(b)) and 15 nm (figure. 5.26(c)) sized particles.*

In figure. 5.26(a) and 5.26(b), AFM imaging shows spherical nano-particles with significantly different sizes. In figure. 5.26(c) significantly larger spherical particles are seen with a high density. The size-distribution of nano-particles obtained from AFM analysis on three separate sample spots for each Au-NP batch are shown in the histogram in figure. 5.27. A total of 100 individual particles were analysed in each case.

For an Au-NP solution prepared according to a 5 nm recipe, height analysis of nano-particles by TM-AFM shows that the surface contains particles with heights between 1 and

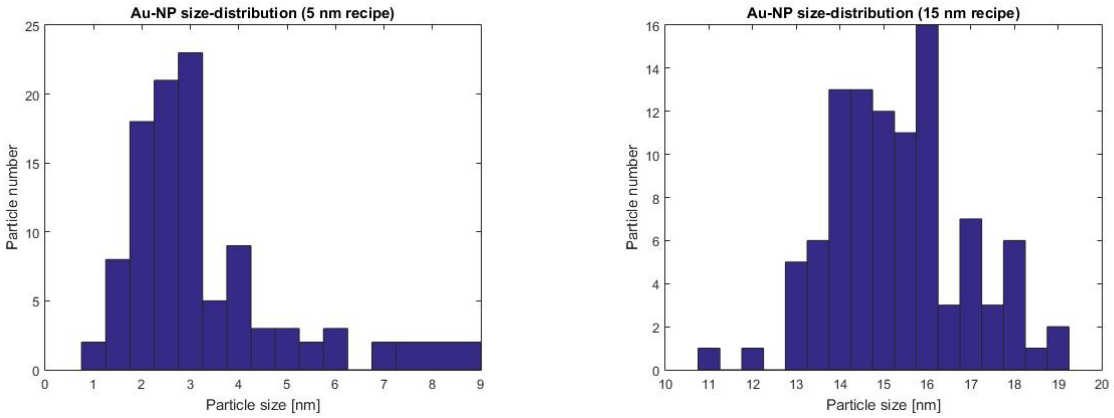

(a) (b)

FIGURE 5.27: *Size distributions of Au-NPs deposited on an APTMS modified mica surface*

9 nm. Most particles are found to have a size of 2-3 nm. For a 15 nm Au-NP solution, most particles have sizes ranging between 13-19 nm with the highest occurrence at 14-16 nm.

5.7.3 Au-NP to DNA origami conjugation

Conjugation of 5 nm Au-NPs

Due to the small size of synthesized Au-NPs, amplitude images were analysed in order to better analyse feature changes and thereby whether or not Au-NP conjugation had taken place. These are compared with amplitude images obtained of pure 42 hb samples. Finally, height analysis was done. The findings are showed in figure. 5.28.

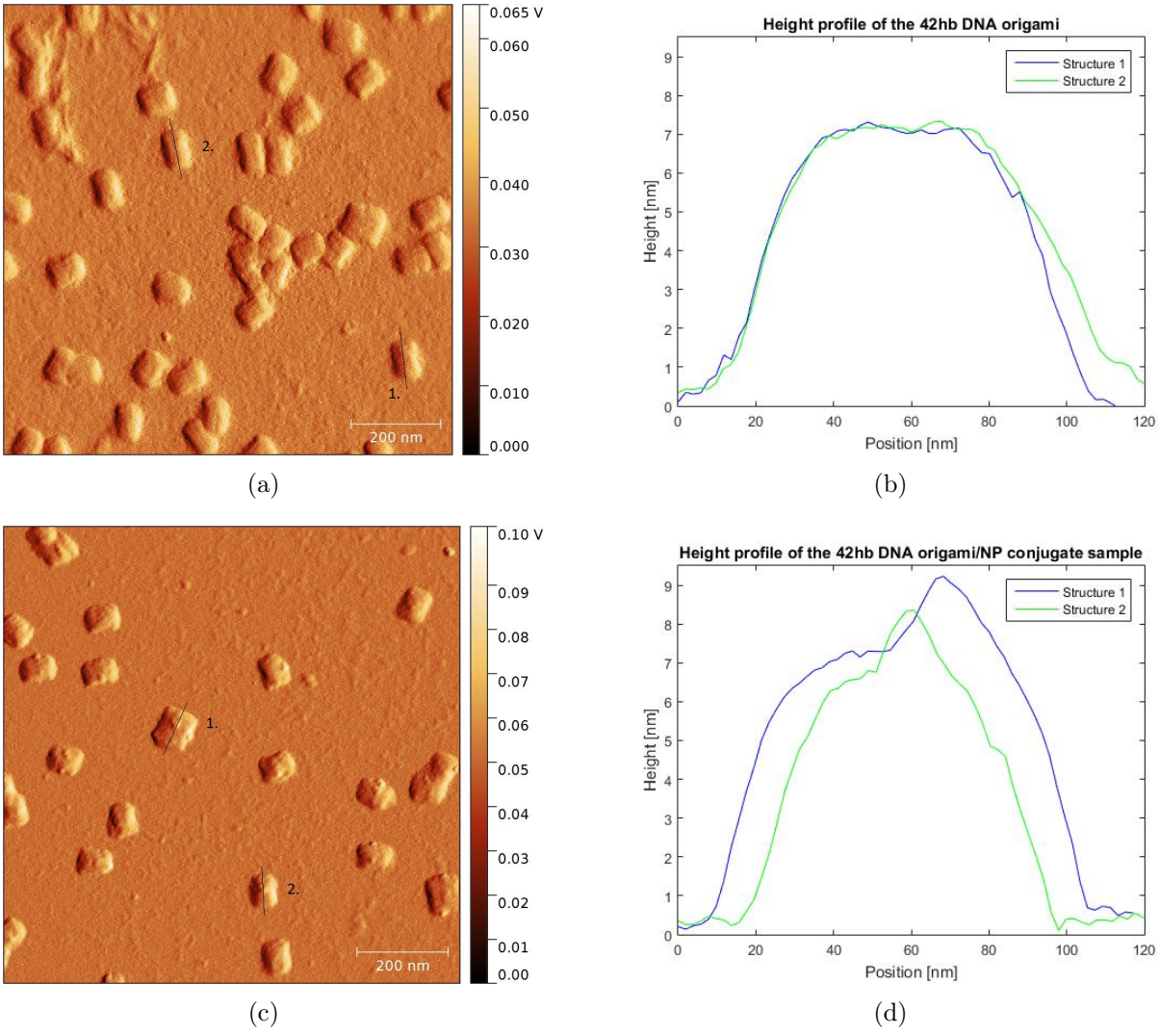

Figure 5.28: *Amplitude images of a pure 42 hb (5.28(a)) and one treated with Au-NP/DNA conjugate(5.28(c)) in addition to height analysis.*

Comparing figure. 5.28(a) and 5.28(c), features are observed in the form of one or two small bumps located on several origamis that are not present on pure 42 hb bundle samples. Bumps of 2-2.5 nm are confirmed by height profiles when comparing figure. 5.28(b) and 5.28(d).

Conjugation of 15 nm Au-NPs

The Au-NP conjugation success of 15 nm Au-NPs was based on imaging of three different areas with a combined sample size of roughly 150. An AFM image of roughly 15 nm Au-NPs conjugated onto the 42 hb in addition to conjugation statistics are seen in figure. 5.29. For this particular sample, Au-NP/DNA origami conjugates were prepared at room temperature and did not receive prior annealing.

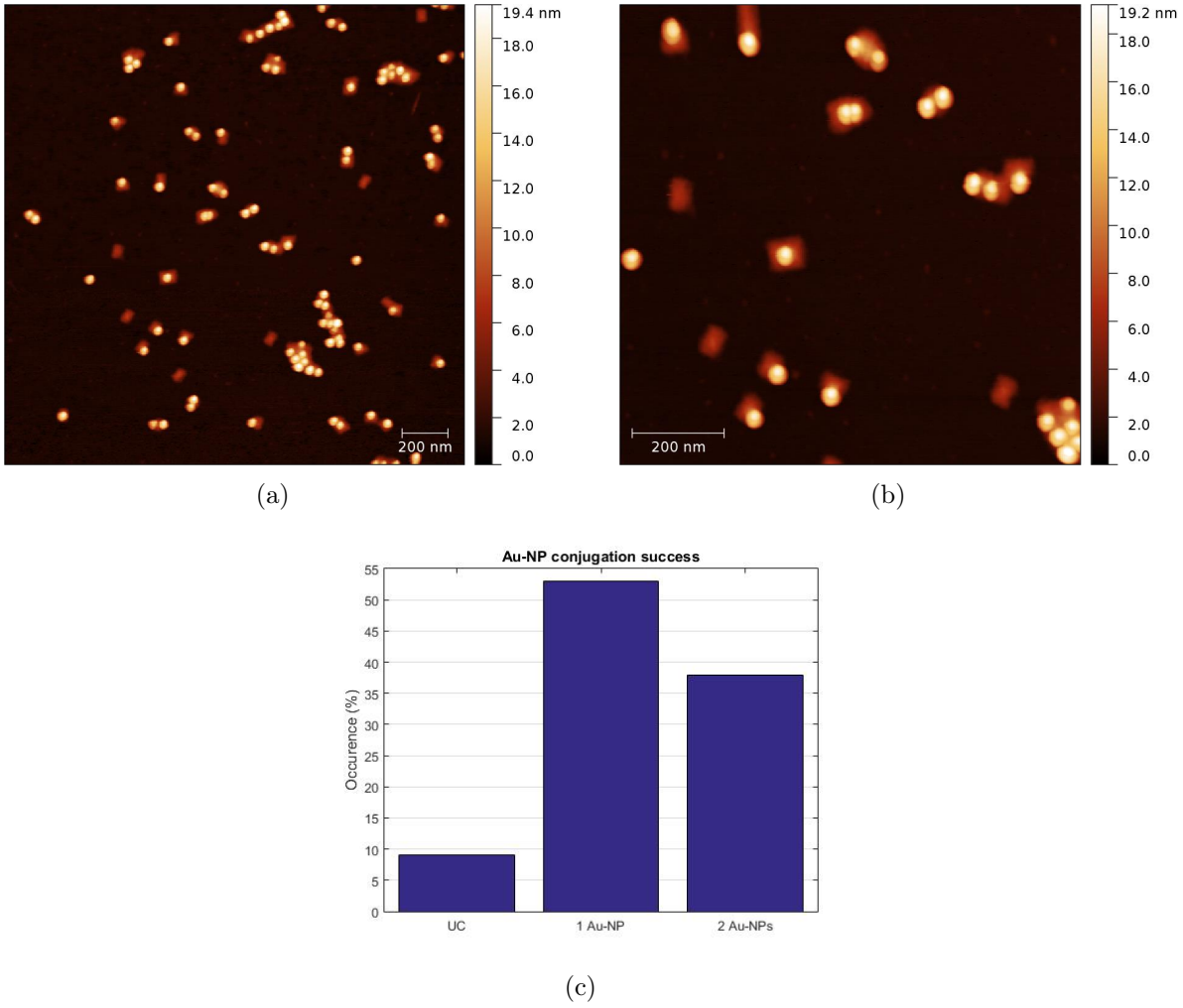

FIGURE 5.29: *AFM image obtained of roughly 15 nm Au-NPs conjugated onto the 42 hb in addition to conjugation statistics. The statistics include un-conjugated species (UC) and species where 1/2 Au-NPs are conjugated (1 Au-NP)/(2 Au-NP).*

Analysis points to that Au-NP conjugation achieves a 91 % success-rate with the occurrence of single Au-NP conjugation being the most frequent at 53 %. Successful conjugation of 2 Au-NPs is found to be significantly less with a success of 38 %. Pure origami structures are found to have a height of approximately 5 nm while particles are found to have a height mostly ranging between 10-15 nm.

No clear evidence was obtained of Au-NP conjugation onto the 18 hb origami structure for either synthesized particle batch.

6 | Discussion

6.1 Structural stability simulation

The structural properties of the 18 hb and cuboid 42 hb DNA origami structures were computationally predicted using CanDo.

The 18 hb structure was found to have regions of high stability especially in the left center, usually with RMSF values between 0.2-0.3 nm. Lower stability regions at the outer most ends of several DNA helices in the origami structure were noted as well as for larger regions of strands 9 and 16 with RMSF values of approximately 0.7 nm. The majority of scaffold and staple strand cross-overs are located in the left center region, thereby the CanDo simulation is expected to show the highest degree of stability in this particular region. The low stability regions that are seen especially at the outer right ends of the majority of the strands as well as for larger regions of helix 9 and 16 can be explained by the ordering of scaffold as well as stable strand cross-overs. Examining helices 9 and 16 in detail in the full caDNAno diagram in appendix. B.1 shows that helix 9 connects the free scaffold strand with the origami structure. This particular helix lacks strand cross-overs in the right part which is the reason for low stability. The same explanation can be given to helix 16. The diagram also reveals that the left ends of several helices such as 0, 4, 8, 11 and 17 have staple strand cross-overs that should stabilize the far outer left ends. The far right ends of the helices are not stabilized by staple strand cross-overs to the same degree which results in more flexible ends which thereby explains the differences in the stability profiles between the different ends of the helices.

The large 42 hb structure was found to have a highly symmetric stability profile. The highly consistent and stabilized center regions can be explained by a highly periodic staple strand cross-over pattern as seen in appendix. B.2. From this design, the majority of helices can at most share staple cross-overs with 3 neighbouring helices due to the general design principle of honey-comb lattice structures. As each helix is approximately 59 nm, the opportunity of creating a predominantly periodic cross-over pattern of both staple and scaffold over large areas is high. This periodicity is most successfully achieved in symmetric origami structures. The low stability for all ends is predicted due to no outer strand cross-overs which also explains the similarities between the 42 and 18 hb in this regard. Generally, DNA origami structures should benefit from highly periodic staple-strand cross-overs which should result in high stability as well as an evenly distributed stability profile.

Examining CanDo simulations of other 3D DNA origami structures reveal similar structural tendencies. [78, 79, 80]. Although these structures as well as the ones analysed in this study have greatly varying sizes, stability characteristics are similar with comparable RMSF value. The most important characteristics include high center area stability with stability decrease as one approaches the helix ends. These characteristics appear to be a natural consequence and property of 3D DNA origami structures due to the unique routing of the scaffold and staple-strand cross-overs. Most importantly, small flexible ends should not present any significant instabilities to the core regions of the structure.

Briefly examining the sheet DNA origami design in appendix. B.3 reveals significantly lower RMSF values compared to both the 18 and 42 hb structures. This is explained by the unique routing design of both the scaffold and staple strands in a 2D origami structure. Each helix in the DNA origami-sheet can at most have two nearest neighbour helices that lie in the same plane. Therefore, a helix in a single sheet can only be supported by staple-strand cross-overs that lie in the sheet-plane and thereby each helix in less structurally supported compared to fully 3D origami structures. The apparent lower stability of the DNA origami-sheet and other 2D origami structures should not necessarily compromise the structure resulting in structural degradation before actual characterization. Several other single-layered 2D DNA-origami structures with similar shape, scaffold and staple-strand cross-over pattern have been successfully studied without any additional remarks [6, 10, 81].

6.2 Simulations of the optical properties of Au-NPs and fluorophores

The optical properties of Au-NPs in addition to the quantum efficiency of a dipole were found in order to quantitatively predict the fluorescence enhancement of the ATTO-647N dye.

Irradiating both Au-NP monomers and dimers with 647 nm light results in an expected strong electric field response due to the occurrence of localized surface plasmon resonance. As light interacts with a single nano-particle, the associated electric field is expected to polarise the nano-particle resulting in a field-angle dependence formulated by combining eq. 1.1 and 1.9. This is also qualitatively observed from figure. 5.3(a). Possible discrepancies can be attributed to the quasistatic approximation used for the derivation of eq. 1.10. Analysing the same equation, moving away from the surface at y=0 would result in a non-linear decrease in the electric field as this is proportional to $\frac{1}{r}$ which initially agrees well with the data provided in figure. 5.4. The general electric field profile is in accordance with theory and derivations presented in section. 1.3.1 and in other studies [45, 57]. Lastly, the increase in electric field intensity for larger particles can be physically explained by the increase in collective oscillating electrons and is importantly in agreement with eq. 1.10. [56].

A similar electric field profile is observed in the case of an Au-NP dimer in figure. 5.3(b). The main difference is the enhanced electric field that is observed in the gap as well as the weaker electric field on the outer sides which is in good agreement with figure. 1.11. As explained in section. 1.3.1, high electric field enhancements are predicted in the gap itself

due to coulomb attraction forces between opposite charges caused by polarization by the electric field of the incoming light. This effect would also result in higher electric fields than for Au-NP monomers, which is also clearly the case. Initially, the simulation results validate the design idea of using the much enhanced local electric field in a dimer-gap in order to maximise the fluorescence emission of fluorophores according to eq. 1.20 in section. 1.4.1. As in the case with the complete electric field simulated for a single Au-NP, the field profile of the Au-NP dimer is in agreement with other computational studies performed as well [50, 57].

Analysing the electric enhancement at wavelengths between 400-800 nm in figure. 5.5 shows the occurrence of the maxima at around 550-650 nm. This agrees well with literature on the wavelength where plasmon resonance of Au-NPs occur [1]. The red-shift of the plasmon peak with an increase in particle size is expected and can physically be explained by the weakening in the restoring force outlined in section. 1.3.1. The red-shift is also observed for particles of identical sizes if the gap-distance is decreased. This can possibly be explained by increased interactions which effectively results in the occurrence of one larger particle. The increase in electric field enhancements with a decrease in gap-size is due to an increase in the coulomb interactions of opposite charges located predominantly on the part of the Au-NP surface neighbouring the gap-area.

In order to choose an optimal fluorophore for fluorescence enhancement experiments, the scattering and absorption cross-sections of single Au-NPs and Au-NPs dimers were computationally predicted in COMSOL. As seen in figure. 5.6 in section. 5.2.3, a high degree of absorption is noted around 500 nm which is approximately the wavelength at which surface plasmon resonance of Au-NPs in vacuum/water medium occurs [48]. Pronounced absorption at this particular wavelength region is therefore expected as the light absorbed is used to facilitate the oscillations of conduction band electrons as described in section. 1.3.1.

Red-shifting the wavelength relative to the resonance frequency reveals regions at 650-750 nm with a high level of scattering which is in accordance with several other theoretical predictions [82, 83, 84, 85]. Studying eq. 1.15 in section. 1.3.1 in detail reveals that the absorption cross-section is proportional to the third power of the particle radius, while for the scattering cross-section this proportion goes as the sixth power of the particle radius. As such, scattering processes are predicted to become dominant as the particle size increase, which is in qualitative accordance with the increase of $\frac{\sigma_{sca}}{\sigma_{abs}}$ with particle size increase as found in COMSOL simulations.

From these studies, $\frac{\sigma_{sca}}{\sigma_{abs}}$ is also found to be higher for a single Au-NP in a dimer set-up than a single Au-NP with identical size in a continuous medium. This is hypothesized to be caused by the fact that the dimer set-up is effectively a larger system compared to a single Au-NP. Couple this with the fact that $\frac{\sigma_{sca}}{\sigma_{abs}}$ increases with larger particles, the ratio is expected to be higher for Au-NPs in a dimer set-up compared to a single Au-NP.

Quantum efficiency simulations were performed in order to gain insight into the physical interactions between a fluorephore and Au-NPs and calculate fluorescence enhancement. Furthermore, QE simulations were also performed to validate the results concerning the choice of fluorophore obtained from Au-NP scattering and absorption cross-section

simulations. The low quantum efficiency at a wavelength of approximately 520 nm as noted in figure. 5.7 for a perpendicularly oriented dipole is a common feature for all gap and nano-particle sizes investigated which is expected due to plasmon resonance; as is the increase in QE when red-shifting the wavelength. Importantly, both of these characteristics are in agreement with the $\frac{\sigma_{sca}}{\sigma_{abs}}$ dependence found independently from COMSOL simulations. The high quantum efficiency for perpendicular oriented dipole and the high $\frac{\sigma_{sca}}{\sigma_{abs}}$ at 650-700 nm point to that light is much more efficiency scattered at wavelengths red-shifted with respect to the plasmon resonance wavelength. The clear increase in QE at all wavelengths for increasing particle sizes is expected as the scattering properties should increase. The additional increase as the gap is widened is most likely due to less quenching occurring because of longer Au-NP/dipole distances. A dipole in a parallel orientation is found to be heavily quenched for all investigated gap-sizes. This is expected as the emitted light propagates directly onto the Au-NP surface. In addition, significantly higher quenching is also observed when decreasing the gap-size which is also to be expected.

Examining the QE of a dipole in a 15 nm large gap for particles between 1 and 80 nm in section. 5.3.1 reveal several interesting findings. The initial quantum efficiency close to unity in figure. 5.10 and low normalized non-radiative decay rates in figure. 5.9 are explained by the individual small nano-particles that do not have the necessary size to facilitate strong interactions with the light emitting from the dipole. As a consequence, the dipole is not noticeably affected by the presence of the particle. This is also clearly seen as the radiative decay rate is approximately unity in all cases in addition to the non-radiative decay rate being approximately zero.

As the particle size increases, interactions between light emitting from the dipole and the particle become more pronounced which is evident from the decay rates. The steep decrease in QE of the dipole across particle sizes between 1-20 nm is evidence that single Au-NPs of these sizes are good absorbers and thereby good quenchers at this specific separation distance. This is also widely reported from both theoretical and experimental data. [48, 86]. According to the results in figure. 5.9(a) and 5.9(b) the main reason for this is the low and constant radiative decay rate that has to compete with a steadily climbing non-radiative decay rate.

As the particle size increases beyond 20 nm, the QE of the dipole is found to be very dependent on the orientation of the dipole. An increase in the fraction of light which is absorbed for a parallel oriented dipole is noted while a perpendicular orientation results in increased scattering. As a dipole oscillates in the perpendicular orientation, emission of light will undergo in the parallel direction as explained in section. 3.3, leading to less light interacting with the Au-NP compared to perpendicular directed light emission. This decreases the chance of possible absorption processes and is therefore the orientation of choice for optimal fluorescence enhancement. This is in good agreement with the power output profile in figure. 5.11.

Fluorescence enhancement calculations in figure. 5.12 and 5.13 show how the enhancement is affected by the Au-NP size in the case of both set-ups in addition to a comparison between gap-sizes of 15 and 20 nm.

The enhancement due to the presence of a single Au-NP results in a total increase factor of nearly 7. This is explained by the relatively weak electric-field enhancement at the dipole position in addition to the high degree of quenching. According to the simulation, the fluorescence enhancement dependence on the particle size is non-linear. This is explained by the fact that enhancement is dependent on E^2 according to eq. 1.20 in section. 1.4.1. The fluorescence enhancement of a dipole in a dimer-gap is significantly higher. This is a combination of less total quenching in addition to a much higher local electric field. In each set-up, it appears that the use of small Au-NPs is not advised. Small Au-NPs are found to be good absorbers and do not provide strong local electric fields thereby fluorescence is seen to be heavily quenched. It is seen from figure. 5.13 that fluorescence of a dipole in a dimer-gap of 15 nm is a factor two stronger than that of a dipole in a 20 nm gap. Higher fluorescence can be attributed to a significantly higher local electric field that outweighs the small increase in quenching.

Importantly, the simulation environment in this study was used to compare with the set-up in Acuna et. al. resulting in a good agreement. The discrepancies are likely due to the use of different simulation environments, general settings, conditions and material constants.

6.3 DNA agarose gels

In order to obtain initial insight into the quality of formed DNA origami structures, agarose gel electrophoresis was conducted. Annealing programs that differ significantly were examined. Besides examining the optimal approach in order to make well-folded origami structures, the folding programs have also been used in order to gain general knowledge into the biophysical properties of the scaffold as well as the origami structure.

6.3.1 18 helix-bundle DNA origami

It is observed when examining the findings obtained from gel photos of each individual annealing program that these can mainly be classified in two groups. The first group consists of gels where several bands are well-defined. These are the gels found in figures. 5.14(a) and 5.16 which contain samples from annealing programs A and E respectively. The other group consists of gels where there is a high degree of band-smearing for all origami samples as well as respective scaffold references and are seen in gel figures. 5.14(b), 5.14(c) and 5.15. These contain samples from annealing programs B, C and D respectively.

As each scaffold reference has undergone annealing, it is apparent that this is not merely a case of aggregated or misfolded origami structures that result in a range of structures and thereby smearing. Furthermore, it neither points to an ensemble of scaffold DNA with various secondary structures. Rather, it appears to be the physical conditions during annealing that results in partial thermal degradation of the scaffold strand. This is supported by the fact that smearing especially appears for samples that have undergone annealing at conditions of high temperatures of 70-90 °C for prolonged times of at least 60 min.

This point is further highlighted when comparing gel photos 5.14(a) , 5.14(b) and 5.14(c) where annealing programs A, B and C were used respectively. The increase in smearing is easily seen as the annealing from 90-20 $°C$ proceeds over longer time-periods. This is consistent with the results in gel photo 5.15 for program D which shows the overall highest degree of band smearing. Lastly, examining gel photo 5.16 which is of samples undergone annealing program E, the rapid temperature decrease to 65 °C followed by slow annealing appears to have no degrading effect on neither the scaffold nor the origami structures at any magnesium chloride concentration.

Smearing is also observed to be highly dependent on the concentration of $MgCl_2$ as clearly seen when comparing the origami and scaffold lanes for 0 and 4 mM $MgCl_2$ in gel photo. 5.14(b)(Program B). This pronounced smearing has been pointed out by a study conducted by Martin et al. [70]. Here a multi-layered DNA origami structure was made by subjecting the folding solutions to a thermal-annealing program with a ramp that cooled from 65 to 25°C over the course of at least 1.5 days with no $MgCl_2$ present. Increasing the $MgCl_2$ content to 2 mM resulted in the complete absence of smearing. The group theorised that the smearing was caused by gradual thermal degradation of the scaffold strand. As the scaffold is subjected to heating, $MgCl_2$ may have the effect of facilitating the formation of double-stranded DNA in the form of stem-loops that might protect against thermal degradation.

Examining samples from a range of annealing programs gives important information on the stability of the p7249 scaffold at elevated temperatures over prolonged time-periods at different concentrations of $MgCl_2$. From this study, it is advised as a general rule that the p7249 scaffold should not be subjected to temperatures over 65°C for more than approximately 20 min, preferably with a max temperature of 80°C. Additional annealing programs are needed in order to gain a more detailed understanding of the temperatures and corresponding times needed before degradation of the p7249 scaffold becomes a serious issue for the self-assembly and the yield of DNA origami structures.

Examining the location and brightness of gel bands for scaffold and origami structures reveal interesting tendencies.

From gel-photo 5.16(program E), it is seen that untreated scaffold and Sc(0) migrate similarly unlike scaffold samples annealed in the presence of $MgCl_2$ resulting in slower migration. This points to a significant change in the secondary structure of the scaffold that is highly dependent on $MgCl_2$. A possible explanation may be the formation of stem-loops that result in locally double-stranded DNA which will affect the overall 3D structure and thereby the resistance of movement through the gel. This is supported as the effective formation of double-stranded DNA requires salt that can screen the negative charges as explained in section. 1.1.

Folding solution bands are found to migrate at a slower rate compared to both the scaffold reference and a scaffold solution undergone annealing. This points to the formation of DNA origami structures. It is also seen that FS(0) migrates slightly faster than samples containing $MgCl_2$. As some salt is required in order to create properly folded origami structures, it appears that FS(0) does not contain DNA origami. The amount of salt required is dependent on each individual structure.

Examining lanes FS(16) and FS(20) in gel-photo 5.16(Program E) shows traces of material trailing behind the main band and even a slower secondary band is observed near the well which points to a new structure. This is theorised to be an aggregate structure. Aggregate structures are also seen for other origami structures at higher concentrations of $MgCl_2$ [70].

6.3.2 42 helix-bundle DNA origami

The formation of the 42 hb structure was done using a constant temperature approach as well as a folding program provided by Tilibit.

The constant temperature approach was performed at different temperature points and yielded gel bands in excellent agreement with [35]. The smearing of each sample before the main bands is strong evidence of an ensemble of structures with varying folding success. The fast migrating bands located at approximately 1250 bp have been concluded from TEM measurements to be well-folded 42 hb structures [35]. As more pronounced bands are observed for samples folding at 50°C in addition to less smearing, this temperature is optimal for this specific structure. Lower intensity bands of well-folded structures for samples at 41 and 44°C along with more smearing is likely explained by a higher degree of mis-folding due to low folding-temperatures. Samples which were run at high temperatures have no bands that correspond to correctly folded structures, instead all material migrates slower than the scaffold. The likely explanation is the presence of semi-folded structures that consist of the scaffold and a fraction of missing or partially bounded staples due to high temperature. Semi-folded structures will therefore have a combination of increased weight and larger resistance due its less compact nature which would account for its migration profile and why it travels slower than a free scaffold sample.

Comparing lanes containing the 42 hb prepared by constant temperature folding and Tilibits annealing procedure reveals main bands that have near identical migration profiles. The main difference appears to be the brightness of the band and thereby the total yield of correctly folded structures. The higher yield obtained following Tilibits folding program can be attributed to the longer folding time resulting in higher conversion of semi-folded to well-folded origami structures.

6.4 Melting analysis of p7249 and 18 hb DNA origami

Melting temperature profiles of the p7249 scaffold and the 18 hb DNA origami structure were examined to gain a deeper physical understanding of the thermo-structural stability. The experiments were also performed to gain knowledge into possible competition between DNA double-strand formation of either p7249 scaffold stem-loops and DNA origami. The melting profiles of the scaffold and origami structure were expected to differ due to the introduction of staple strands.

The formation of stem-loop structures have been a source of interest in this study and whether or not these might have an influence on the proper folding of origami structures. This is especially interesting as numerous articles use protocols which apply initial heating

at 80°C followed by rapid cooling to approximately 65-70°C and further cooling over days. The expectation is that the primary folding of the origami happens at sub 70°C. Dietz el. al have performed melting analysis on four separate DNA origami helix bundle structures and found that the structures show relatively high stability up to approximately 60-65 °C where-after melting predominantly occurs [35]. The study also found that the DNA origami structures were formed at roughly 50-55 °C. Interestingly, 60-65 ° is the area where the 18 hb DNA origami predominantly melts as well. Most importantly, the melting temperature of the scaffold is significantly lower than that of the investigated origami structures. In addition, the slight shift of the entire melting profile for the 18 hb structure is evidence that this structure is more stable most probably due to the binding of staple strands. As no issues are reported concerning stem-loop formation in large DNA origamis, it is likely that the formation of staple-connected regions are generally much more favourable and stable than stem-loops or other intra-strand connections.

In order to completely understand the melting properties, analysis has to go into association and dissociation of double-stranded DNA for both heating and cooling cycles for scaffold and scaffold/staple-strand solutions.

6.5 Au-NP absorption and conjugate analysis

Characterization of synthesized Au-NPs was done before actual conjugation to origami structures to gain insight into the size distribution so that the later conjugation success could be thoroughly evaluated.

Absorption measurements seen in figure. 5.20 reveal clear signatures of Au-NP formation. The difference in spectra shape and wavelength of peak absorption also confirms that the batches produced contain nano-particles of different sizes. The apparent red-shift in peak wavelength for the 15 nm batch is a clear indication that larger nano-particles have been produced compared to the expected 5 nm Au-NP batch. This tendency is also in agreement with plasmonic theory outlined in section. 1.3.1. The position of the absorption maximum of 15 nm Au-NPs is in good agreement with other studies [87] as well as simulation studies of the plasmon wavelength in this report. The significantly broader peak found for 5 nm Au-NP solution is a tendency that is observed for Au-NPs below 10 nm. This is physically explained by the increased rate of electron-surface collisions due to the small particle size that results in a damping of the SPR band [1, 88].

The most noteworthy finding from figure. 5.21, which examines the growth of Au-NPs, is the red-shift and change in absorbance at time intervals after the addition of sodium borohydride. In this case, the red-shift appears to be a clear indicator of Au-NP growth and can thereby be used to monitor the growth kinetics. The increase in absorbance at later measurements is possibly caused by an increase in the molar attenuation coefficient which is expected to increase for larger particles.

AFM measurements were performed to complement findings by absorbtion spectroscopy as well as give more precise information regarding the size distribution. According to statistics shown in figure. 5.27, the size of produced nano-particles prepared according to a 5 nm recipe

were mostly approximately 2-3 nm in diameter. Therefore, according to AFM analysis, it appears that the synthesized batch contains particles that neither are highly mono disperse nor contain a majority of 5 nm Au-NPs.

Differences in nanoparticle size and distribution of the provided recipe and the batch synthesized in this study can be due to differences in the reduction effectiveness of priorly prepared sodium borohydride solutions. The reduction efficiency of sodium borohydride in water decreases over time and is also highly dependent on the solution temperature as well as the pH. If left in solution, the reaction will produce hydrogen and sodium borohydroxide. [89]

Au-NPs synthesized according to the 15 nm recipe generally provided NPs of that size. In addition, significantly higher densities were achieved and each individual particle was easier to image.

AFM and absorption measurements are found to reach the same conclusions on the general size of Au-NP batches. From these studies, it appears that standard absorption measurements provide a cheap and quick method of initially monitoring and analysing the size of small Au-NPs due to the plasmonic properties of these. In addition, absorption spectroscopy was also found to provide useful information regarding Au-NP formation and growth. Although, absorption does not provide straightforward information on whether or not and to what degree the solution contains mono-disperse particles. This will require advanced study into the entire absorption spectrum [90].

Efforts were put into analysing both batches of Au-NP solutions using LM10 Nanosight equipment but imaging was unsuccessful likely due to the small nano-particle size.

Agarose gel electrophoresis was conducted to determine the conjugation efficiency between Au-NPs and thiolated single-stranded DNA. As seen in figure. 5.22, single pure Au-NPs are found to migrate at a faster rate compared to conjugates. This trend is seen in several studies [91, 92]. The main reasons for this is the increased weight due to DNA loading as well as the increase in geometric cross-section leading to a larger gel migration resistance. The migration rate of the conjugates with respect to pure Au-NPs can therefore be used to determine the loading efficiency of DNA.

6.6 AFM imaging of scaffold DNA and DNA origami

The AFM images of both scaffold solutions show that the structure is highly compact which is likely due to the formation of stem-loops. Due to the low temperature and no staple-strands present that would satisfy complementary binding, the pairing of self-complementary regions during annealing is energetically favourable. As a wide range of possible stem-loops can be formed between different regions in addition to the fact that stem-loops add minimal structural stability, a range of semi-compact structures are expected. Furthermore, scaffold DNA is found to have a relatively even height profile of $\approx$ 0.8-1.1 nm. This is well below the expected diameter of B-DNA which is approximately 2 nm as pointed out in section. 1.1. In AFM imaging, DNA is often reported to have a height ranging between 0.1-1.5 nm which is

in line with the findings in this study. The reduced height is most commonly attributed to DNA deformation done by the tip or DNA-tip adhesion forces. [93, 94, 95]

Examining AFM images of the 18 hb origami solutions reveal structural similarities with pure scaffold. The main difference is the occurrence of patches with a height of 2.7 nm and with different sizes. This is the most prevalent evidence of the formation of a DNA origami structure. The most regular patches measure ≈ 30x24x2.7 nm and are seen in figure. 5.23(d). Slightly different dimensional values can be related to the orientation and folding succes of individual structures. The two instances of string-like structures seen in figure. 5.23(d) are most likely single-stranded open ended scaffold DNA created due to partial degradation of the initial circular form.

Characterizing the folding success of the 18 hb DNA origami is difficult due to its small size which is possibly one of several reasons why such small structures are not seen in literature. Removal of excess scaffold strand could benefit in the imaging of smaller origami structures. This could be done by creating an additional origami structure. As an example, the smaller origami structure can be connected to a DNA bridge that is connected to a flat origami sheet using scaffold strand regions flanking the 18 hb structure. This is shown in appendix. B.3. Another option is the removal of the excess scaffold strand using restriction enzymes etc.

Analysing AFM images 5.24(c) and 5.24(d) of the 42 hb origami sample reveal highly well-defined and near identical rectangular structures. This points to the successful formation of the 42 hb in agreement with agarose gel electrophoresis. Comparing gel images obtained of samples prepared at a constant temperature of 50°C and Tilibit's procedure point to that the final products are indistinguishable both when analysing agarose gels but also from AFM imaging. Therefore, it appears that a 2 h fold is sufficient in obtaining correctly folded structure, the only difference being the amount of end-product as seen from gel photo 5.18. Comparing the AFM imaging results to TEM analysis reveal good agreement [35, 70].

The dimensions of the 42 hb and suspected 18 hb origami structures reveal in both cases larger than expected dimensions in-plane. The height on the other hand is significantly lower than expected. The reduced height can be explained by the same reasoning as previously stated for scaffold DNA. Measured enlargement and reduced height of DNA origami and DNA in general is also clearly observed when comparing dried and hydrated DNA samples. This is attributed to capillary effects and change in tip-sample interactions due to surrounding medium. [96, 97] In addition, the well-reported broadening caused by a probe with finite tip radius is also a potential cause in addition to the strong adhesion between DNA and mica [98, 99]. This can be seen in figure. 5.25 due to the relatively non-sharp transition between the mica surface and origami.

6.6.1 Imaging DNA origami/Au-NP conjugates

Au-NP conjugation onto the 18 hb proved unsuccessfully according to AFM imaging. In the case of conjugation primarily occurring after origami adsorption, Au-NP/ thiol connections may be sterically hindered if the origami structure is preferably adsorbed onto the mica surface via its helix sides and not its ends. An issue might also arise due to the distance of

the thiol-group from the helix end preventing the thiol group from effectively penetrating the BSPP layer and forming an Au-S bond. This problem could in principle be solved by incorporating staple overhang sections. The unsuccessful conjugation resulted in total internal reflection fluorescence experiments being omitted. As a result, focus solely shifted to Au-NP conjugation onto the 42 hb.

The height profile seen in figure. 5.28(d) of the bumps located on the origami structure fit well with the general size of the 2-3 nm Au-NPs obtained from AFM images as seen in the histogram in figure. 5.27. Yet, the small features made evaluation of actual conjugation success across numerous origami structures time-consuming.

Conjugation of 15 nm Au-NPs is much clearer and the presence of one or two Au-NPs on 42 hb origami structures can clearly be visualized when looking at the height image in figure. 5.29(a). The Au-NPs conjugated onto the 42 hb have a size of approximately 10-15 nm in agreement with the AFM analysis of individual particles.

Importantly, it is seen that at maximum two nano-particles are located on each origami structure regardless of particle size investigated. This is expected as each side has two staple-strands with overhang. The absence of observed nano-particle conjugation in the case where overhang staple-strands have been omitted from the origami structure is important in verifying that Au-NP conjugation is due to actual programmed conjugation and not random Au-NP/DNA interaction. Furthermore in each case, the actual location of one or more nano-particles fit well with the placement of the overhang staple-strands when comparing AFM images 5.29(a) and 5.29(b) with the design schematic of the 42 hb in appendix. B.2.

The conjugation of 15 nm Au-NPs onto the 42 hb was seen to surpass 90 % efficiency with predominant coupling of a single Au-NP. This yield is in the range of the highest reported conjugation success. [100, 101]

In general, studies find that the conjugation success is dependent on incubation time in addition to the use of temperature annealing programs. Groups have also achieved great success in coupling Au-NPs to DNA origami via staple strands containing mono-thiol or bis-thiol groups at room temperature. [100] The coupling of two Au-NPs onto a DNA origami was in one case found to go from 45 % to 91 % in yield when switching from mono to bis-thiol modified staple-strands [101].

As there was not found to be any significant statistical difference in conjugation success of pre-annealing an Au-NP/origami solution before deposition, it appears that conjugation predominantly occurs on the mica surface and not in solution. It is theorized that the adsorption of origami onto mica creates a stationary environment for nano-particles to better couple. This finding is interesting as a study done by Wang et. al. following the same annealing procedure as in this report experienced successful conjugation only in the case of several hours of pre-annealing [102]. A possible reason is the relatively long deposition time of 10 min used in this report, vs. 3 min in Yang et. al. which, in the case of this study, appears to be adequate in achieving a high conjugation yield on pre-adsorbed origami. Additionally, it remains unclear what the concentration of incubated Au-NPs was in Wang et. al. The high excess of Au-NP to DNA origami (approximately 30/1) used in this report most likely has a high impact on the coupling kinetics.

7 | Conclusion

In this project, simulations of the optical properties of Au-NPs were analysed in addition to the properties of a dipole used for predicting fluorescence enhancement in a nano-antenna set-up. The geometrical element in the set-up was envisioned to be DNA origami structures of which an 18 and 42 hb were thoroughly examined using AFM and agarose gel electrophoresis. Lastly, conjugation of Au-NPs onto the structures was attempted.

It was found from COMSOL and Lumerical simulations that the optimal choice of a fluorophore is one with excitation and emission wavelengths red-shifted with respect to the plasmon resonance wavelength of Au-NPs. A fluorescence enhancement of approximately 385 times was found for a simulated ATTO-647N dye in an Au-NP dimer-gap of 15 nm containing 100 nm particles. The use of small Au-NPs are not advised as these are found to be good quenchers. In addition, QE and electric field data was found for dimer-gaps of 5, 10 and 20 nm containing several sizes of Au-NPs. Similar in-depth studies were not found to be provided in literature according to the authors knowledge. The data can be used as an approximation for systems of varying dimensions in other studies.

Gel analysis of both the 18 and 42 hb provided important information regarding the preparation of origami structures. In both cases, obtained gels were found to be useful tools in determining the quality of folding for structures prepared by various folding programs. According to gel analysis, the p7249 scaffold was prone to degradation at temperatures of 65°C for more than approximately 20 min.

According to AFM studies of the 18 hb, the folding success was difficult to determine due to the inherent small size of this origami structure, although evidence of the formation of an origami structure was found. The folding of the 42 hb was found to be highly successful from both agarose gel electrophoresis and AFM analysis providing results that were found to be nearly identical with findings in literature. In addition, it was found that the 42 hb can be properly folded at a constant temperature of 50°C for merely 2 h with good yields. Higher yields can be achieved if the solution is prepared using the more time-consuming folding program provided by Tilibit Nanosystems. AFM and agarose gel electrophoresis are found to be a powerful analytical combo for the characterization of origami structures and is therefore advised in future studies.

The synthesis of Au-NPs was successful although in the case of a recipe for 5 nm Au-NPs, smaller particles were synthesized. The recipe for 15 nm particles generally provided particles of that size as seen from AFM. Absorption spectroscopy was also found to provide

good initial estimation on the particle size in addition to the monitoring of the growth kinetics.

Conjugation of 15 nm Au-NPs onto the 42 hb structure was shown from AFM imaging to be successful thereby fulfilling one of the primary goals of this study. 53 % of analysed 42 hb structures were shown to have a single Au-NP conjugated, 36 % two Au-NPs while the remaining showed no signs of conjugation. In addition, Au-NP placement was found to fit well with the placement of overhang staple strands thereby showing the promise of this conjugation technique for precise placement of Au-NPs. The high conjugation success and precise placement of Au-NPs shown in this study make the 42 hb structure a candidate for further studies in the fabrication of nano-photonics circuits and biosensors.

Bibliography

[1] Xiaohua Huang and Mostafa A. El-Sayed. Gold nanoparticles: Optical properties and implementations in cancer diagnosis and photothermal therapy. *Journal of Advanced Research*, Vol. 1(1):pp. 13–28, 2010.

[2] Yunan Cheng; Mang Wang; Gustaff Borghs and Hongzheng Chen. Gold Nanoparticle Dimers for Plasmon Sensing. *Langmuir*, Vol. 27:pp. 7884–7891, 2011.

[3] Alexander S. Urban; Andrey A. Lutich; Fernando D. Stefani and Jochen Feldmann. Laser printing single gold nanoparticles. *Nano letters*, Vol. 10(12):pp. 4794–8, 2010.

[4] Ryan J. Kershner; Luisa D. Bozano; Christine M. Micheel; Albert M. Hung; Ann R. Fornof; Jennifer N. Cha; Charles T. Rettner; Marco Bersani; Jane Frommer; Paul W. K. Rothemund and Gregory M. Wallraff. Placement and orientation of individual DNA shapes on lithographically patterned surfaces. *Nature Nanotechnology*, Vol. 4(9):pp. 557–561, 2009.

[5] Nadrian C. Seeman. Nanomaterials based on DNA. *Annual Review of Biochemistry*, Vol. 79:pp. 65–87, 2010.

[6] Paul W. K. Rothemund. Folding DNA to create nanoscale shapes and patterns. *Nature*, Vol. 440(7082):pp. 297–302, 2006.

[7] Ralf Dahm. Discovering DNA: Friedrich Miescher and the early years of nucleic acid research. *Human Genetics*, Vol. 122(6):pp. 565–581, 2008.

[8] Jeremy M. Berg; John L. Tymoczko and Lubert Stryer. *Biochemistry*. W. H. Freeman, seventh edition, 2010.

[9] J. D. Watson and F. H. C. Crick. A structure for deoxyribose nucleic acid. *Nature*, Vol. 171:pp. 737–738, 1953.

[10] Jürgen J. Schmied; Mario Raab; Carsten Forthmann; Enrico Pibiri; Thorben Dammeyer and Philip Tinnefeld. DNA origami-based standards for quantitative fluorescence microscopy. *Nature Protocols*, Vol. 9(6)(pp. 1367-1391), 2014.

[11] Shawn M. Douglas; Hendrik Dietz; Tim Liedl; Björn Högberg; Franziska Graf and William M. Shih. Self-assembly of DNA into nanoscale three-dimensional shapes. *Nature*, Vol. 459(7250):pp. 414–418, 2009.

[12] Zhi-Jie Tan and Shi-Jie Chen. Nucleic acid helix stability: Effects of salt concentration, cation valence and size, and chain length. *Biophysical Journal*, Vol. 90(4):pp. 1175–1190, 2006.

[13] James Watson. *Molecular Biology of the Gene*. Cold Spring Harbor Laboratory Press, 5th edition edition, 2003. p. 102.

[14] Structure of a B-DNA dodecamer. Conformation and dynamics - http://www.rcsb.org/pdb/explore.do?structureid=1bna.

[15] Martin Gaudier; Barbara S. Schuwirth; Sarah L. Westcott and Dale B. Wigley. Structural Basis of DNA Replication Origin Recognition by an ORC Protein. *Science*, Vol. 317(5842):pp. 1213–6, 2007.

[16] Carole A. Bewley; Angela M. Gronenborn and G. Marius Clore. Minor Groove-Binding Architectural Proteins: Structure, Function, and DNA Recognition. *Annual review of biophysics and biomolecular structure*, Vol. 27:pp. 105–31, 1998.

[17] Reginald H. Garrett and Charles M. Grisham. *Biochemistry*. Brooks Cole, 5th edition, 2012.

[18] Gerald S. Manning. The Persistence Length of DNA Is Reached from the Persistence Length of Its Null Isomer through an Internal Electrostatic Stretching Force. *Biophysical Journal*, Vol. 91(10):pp. 3607–3616, 2006.

[19] James G. Wetmur and Norman Davidson. Kinetics of Renaturation of DNA. *Journal of Molecular Biology*, Vol. 31(3)(pp. 349-370), 1968.

[20] J. Stenesh. *Biochemistry*. Springer, 1998.

[21] C. A. Miles and B. M. Mackey. Survival and biological activity of heat damaged DNA. *Letters in Applied*, Vol. 27(5):pp. 279–282, 1998.

[22] Moshe Karni; Dolev Zidon; Pazit Polak; Zeev Zalevsky and Orit Shefi. Thermal degradation of DNA. Vol. 32(6):pp. 298–301, 2013.

[23] E. J. Sambriski; D. C. Schwartz and J. J. de Pablo. A Mesoscale Model of DNA and Its Renaturation. *Biophysical Journal*, Vol. 96(5):pp. 1675–1690, 2009.

[24] Jeremy M Berg; John L Tymoczko and Lubert Stryer. *Biochemistry*. W. H., 5th edition, 2002.

[25] Michael Levitt. Folding of nucleic acids. *Polymerization in Biological Systems, Ciba Foundation Symposium*, Vol. 7:pp. 147–171, 2009.

[26] Nadrian C. Seeman. DNA in a material world. *Nature*, Vol. 421(6921):pp. 427–31, 2003.

[27] https://www.eurofinsgenomics.eu/en/dna-rna-oligonucleotides/custom-dna-oligos.aspx.

[28] Chengde Mao. The Emergence of Complexity: Lessons from DNA. *PLoS Biology*, Vol. 2(12):p.e431, 2004.

[29] David M. J. Lilley. Structures of helical junction in nucleic acids. *Quarterly Reviews of Biophysics*, Vol. 33(2):pp. 109–159, 2000.

[30] Barbara Saccà and Christof M. Niemeyer. DNA Origami: The Art of Folding DNA. *Angewandte*, Vol. 51(1):pp. 58–66, 2012.

[31] Yu-Chueh Hung; Dennis M. Bauer; Ishtiaq Ahmed and Ljiljana Fruk. DNA from natural sources in design of functional devices. *Methods*, Vol. 67(2):pp. 105–115, 2014.

[32] Jean-Michel Arbona; Jean-Pierre Aimé and Juan Elezgaray. Folding of DNA origamis. *Frontiers in Life Science*, Vol. 6(1-2):pp. 11–18, 2012.

[33] Frits Dannenberg; Katherine E. Dunn; Jonathan Bath; Marta Kwiathowska; Andrew J. Turberfield and Thomas E. Ouldridge. Modelling DNA origami self-assembly at the domain level. *The Journal of Chemical Physics*, Vol. 143(16):pp. 165102, 2015.

[34] Katherine E. Dunn; Frits Dannenberg; Thomas E. Ouldridge; Marta Kwiathowska; Andrew J. Turberfield and Jonathan Bath. Guiding the folding pathway of DNA origami. *Nature*, Vol. 525(7567):pp. 82–6, 2015.

[35] Jean-Philippe J. Sobczak; Thomas G. Martin; Thomas Gerling and Hendrik Dietz. Rapid Folding of DNA into Nanoscale Shape at Constant Temperature. *Science*, Vol. 338(6113):p. 1458(4), 2012.

[36] Satoko Yoshizawa, editor. *Nanotechnology Tools for the Study of RNA*. Academic Press, 1 edition, 2016. p. 144.

[37] Shawn M. Douglas; Adam H. Marblestone; Surat Teerapittayanon; Alejandro Vazquez and George M. Church. Rapid prototyping of 3D DNA-origami shapes with caDNAno. *Nucleic Acids Research*, Vol. 37(15):pp. 5001–5006, 2009.

[38] http://cando-dna-origami.org/about/.

[39] Eleonora Petryayeva and Ulrich J. Krull. Localized surface plasmon resonance: Nanostructures, bioassays and biosensing - a review. *Analytica Chimica Acta*, Vol.706(1):pp. 8–24, 2011.

[40] Neil W. Ashcroft and N. David Mermin. *Solid State Physics*. Saunders College Publishing, 1st edition, 1976.

[41] Katherine A. Willets and Richard P. Van Duyne. Localized surface plasmon resonance spectroscopy and sensing. *Annual Review of Physical Chemistry*, Vol. 58:pp. 267–297, 2007.

[42] Anatoly V. Zayats; Igor I. Smolyaninov and Alexei A. Maradudin. Nano-optics of surface plasmon polaritons. *Physics Reports*, Vol. 408(3):pp.131–314, 2005.

[43] Sujit Kumar Ghosh and Tarasankar Pal. Interparticle Coupling Effect on the Surface Plasmon Resonance of Gold Nanoparticles: From Theory to Applications. *Chemical Reviews*, Vol. 107(11):pp. 4797–862, 2007.

[44] Robert W. Christy; John R. Reitz and Frederick J. Milford. *Foundations of Electromagnetic Theory*. Pearson, fourth edition, 2009. pp. 115-117.

[45] Xiaofeng Fan; Weitao Zheng and David J. Singh. Light scattering and surface plasmons on small spherical particles. *Light: Science and Applications*, Vol. 3(6):p.e179, 2014.

[46] Traci R. Jensen; Michelle L. Duval; K. Lance Kelly; Anne A. Lazarides; George C. Schatz and Richard. Nanosphere Lithography: Effect of the External Dielectric Medium on the Surface Plasmon Resonance Spectrum of a Periodic Array of Silver Nanoparticles. *Journal of Physical Chemistry B*, Vol. 103(45):p. 9846(8), 1999.

[47] Matthew Pelton and Garnett W. Bryant. *Introduction to Metal-Nanoparticle Plasmonics*. Wiley, 1st edition, 2013.

[48] Prashant K. Jain; Kyeong Seok Lee; Ivan H. El-Sayed and Mostafa A. El-Sayed. Calculated Absorption and Scattering Properties of Gold Nanoparticles of Different Size, Shape, and Composition: Applications in Biological Imaging and Biomedicine. *Journal of Physical Chemistry B*, Vol. 110(14):pp. 7238–7248, 2006.

[49] Z. B. Wang; B. S. Luk'yanchuk; W. Guo; S. P. Edwardson; D. J. Whitehead; L. Li; Z. Liu and K. G. Watkins. The influences of particle number on hot spots in strongly coupled metal nanoparticles chain. *The Journal of Chemical Physics*, Vol. 128(094705), 2008.

[50] Taerin Chung; Seung-Yeol Lee; Eui Young Song; Honggu Chun and Byoungho Lee. Plasmonic Nanostructures for Nano-Scale Bio-Sensing. *Sensors*, Vol. 11(11):pp. 10907–10929, 2011.

[51] Yijun Tang; Xiangqun Zeng and Jennifer Liang. Surface Plasmon Resonance: An Introduction to a Surface Spectroscopy Technique. *Journal of Chemical Education*, Vol. 87(7):pp. 742–746, 2010.

[52] Zhanghua Han and Sergey I. Bozhevolnyi. Radiation guiding with surface plasmon polaritons. *Reports on Progress in Physics*, Vol. 76(1):p.016402 (37pp), 2013.

[53] S. A. Maier. *Plasmonics: Fundamentals and Applications*. Springer, 1st edition, 2007. pp. 21-34.

[54] Emmanuel Fort and Samuel Grésillon. Surface enhanced fluorescence. *Journal of Physics D: Applied Physics*, Vol. 41(1):p.013001 (31pp), 2008.

[55] Joseph R. Lakowicz. *Principles of Fluorescence Spectroscopy*. Springer, 3rd edition, 2011.

[56] Susie Eustis and Mostafa A. El-Sayed. Why gold nanoparticles are more precious than pretty gold: Noble metal surface plasmon resonance and its enhancement of the

radiative and nonradiative properties of nanocrystals of different shapes. *Chemical Society Reviews*, Vol. 35(3):pp. 209–217, 2006.

[57] G. P. Acuna; F. M. Moller; P. Holzmeister; S. Beater; B. Lalkens and P. Tinnefeld. Fluorescence Enhancement at Docking Sites of DNA-Directed Self-Assembled Nanoantennas. *Science*, Vol. 338(506):pp. 506–510, 2012.

[58] Krasimir Vasilev; Wolfgang Knoll and Maximilian Kreiter. Fluorescence intensities of chromophores in front of a thin metal film. *The Journal of Chemical Physics*, Vol. 120(7):pp. 3439–3445, 2004.

[59] Yunan Cheng, Tim Stakenborg, Pol Van Dorpe, Liesbet Lagae, Mang Wang, Hongzheng Chen, and Gustaaf Borghs. Fluorescence near gold nanoparticles for DNA sensing. *Analytical chemistry*, Vol. 83(4):pp. 1307–1314, 2011.

[60] Palash Bharadwaj and Lukas Novotny. Spectral dependence of single molecule fluorescence enhancement. *Optics express*, Vol. 15(21):pp. 14266–74, 2007.

[61] Guozhong Cao. *Nanostructures and Nanomaterials: Synthesis, Properties and Applications*. Imperical College Press, 2004. pp. 63-72.

[62] Nguyen T. K. Thanh; N. Maclean and S. Mahiddine. Mechanisms of Nucleation and Growth of Nanoparticles in Solution. *Chemical Reviews*, Vol. 114(15):pp. 7610–30, 2014.

[63] Puspanjali Sahu and Bhagavatula L. V. Prasad. Time and Temperature Effects on the Digestive Ripening of Gold Nanoparticles: Is There a Crossover from Digestive Ripening to Ostwald Ripening. *Langmuir: the ACS journal of surfaces and colloids*, Vol. 30(34):pp. 10143–50, 2014.

[64] I. M. Lifshitz and V. V. Slyozov. The kinetics of precipitation from supersaturated solid solutions. *Journal of Physics and Chemistry of Solids*, Vol. 19(1):pp. 35–50, 1961.

[65] T. Yao; Z. Sun; Y. Li; Z. Pan; H. Wei; Y. Xie; M. Nomura; Y. Niwa; W. Yan; Z. Wu; Y. Jiang; Q. Liu and S. Wei. Insights into Initial Kinetic Nucleation of Gold Nanocrystals. *Journal of Americal Chemical Society*, Vol. 132(22):pp. 7696–701, 2010.

[66] Ernets M. Hotze; Tanapon Phenrat and Gregory V. Lowry. Nanoparticle Aggregation: Challenges to Understanding Transport and Reactivity in the Environment. *Journal of Environmental Quality*, Vol, 39(6):pp. 1909–24, 2010.

[67] *Van Der Waals Force: A Handbook for Biologists, Chemists, Engineers, and Physicists*. Cambridge University Press, 2005.

[68] Alicja Mikolayczyk; Agnieszka Gajewicz; Bakhtiyor Rasulev; Nicole Schaeublin; Elisabeth Maurer-Gardner; Saber Hussain; Jerzy Leszczynski and Thomas Puzyn. Zeta Potential for Metal Oxide Nanoparticles: A Predictive Model Developed by a Nano-Quantitative Structure-Property Relationship Approach. *Chemistry of Materials*, Vol. 27(7):pp. 2400–2407, 2015.

[69] Wenting Zhao; Thomas M. H. Lee; Sharon S. Y. Leung and I Ming Hsing. Tunable stabilization of gold nanoparticles in aqueous solutions by mononucleotides. *Langmuir*, Vol. 23 (13):pp. 7143–7147, 2007.

[70] Thomas G. Martin and Hendrik Dietz. Magnesium-free self-assembly of multi-layer DNA objects. *Nature Communications*, Vol. 3:p. 1103, 2012.

[71] P. B. Johnson and R. W. Christy. Optical Constants of the Noble Metals. *Physical Review*, Vol. 6(12):pp. 4370–4379, 1972.

[72] S.P. Yushanov; J.S. Crompton and K.C. Koppenhoefer. Scattering of Electromagnetic Waves. In *Comsol Conference Boston*, 2013.

[73] Sergei Yushanov; Jeffrey S. Crompton and Kyle C. Koppenhoefer. Mie Scattering of Electromagnetic Waves. In *Comsol Conference Boston*, 2013.

[74] /www.atto-tec.com/attotecshop/.

[75] Lukas Novotny and Bert Hecht. *Principles of Nano-optics*. Cambridge University Press, 2006. pp. 268-273.

[76] J. Sambrook; E.F. Fritsch and T. Maniatis. *Molecular Cloning*, volume II. Cold Spring Harbor Laboratory, 2nd edition, 1989. p. 11,46.

[77] John Turkevich; Peter Cooper Stevenson and James Hillier. A study of the nucleation and growth processes in the synthesis of colloidal gold. *Discussions of the Faraday Society*, Vol. 11:pp. 55–75, 1951.

[78] Hendrik Dietz, Shawn M Douglas, and William M Shih. Folding DNA into twisted and curved nanoscale shapes. *Science*, Vol. 325(5941):pp. 725–730, 2009.

[79] http://cando-dna-origami.org/examples/.

[80] Carlos Ernesto Castro; Fabian Kilchherr; Do-Nyun Kim; Enrique Lin Shiao; Tobias Wauer; Philipp Wortmann; Mark Bathe and Hendrik Dietz. A primer to scaffolded DNA origami. *Nature methods*, Vol. 8(3):pp. 221–229, 2011.

[81] Alexandria N Marchi; Ishtiaq Saaem; Briana N Vogen; Stanley Brown and Thomas H Labean. Toward larger DNA origami. *Nano Letters*, Vol. 14(10):pp. 5740–7, 2014.

[82] Palash Bharadwaj; Pascal Anger and Lukas Novotny. Nanoplasmonic enhancement of single-molecule fluorescence. *Nanotechnology*, Vol. 18(4):p.044017 (5pp), 2007.

[83] M. Thomas; J.-J. Greffet; R. Carminati and J. R. Arias-Gonzalez. Single-molecule spontaneous emission close to absorbing nanostructures. *Applied Physics Letters*, Vol. 85(17):pp. 3863–3865, 2004.

[84] A. Zasedatelev; A. Karpo; I. Feofanov; V. Krasovskii and V. Pushkarev. Plasmon-Exciton Interaction in AuNP-Phtalocyanine Core/Shell Nanostructures. *Jornal of Physics*, Vol. 541(1):p. 012064 (6pp), 2014.

[85] Pascal Anger; Palash Bharadwaj and Lukas Novotny. Enhancement and quenching of single-molecule fluorescence. *Physical Review Letters*, Vol. 96(11):pp. 113002, 2006.

[86] Jose H. Hodak; Arnim Henglein and Gregory V. Hartland. Photophysics of Nanometer Sized Metal particles: Electron-Phonon Coupling and Coherent Excitation of Breathing Vibrational Modes. *Jornal of Physical Chemistry*, Vol. 104(43):pp. 9954–965, 2000.

[87] You Qiu He; Shao Pu Liu; Ling Kong and Zhong Fang Liu. A study on the size and concentration of gold nanoparticles by spectra of absorption, resonance Rayleigh scattering and resonance non-linear scattering. *Spectrochimica Acta Part A: Molecular and Biomolecular Spectroscopy*, Vol. 61(13):pp. 2861–2866, 2005.

[88] U. Kreibig and C. von Fragsetein. The limitation of electron mean free path in small silver particles. *Z Phys*, Vol. 224:pp. 307–23, 1969.

[89] H.I. Schlesinger. Sodium borohydride, its hydrolysis and its use as a reducing agent and in the generation of hydrogen. *J. Am. Chem. Soc.*, Vol. 75, 1953.

[90] Vincenzo Amendola and Moreno Meneghetti. Size Evaluation of Gold Nanoparticles by UV-vis Spectroscopy. *The Journal of Physical Chemistry. C*, Vol. 113(11):pp. 4277–4285, 2009.

[91] Natalia Borovok; Elad Gillon and Alexander Kotlyar. Synthesis and Assembly of Conjugates Bearing Specific Numbers of DNA Strands per Gold Nanoparticle. *Bioconjugate*, Vol. 23(5):pp. 916–22, 2012.

[92] Gennady Eidelshtein; Moran Fattal; Gavriel Avishai; Benjamin Kempinski; Clelia Giannini and Alexander Kotlyar. Preparation, Characterization and Manipulation of Conjugates between Gold Nanoparticles and DNA. *Nanomaterials*, Vol. 6(9):pp. 167(8), 2016.

[93] T. Thundat; D. P. Allision and R. J. Warmack. Stretched DNA structures observed with atomic force microscopy. *Nucleic Acids Research*, Vol. 22(20):pp. 4224–8, 1994.

[94] Carlos Bustamante; James Vesenka; Chun Lin Tang; William Rees; Martin Guthold and Rebecca Keller. Circular DNA molecules imaged in air scanning force microscopy. *Biochemistry*, Vol. 31(1):pp. 22(5), 1992.

[95] Y. L. Lyubchenko; P. I. Oden; D. Lampner; S. M. Lindsay and K. A. Dunker. Atomic force microscopy of DNA and bacteriophage in air, water and propanol: the role of adhesion forces. *Nucleic*, Vol 21(5):pp. 1117–23, 1993.

[96] Cheikh Tidiane Diagne; Christophe Brun; Didier Gasparutto; Xavier Baillin and Raluca Tiron. DNA Origami Mask for Sub-Ten Nanometer Lithography:. *ACS nano*, Vol. 10(7):pp. 6458–63, 2016.

[97] Yuri Lyubchenko and Luda S. Shlyakhtento. Vsualization of Supercoiled DNA with Atomic Force Microscopy in situ. *Proceedings of the National Academy of Sciences of the United States of America*, Vol. 94(2):pp. 496–501, 1997.

[98] T. Thundat; D. P. Allision; R. J. Warmack; G. M. Brown; K. B. Jacobson; J.J. Schrick and T. L. Ferrell. Atomic force microscopy of DNA on mica and chemically modified mica. *Scanning Microscopy*, Vol. 6(4):pp. 911–8, 1992.

[99] J. Vesenka; M. Guthold; C. L. Tang; D. Keller; E. Delaine and C. Bustamante. Substrate preparation for reliable imaging of DNA molecules with the scanning force microscope. *Ultramicroscopy*, Vol. 42-44 (Pt B):pp. 1243–9, 1992.

[100] Masayuki Endo; Yangyang Yang; Tomoko Emura; Kumi Hidaka and Hiroshi Sugiyama. Programmed placement of gold nanoparticles onto a slit-type DNA scaffold. *Chemical Communications*, Vol. 47(38):pp. 10743–10745, 2011.

[101] Jaswinder Sharma; Rahul Chhabra; Casper S. Andersen; Kurt V. Gothelf; Hao Yan and Yan Liu. Toward Reliable Gold Nanoparticle Patterning On Self-Assembled DNA Nanoscaffold. *Journal of the American Chemical Society*, Vol. 130(25):pp. 7820–1, 2008.

[102] Risheng Wang; Colin Nuckolls and Shalom J. Wind. Assembly of Heterogeneous Functional Nanomaterials on DNA Origami Scaffolds. *Angewandte Chemie International Edition*, Vol. 51(45):pp. 11325–11327, 2012.

A | Derivation of SPR conditions

The derivation uses the wave-equation shown in eq. A.1 as a starting point.

$$\nabla^2\mathbf{E} - \frac{\varepsilon}{c^2}\frac{\partial^2\mathbf{E}}{\partial t^2} = 0 \tag{A.1}$$

Where $\mathbf{E}$ is the electric field vector, ε is the permittivity of the system, c is the speed of light and t is the time. A harmonic time-dependence of the electric-field is assumed, which results in a monochromatic wave described by $\mathbf{E}(\mathbf{r},t) = \mathbf{E}(\mathbf{r})e^{-i\omega t}$. Inserting this expression into eq. A.1 results in eq. A.2, which is the Helmholtz equation.

$$\nabla^2\mathbf{E} + k_0^2\varepsilon\mathbf{E} = 0 \tag{A.2}$$

where $k_0 = \frac{\omega}{c}$. The wave is set to propagate in the x-direction with an electric field described by $\mathbf{E}(x,y,z) = \mathbf{E}(z)e^{i\beta x}$, where $\beta = k_x$, which is the x-component of the wave-vector. Inserting this into eq. A.2 gives:

$$\frac{\partial^2\mathbf{E}(z)}{\partial z^2} + (k_0^2\varepsilon - \beta^2)\mathbf{E}(z) = 0 \tag{A.3}$$

Expressions for the field components of $\mathbf{E}$ and $\mathbf{H}$ are necessary in order to describe the dispersion of propagating waves and the spatial profile. Using the expressions for the curl of $\mathbf{E}$ and $\mathbf{H}$, $\nabla\times\mathbf{E} = -i\omega\mu_0\mathbf{H}$ and $\nabla\times\mathbf{H} = -i\omega\varepsilon_0\mathbf{E}$ in the case of harmonic time dependence

of ($\frac{\partial}{\partial t} = i\beta$) and using $\frac{\partial}{\partial x} = i\beta$ and $\frac{\partial}{\partial y} = 0$, the following is derived.

$$\frac{\partial E_z}{\partial y} - \frac{\partial E_y}{\partial z} = i\omega\mu_0 H_x \quad \Rightarrow \quad \frac{\partial E_y}{\partial z} = i\omega\mu_0 H_x \tag{A.4a}$$

(A.4b)

$$\frac{\partial E_x}{\partial z} - \frac{\partial E_z}{\partial x} = i\omega\mu_0 H_y \quad \Rightarrow \quad \frac{\partial E_x}{\partial z} - i\beta E_z = i\omega\mu_0 H_y \tag{A.4c}$$

(A.4d)

$$\frac{\partial E_y}{\partial x} - \frac{\partial E_x}{\partial y} = i\omega\mu_0 H_x \quad \Rightarrow \quad i\beta E_y = i\omega\mu_0 H_z \tag{A.4e}$$

(A.4f)

$$\frac{\partial H_z}{\partial y} - \frac{\partial H_y}{\partial z} = -i\omega\varepsilon_0\varepsilon E_x \quad \Rightarrow \quad \frac{\partial H_y}{\partial z} = i\omega\varepsilon_0\varepsilon E_x \tag{A.4g}$$

(A.4h)

$$\frac{\partial H_x}{\partial z} - \frac{\partial H_z}{\partial x} = -i\omega\varepsilon_0\varepsilon E_y \quad \Rightarrow \quad \frac{\partial H_x}{\partial z} - i\beta H_z = -i\omega\varepsilon_0\varepsilon E_y \tag{A.4i}$$

(A.4j)

$$\frac{\partial H_y}{\partial x} - \frac{\partial H_x}{\partial y} = -i\omega\varepsilon_0\varepsilon E_z \quad \Rightarrow \quad i\beta H_y = i\omega\varepsilon_0\varepsilon E_z \tag{A.4k}$$

Two set of equations can be written that govern respectively transverse magnetic modes (p-polarised light) and transverse electric modes (s-polarised light)

TM modes

For TM modes, E_x, E_z and H_y are nonzero. Isolating E_x and E_z from eq. A.4g and A.4k gives:

$$E_x = -i\frac{1}{\omega\varepsilon_0\varepsilon}\frac{\partial H_y}{\partial z} \tag{A.5}$$

$$E_z = -\frac{\beta}{\omega\varepsilon_0\varepsilon}H_y \tag{A.6}$$

Inputting eq. A.5 and eq. A.6 into eq. A.4c, while applying the identity $c = \frac{1}{\mu_0\varepsilon_0}$ yields the wave equation for TM modes:

$$\frac{\partial^2 H_y}{\partial z^2} + (k_0^2\varepsilon - \beta^2)H_y = 0 \tag{A.7}$$

TE modes

For TE modes, H_x, H_z and E_y are non-zero yielding the following from eq. A.4a and eq. A.4e.

$$H_x = i\frac{1}{\omega\mu_0}\frac{\partial E_y}{\partial z} \tag{A.8}$$

$$H_z = \frac{\beta}{\omega\mu_0} E_y \tag{A.9}$$

The wave-equation is therefore:

$$\frac{\partial^2 E_y}{\partial z^2} + (k_0^2\varepsilon - \beta^2)E_y = 0 \tag{A.10}$$

TM modes in a metal and di-electric layer system

A geometry consisting of a metal and di-electric layer is now considered according to figure. A.1.

Figure A.1: *Metal di-electic layer. [53]*

The electric permittivity of the system can be described as:

$$\varepsilon(z) = \begin{cases} \varepsilon_2 \ if \ \ z > 0 \\ \varepsilon_1 \ if \ \ z < 0 \end{cases}$$

The solutions to the TM mode can be obtained from solving eq. A.5, A.6 and A.7 in each layer. The general solution to $H_y(z)$ has to describe waves which are confined to the surface with an electric field that decays exponentially when moving from the interface into the di-electric describing an evanescent field. This implies solutions of the following form.

$$\left.\begin{aligned} H_y(z) &= A_2 e^{i\beta x} e^{-k_2 z} \\ E_x(z) &= iA_2 \frac{1}{\omega \varepsilon_0 \varepsilon_2} k_2 e^{i\beta x} e^{-k_2 z} \\ E_z(z) &= -A_2 \frac{\beta}{\omega \varepsilon_0 \varepsilon_2} e^{i\beta x} e^{-k_2 z} \end{aligned}\right\} for\ z > 0 \tag{A.11}$$

$$\left.\begin{aligned} H_y(z) &= A_1 e^{i\beta x} e^{k_1 z} \\ E_x(z) &= -iA_1 \frac{1}{\omega \varepsilon_0 \varepsilon_1} k_1 e^{i\beta x} e^{k_1 z} \\ E_z(z) &= -A_1 \frac{\beta}{\omega \varepsilon_0 \varepsilon_1} e^{i\beta x} e^{k_1 z} \end{aligned}\right\} for\ z < 0 \tag{A.12}$$

The $H_y(z)$ component in equation-sets A.11 and A.12 have to satisfy the wave equation in eq. A.7 leading to expressions for k_1 and k_2.

$$k_1^2 = \beta^2 - k_0^2 \varepsilon_1 \tag{A.13a}$$
$$k_2^2 = \beta^2 - k_0^2 \varepsilon_2 \tag{A.13b}$$

For appropriate boundary conditions to be fulfilled, it is required that there is a continuity of the tangential components of **E** and **H** across the interface (z=0). This results in:

$$H_y(z=0) = A_2 e^{i\beta x} \quad = \quad H_y(z=0) = A_1 e^{i\beta x} \tag{A.14a}$$

$$\Rightarrow A_1 = A_2 \tag{A.14b}$$

$$E_x(z=0) = iA_2 \frac{1}{\omega\varepsilon_0\varepsilon_2} k_2 e^{i\beta x} \quad = \quad E_x(z=0) = -iA_1 \frac{1}{\omega\varepsilon_0\varepsilon_2} k_1 e^{i\beta x} \tag{A.15a}$$

$$\Rightarrow \frac{k_2}{k_1} = -\frac{\varepsilon_2}{\varepsilon_1} \tag{A.15b}$$

As both k_1 and k_2 are positive, it is apparent that SPPs are found only at the interface between materials where the real part of the di-electric constant changes sign across the interface.

Combining expression A.13a and A.13b with eq. A.15b results in the expression for the dispersion relation of SPPs at the interface.

$$\beta = k_{spp} = k_0 \sqrt{\frac{\varepsilon_1 \varepsilon_2}{\varepsilon_1 + \varepsilon_2}} \tag{A.16}$$

This can be re-written in terms of the wavelength of light and the refractive index of the medium as:

$$k_{spp} = \frac{2\pi}{\lambda} \sqrt{\frac{n_1^2 n_2^2}{n_1^2 + n_2^2}} \tag{A.17}$$

Equating eq. 1.16 and eq. A.17 and rearranging gives the angle of incoming light at which SPPs are excited and thereby the conditions for surface plasmon resonance.

$$\theta_{spr} = sin^{-1} \left(\frac{1}{n_1} \sqrt{\frac{n_1^2 n_2^2}{n_1^2 + n_2^2}} \right) \tag{A.18}$$

TE modes in a metal and di-electric layer system

The possibility of TE surface modes can be investigated by following the previous route and solving the equation set consisting of eq. A.8, A.9 and A.10 resulting in:

$$\left.\begin{aligned} E_y(z) &= A_2 e^{i\beta x} e^{-k_2 z} \\ H_x(z) &= -iA_2 \frac{1}{\omega\varepsilon_0\mu_0} k_2 e^{i\beta x} e^{-k_2 z} \\ H_z(z) &= A_2 \frac{\beta}{\omega\varepsilon_0\mu_0} e^{i\beta x} e^{-k_2 z} \end{aligned}\right\} for\ z > 0 \tag{A.19}$$

$$\left.\begin{aligned} E_y(z) &= A_1 e^{i\beta x} e^{k_1 z} \\ H_x(z) &= iA_1 \frac{1}{\omega\varepsilon_0\mu_0} k_1 e^{i\beta x} e^{k_1 z} \\ H_z(z) &= -A_1 \frac{\beta}{\omega\varepsilon_0\mu_0} e^{i\beta x} e^{k_1 z} \end{aligned}\right\} for\ z < 0 \tag{A.20}$$

Applying the same boundary conditions result in $A_1 = A2$ and $-k_1 = k_2$ which is not possible since both need to be positive. Hence, s-polarised light can not excite surface plasmon polaritons.

B | CaDNAno DNA origami designs

B.1 18 hb design

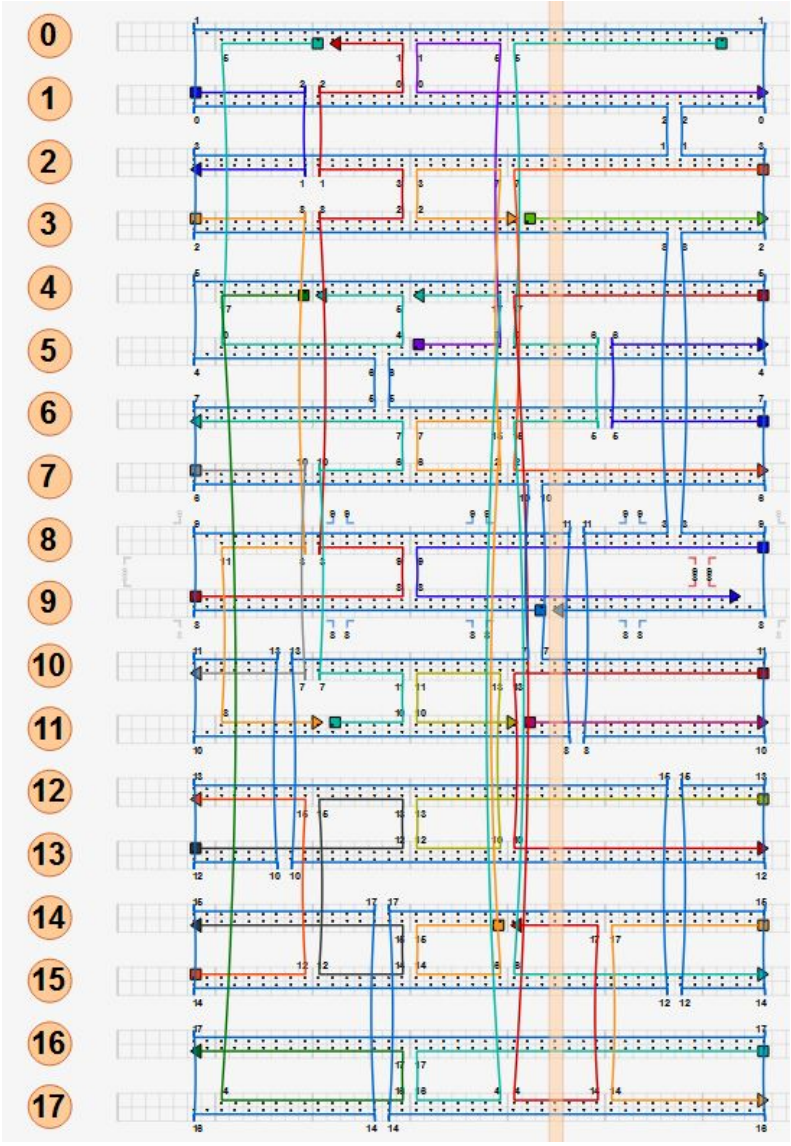

FIGURE B.1: *18 hb DNA origami caDNAno design diagram*

B.2 42 hb design

Green staples have a 5′-end overhang of 15 poly-dA used as capturing anchors of 15 poly-dT thiolated DNA strands coupled to Au-NPs. Yellow strands are newly introduced staples that accommodate the changes in the design. The purple strand is modified with the ATTO-647N dye. Lastly, red strands are staples that have been modified with a 5 poly-dT overhang that serves as passivation against the formation of multimer structures.

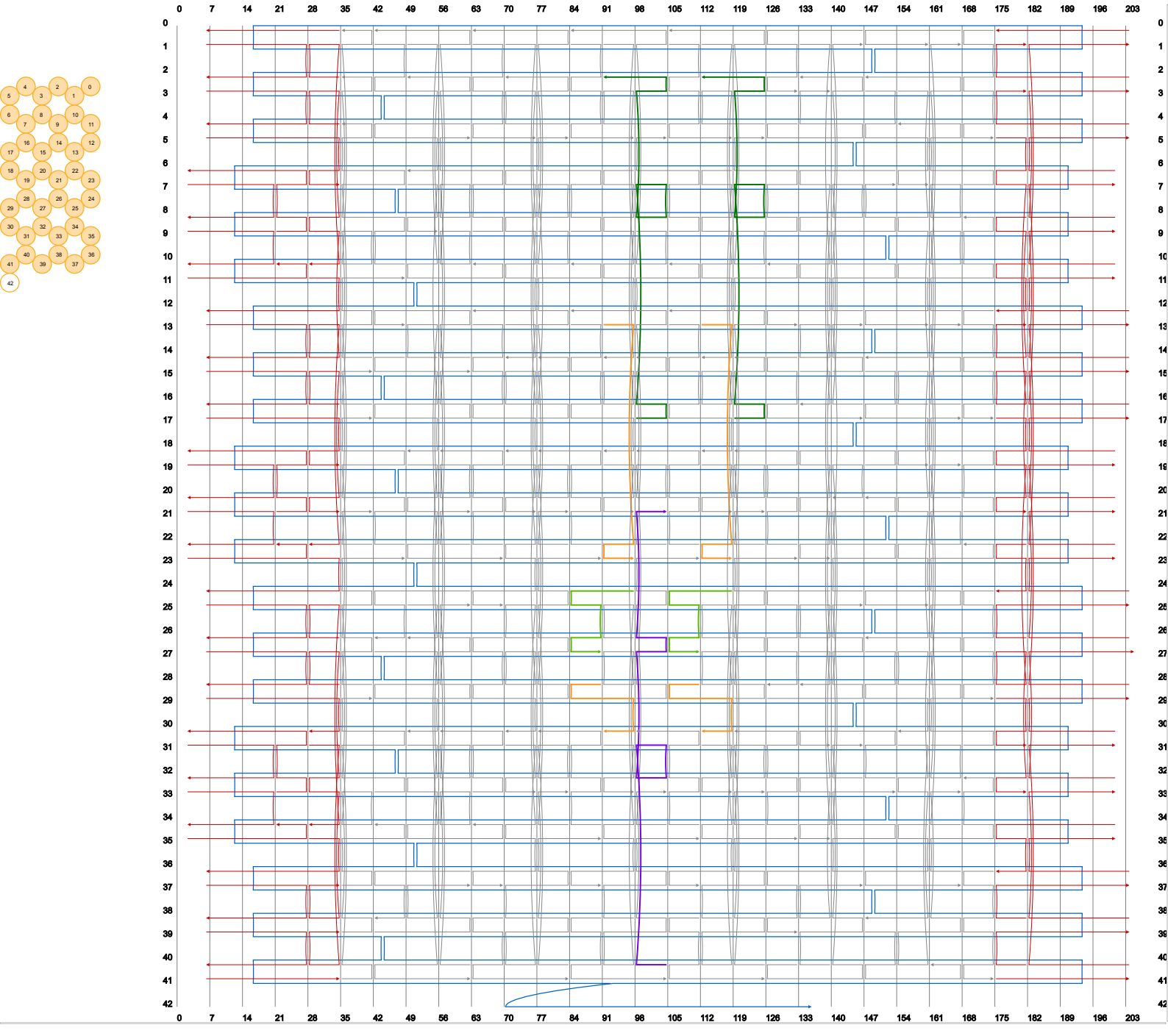
0 7 14 21 28 35 42 49 56 63 70 77 84 91 98 105 112 119 126 133 140 147 154 161 168 175 182 189 196 203
0 1 2 3 4 5 6 7 8 9 10 11 12 13 14 15 16 17 18 19 20 21 22 23 24 25 26 27 28 29 30 31 32 33 34 35 36 37 38 39 40 41 42
4 3 2 1 0
5 6 7 8 9 10 11
16 15 14 13 12
17 18 19 20 21 22 23
28 27 26 25 24
29 30 31 32 33 34 35
40 39 38 37 36
41 42

B.3 1D sheet

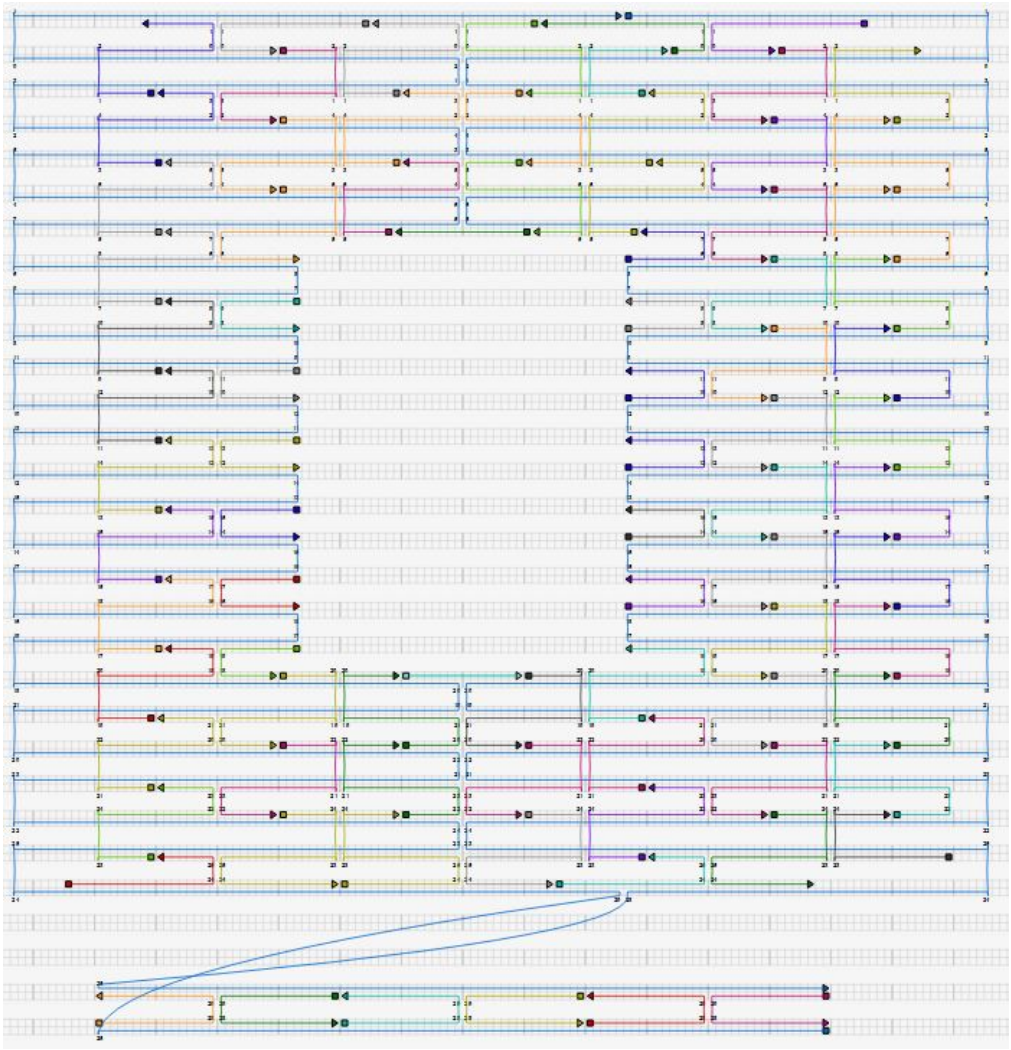

Figure B.2: *CaDNAno design of a DNA origami 1D sheet*

C | CanDo simulation results

C.1 18 hb

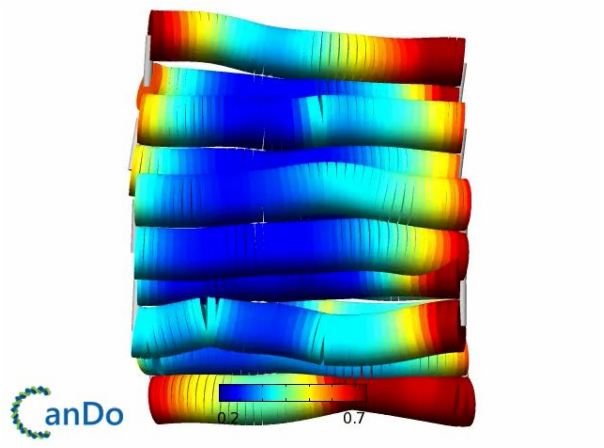

(a)

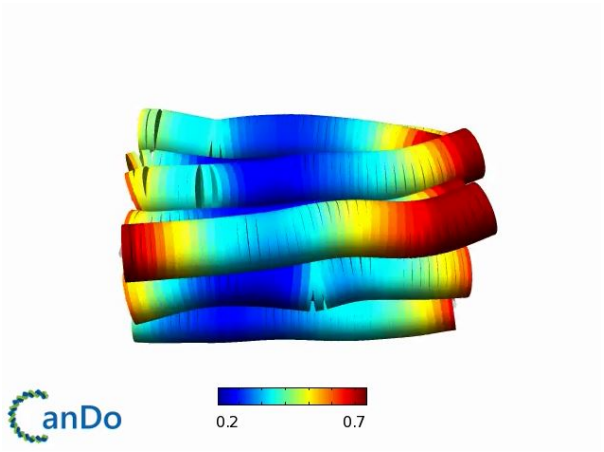

(b)

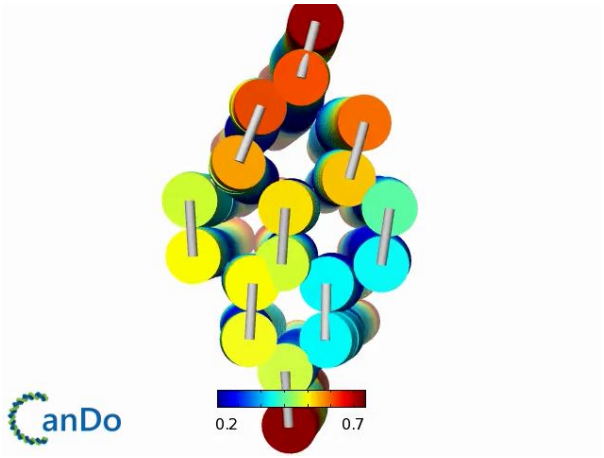

(c)

Figure C.1: *RMSF of the 18 hb DNA origami structure*

C.2 42 hb

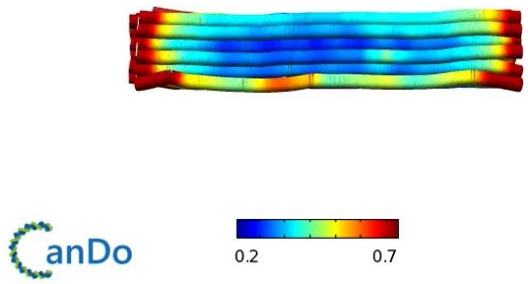

(a)

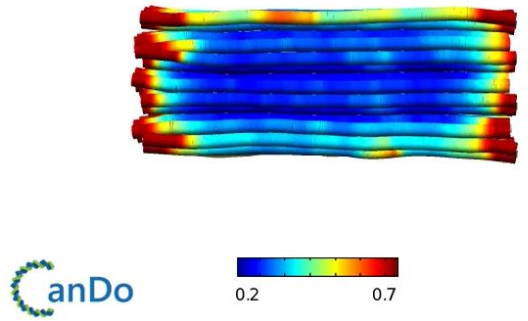

(b)

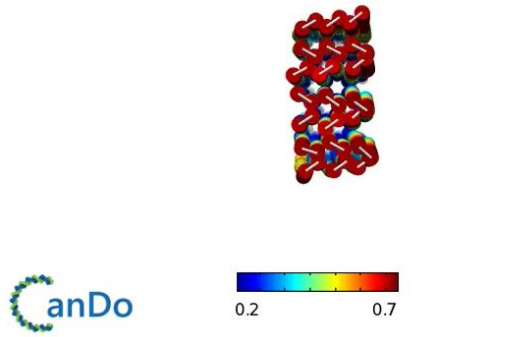

(c)

FIGURE C.2: *RMSF of the 42 hb DNA origami structure*

C.3 1D sheet

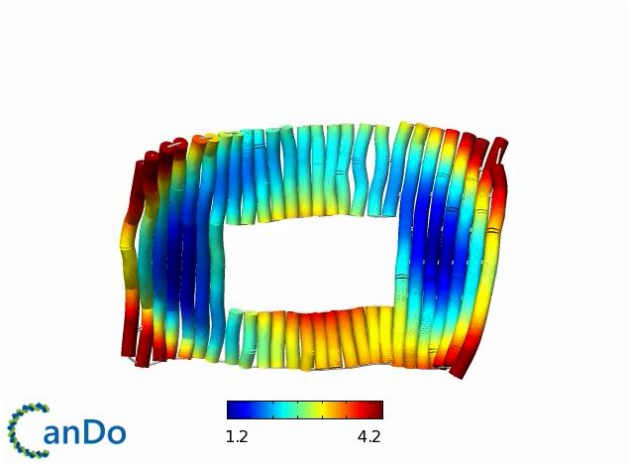

(a)

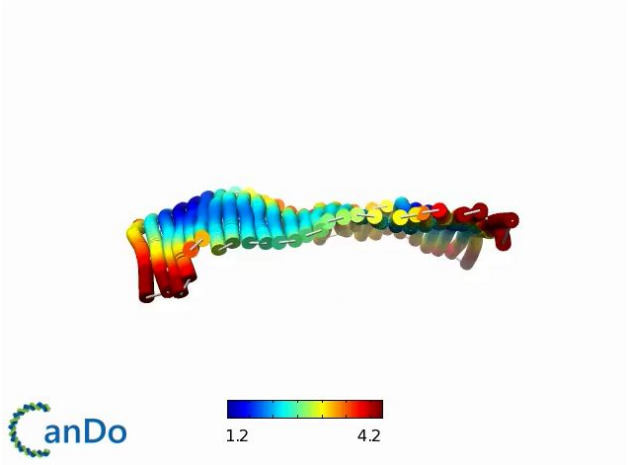

(b)

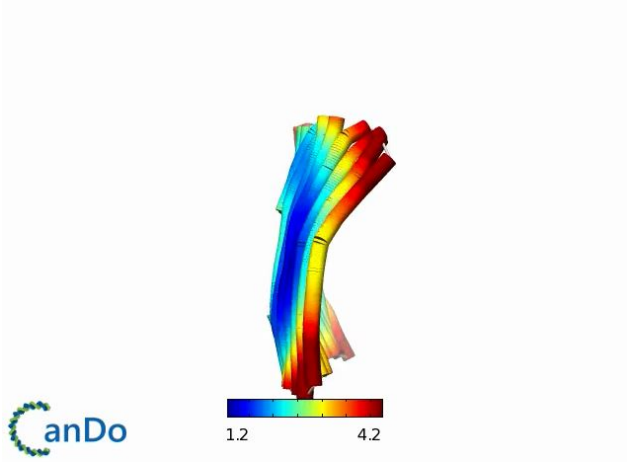

(c)

Figure C.3: *RMSF of the 1D DNA origami sheet*

D | Electric field strengths/decay data

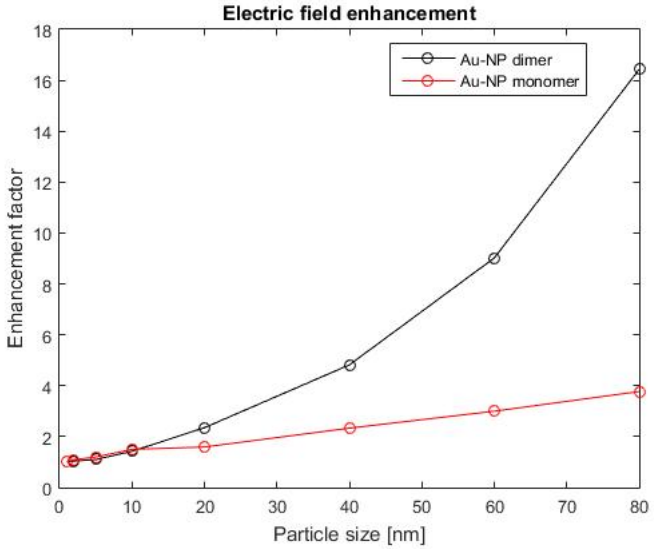

FIGURE D.1: *Electric field strengths at dipole positions.*

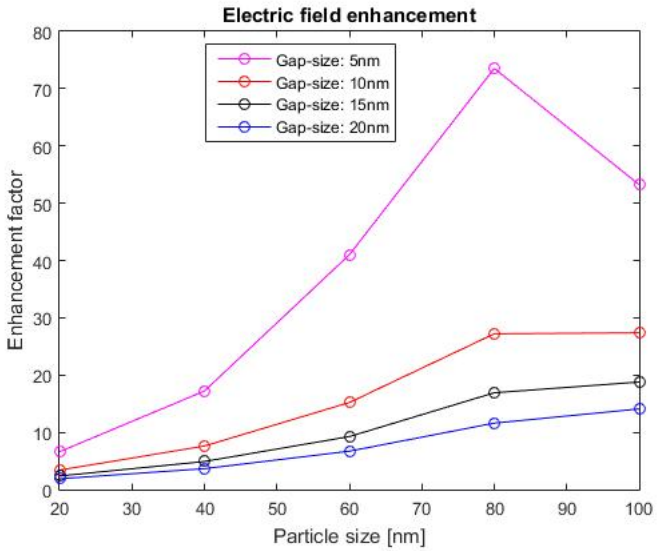

FIGURE D.2: *Electric field strengths in the center of Au-NP dimer-gaps with different gap-distances.*

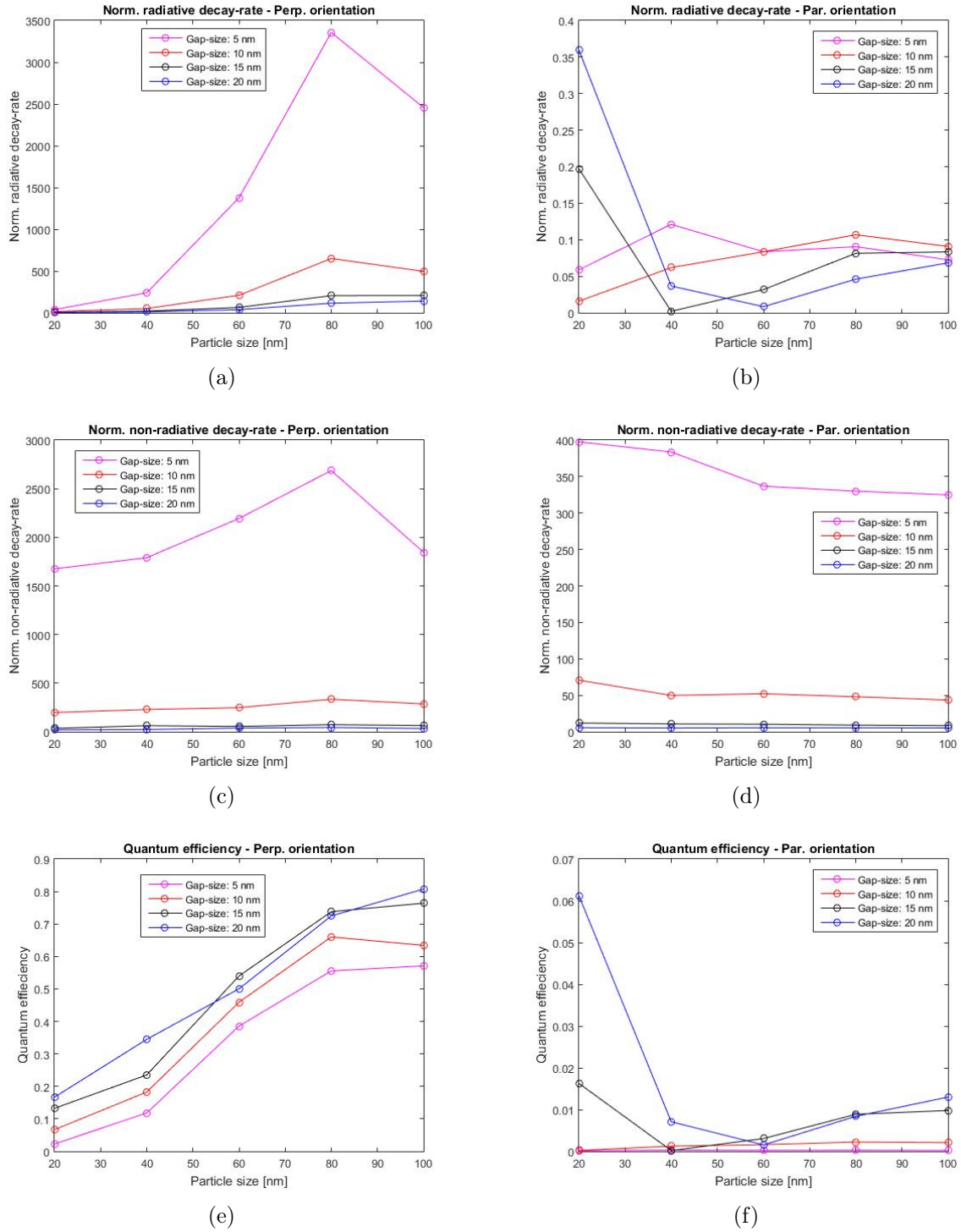

Figure D.3: *Decay-rate data and QE values of a dipole emitting light at 665 nm in dimer-gaps of different distances.*

E | Quantum yield data/FEF for a dipole in dimer gap

The dipole is positioned at different locations in a 15 nm dimer-gap with 80 nm Au-NPs. The electric field used to calculate the fluorescence enhancement is found in figure. 5.4

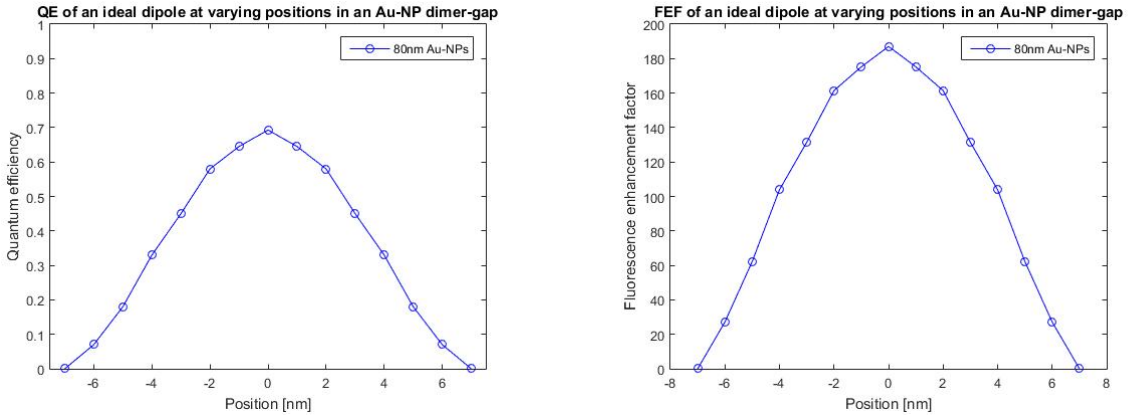

(a) (b)

FIGURE E.1: *Average quantum efficiency of an ideal dipole in addition to the expected fluorescence enhancement.*